

Lawrence Berkeley National Laboratory

Recent Work

Title

KINETIC AND TEM STUDIES OF DECOMPOSITION OF $Mg(OH)_2$ AND $MgCO_3$

Permalink

<https://escholarship.org/uc/item/33z045c9>

Author

Kim, M.G.

Publication Date

1985-11-01

e.2



Lawrence Berkeley Laboratory

UNIVERSITY OF CALIFORNIA

RECEIVED
LAWRENCE
BERKELEY LABORATORY

Materials & Molecular Research Division

FEB 18 1986

LIBRARY AND
DOCUMENTS SECTION

KINETIC AND TEM STUDIES OF DECOMPOSITION
OF $Mg(OH)_2$ AND $MgCO_3$

M.G. Kim
(Ph.D. Thesis)

November 1985

TWO-WEEK LOAN COPY
*This is a Library Circulating Copy
which may be borrowed for two weeks.*



LBL-20623
e.2

DISCLAIMER

This document was prepared as an account of work sponsored by the United States Government. While this document is believed to contain correct information, neither the United States Government nor any agency thereof, nor the Regents of the University of California, nor any of their employees, makes any warranty, express or implied, or assumes any legal responsibility for the accuracy, completeness, or usefulness of any information, apparatus, product, or process disclosed, or represents that its use would not infringe privately owned rights. Reference herein to any specific commercial product, process, or service by its trade name, trademark, manufacturer, or otherwise, does not necessarily constitute or imply its endorsement, recommendation, or favoring by the United States Government or any agency thereof, or the Regents of the University of California. The views and opinions of authors expressed herein do not necessarily state or reflect those of the United States Government or any agency thereof or the Regents of the University of California.

KINETIC AND TEM STUDIES OF DECOMPOSITION
OF $\text{Mg}(\text{OH})_2$ AND MgCO_3

Mun Gyu Kim

(Ph.D. Thesis)

Materials and Molecular Research Division
Lawrence Berkeley Laboratory
and
Department of Materials Science and Mineral Engineering
University of California, Berkeley
Berkeley, California 94720

November 1985

KINETIC AND TEM STUDIES OF DECOMPOSITION
OF $\text{Mg}(\text{OH})_2$ AND MgCO_3

Mun Gyu Kim
(Ph.D. Thesis)

Department of Materials Science and Mineral Engineering
University of California, Berkeley
Berkeley, California 94720

ABSTRACT

Thermogravimetric and TEM studies have been carried out in order to better understand the reaction mechanisms of decomposition of $\text{Mg}(\text{OH})_2$ and MgCO_3 in vacuum.

The TEM studies revealed that the decompositions produce no intermediate phases but yield highly porous pseudomorphic MgO of normal structure which preserves definite orientation relationships to the parent solids. The decomposition of MgCO_3 yields MgO with two variants in a major orientation relationship; $(0001) \text{MgCO}_3 // (111) \text{MgO}$, $[\bar{1}1\bar{2}0] \text{MgCO}_3 // [2\bar{1}\bar{1}] \text{MgO}$ while the decomposition of $\text{Mg}(\text{OH})_2$ has only a single orientation relationship; $(0001) \text{Mg}(\text{OH})_2 // (111) \text{MgO}$, $[\bar{1}1\bar{2}0] \text{Mg}(\text{OH})_2 // [10\bar{1}] \text{MgO}$.

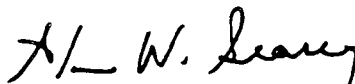
The observed major orientation relationships suggest that oxygen octahedra in the reactant solids are the coherent nuclei for the growth of MgO particles. The MgO is produced as cubes of 2 and 3 nm

in average size from the decomposition of $\text{Mg}(\text{OH})_2$ and MgCO_3 , respectively.

As the decomposition proceeds, MgO particles aggregate to reduce the high surface energy arising from the very small particles and minute (~10 to 50 nm cross section) cracks result.

The thermogravimetric study of single crystal $\text{Mg}(\text{OH})_2$ demonstrates that the decomposition occurs from all the surfaces, but with flux densities from the (0001) habit plane which are about one-tenth of those from the surface normal to the habit plane at 605 K. An SEM observation shows the decomposition rates for MgCO_3 to be the same in each direction normal to rhombohedral cleavage surfaces. Apparent equilibrium fluxes are measured from an open crucible in vacuum which are only $\sim 10^{-7}$ times the true equilibrium fluxes and $\sim 10^{-3}$ times the apparent equilibrium fluxes measured in effusion cells. The low apparent equilibrium pressures probably result from an equilibrium of $\text{Mg}(\text{OH})_2$, MgO, and H_2O adsorbed on the MgO.

The decomposition rates of MgCO_3 single crystal are characteristic of an irreversible process, probably either a desorption step or a surface step, depending on the temperature of the decomposition. The decomposition of MgCO_3 powder in Knudsen cells at 630-800 K shows behavior characteristic of a transition regime between an irreversible and a reversible process.



Alan W. Searcy, Chairman of Committee

CONTENTS

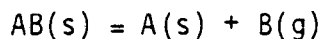
Abstract	vii
I. General Introduction.	1
II. Kinetic Studies	6
1. Introduction.	6
2. Background.	8
2.1. Thermodynamics and Kinetics of Decomposition Reactions	8
2.2. Langmuir and Knudsen Effusion Methods	13
3. Experimental Procedures	15
3.1. Starting Materials.	15
3.2. Thermogravimetric Experiments	16
3.3. Temperature Calibration	18
4. Results and Discussion.	21
4.1. Decomposition of $Mg(OH)_2$	21
4.2. Decomposition of $MgCO_3$	26
III. TEM Studies	33
1. Introduction.	33
2. Background.	35
2.1. Crystal Structures of $Mg(OH)_2$, $MgCO_3$, and MgO	35
2.1.1. $Mg(OH)_2$ Structure	35
2.1.2. $MgCO_3$ Structure	37
2.1.3. MgO Structure	38

2.2.	Structural Study of Decomposition	
	Reactions by TEM.	39
2.2.1.	Electron Diffraction.	39
2.2.2.	Morphological Observations.	41
3.	Previous Studies.	42
3.1.	Orientation Relationships	42
3.2.	Lattice Parameter of Product Solid MgO.	42
3.3.	Morphological Observations.	44
3.4.	Suggested Decomposition Mechanisms.	46
3.4.1.	Mechanisms of Mg(OH) ₂ Decomposition	46
3.4.1.1.	Homogeneous Mechanism	47
3.4.1.2.	Inhomogeneous Mechanism	49
3.4.1.3.	Nucleation and Growth Mechanism	50
3.4.2.	Mechanisms of MgCO ₃ Decomposition	51
4.	Experimental Procedures	52
4.1.	Materials	52
4.2.	Preparation of TEM Specimen	52
4.3.	Transmission Electron Microscopy (TEM).	55
4.4.	Other Analyses Supporting the TEM Work.	58
4.4.1.	X-ray Diffraction (XRD) Measurements.	58
4.4.2.	Microdensitometer Measurements.	58
4.4.3.	Optical Diffraction	59
4.4.4.	Scanning Electron Microscopy (SEM).	59
4.4.5.	BET Surface Area Measurements	60

5. Results and Discussion.	60
5.1. Structural and Morphological Changes.	60
5.1.1. Decomposition of $Mg(OH)_2$	61
5.1.2. Decomposition of $MgCO_3$	67
5.1.3. Origin of the Orientation Variants.	70
5.2. Lattice Parameter of the Product Solid MgO	73
5.3. Particle Size and Shape of the Product Solid MgO	75
5.3.1. Direct Observation.	75
5.3.2. Optical Diffractions.	77
5.3.3. Comparison of the Surface Areas by BET and TEM Methods.	78
5.4. Cracking Phenomena of Decomposition Reactions	79
IV. General Discussion.	81
V. Summary and Conclusion.	84
Acknowledgements	86
References	88
Tables	96
Appendices	100
Figure Captions.	107
Figures.	114

I. GENERAL INTRODUCTION

Reactions in which a solid reactant yields a new solid plus a gas product, that is, reactions which can be described by the general expression



are usually called decomposition reactions [1-3].

Most of the oxides useful in the cement, steel manufacturing, glass, and refractory industries, etc. are produced by the decomposition, or so-called calcination, of hydroxides or carbonates [4,5]. Alkaline earth oxides are not commonly found in nature as are the hydroxides and carbonates. Furthermore, synthetic processes for obtaining oxides, such as precipitation methods or sol-gel processes, often produce hydroxides, or carbonates, etc. which must be decomposed to the oxides for ceramic processing in a later stage [5,6]. The industrial importance of decomposition reactions stimulated the earlier investigations [7], but later scientific questions about decomposition reaction kinetics and properties of the product solids became an important motivation for study [1-3,8-10]. Nevertheless, there has been insufficient understanding about the decomposition reactions.

Essential steps in this kind of reactions are the evolution of gas phase from the solid AB and then the structural change of solid from AB(s) to A(s). Kinetic studies have dealt with the first step to get reaction rates and reaction mechanisms which are deduced from kinetic

models. Structural studies have dealt with the second step to understand reaction mechanisms from atomistic and structural points of view. It is found in the literature [1,3,8] that often decomposition mechanisms are deduced either from kinetic work only or structural work only. However, complete understanding of decomposition mechanism requires a combination of both kinetic and structural studies.

Decomposition of $\text{Mg}(\text{OH})_2$ has been one of most frequently studied reactions [11], but the decomposition mechanism is still obscure [12,18]. Giauque and Archibald [13] measured the equilibrium water vapor pressure of the reaction $\text{Mg}(\text{OH})_2(\text{s}) = \text{MgO}(\text{s}) + \text{H}_2\text{O}(\text{g})$, by a static method using a manometer. Their measured water vapor pressures agreed relatively well with the equilibrium decomposition pressures measured thermochemically. Later, Kay and Gregory [14] measured by the Knudsen effusion method an anomalous apparent equilibrium water decomposition pressure, which is about four orders of magnitude smaller than the equilibrium decomposition pressure measured manometrically for the same reaction. The Knudsen effusion method has been an effective method for measuring the true equilibrium pressures of other systems [15,16]. This discrepancy between the equilibrium pressures measured by a static method and the anomalous equilibrium pressures measured by the Knudsen effusion method has never been explained [17,18].

Such an anomalous equilibrium pressure could result because the product solid, MgO , has a higher energy content than that of normal MgO . Such an MgO of higher energy would equilibrate with $\text{Mg}(\text{OH})_2$

and H_2O of lower vapor pressure than does normal MgO , as illustrated in Fig. 1. Reis [17] reported the Knudsen cell decomposition of $Mg(OH)_2$ at 573 K. His experiment reproduced Kay and Gregory's anomalous equilibrium pressures even though the $Mg(OH)_2$ used was different in particle size and origin. Kay and Gregory used a pure natural brucite and Reis used the $Mg(OH)_2$ formed by a precipitation method. Reis also measured by solution calorimetry the energy content of MgO produced from the decomposition of $Mg(OH)_2$ in vacuum. He did not find any significant excess energy content which could explain the anomalous equilibrium.

Beruto et al. [18] also measured by solution calorimetry the heat content of MgO prepared from the decomposition of $Mg(OH)_2$, but they were careful to desorb the adsorbed water on the surface of MgO . Their measured heat content of MgO , which was as much as 73 kJ/mole higher than that of normal MgO , is high enough to account for the anomalous equilibrium described above. They argued that Reis might not be able to find the high energy content of MgO due to adsorbed water on the surface of MgO since Beruto et al. could get the high energy content of MgO only after desorption of water for a long time at 873 K. However, Beruto et al.'s experimental result may not be relevant to MgO produced in Kay and Gregory's Knudsen cell experiment because the MgO produced in the Knudsen cell at low temperatures (450 to 600 K) surely has a high degree of water adsorption [19-23].

A possibility that could not be ruled out is that the initial solid product of $Mg(OH)_2$ decomposition is a metastable phase, which

had escaped detection perhaps because it transforms irreversibly to normal MgO continuously as reaction proceeds. Transmission electron microscopy (TEM) is well suited to test whether such a metastable phase or phases is responsible for the anomalous equilibrium in the decomposition of $\text{Mg}(\text{OH})_2$.

Decomposition of MgCO_3 also yields MgO as the solid product of decomposition. Unlike $\text{Mg}(\text{OH})_2$ decomposition, MgCO_3 decomposition has been rarely studied from the kinetic point of view [3]. No Knudsen cell study has been made to check whether an anomalous equilibrium behavior like that observed in the decomposition of $\text{Mg}(\text{OH})_2$ similarly affects the decomposition of MgCO_3 .

Another interesting observation from the decomposition of hydroxides and carbonates is the explosive blow-out of powder samples when heated in vacuum at a constant temperature. It was shown for CaCO_3 that phenomenon cannot be due to a pressure gradient established in the powder bed because the flux density was independent of sample amount and sample packing density, and because the explosive blow-out occurred in irregular fashion and was not correlated with the degree of decomposition [24]. It was suggested that sudden exothermic heat generated locally by the transition from some sort of metastable phase to a stable phase triggers fast decomposition and thus produces enough gas pressure to blow powder sample out of the crucible [25].

This explanation of explosive blow-out may be related to the exothermic peaks which have been observed in differential thermal analysis (DTA) studies of decomposition of some hydroxides and

carbonates by Rao et al. [26]. Rao et al. attributed these exothermic peaks to annihilation of defects of product solids.

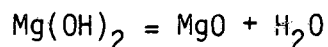
For the better understanding of these questions which arise in decomposition reactions, this study has used $\text{Mg}(\text{OH})_2$ and MgCO_3 , which decompose to produce the same product solid, MgO but different gases, H_2O and CO_2 . Studying $\text{Mg}(\text{OH})_2$ and MgCO_3 decompositions will help us to understand the effects of different reactant solids and product gases on decomposition reactions. Emphasis has been put on discovering where the anomalous thermodynamic behavior in the decomposition of $\text{Mg}(\text{OH})_2$ originates and what causes the exothermic process which explosively ejects powder samples during the decomposition of hydroxides and carbonates.

To this end, kinetic studies by thermogravimetry and structural studies by transmission electron microscopy in addition to X-ray, surface area, and scanning electron microscope (SEM) measurements have been carried out.

II. KINETIC STUDIES

1. Introduction

After Giaouque and Archibald [13] carefully measured the water vapor pressure of the decomposition reaction



by a static method, numerous kinetic studies yielded quite inconsistent activation energies for the reaction. Values ranged from about 80 kJ/mole to 400 kJ/mole [32]. In addition to Kay and Gregory's Knudsen cell study [14], the kinetics of decomposition of Mg(OH)_2 has been studied by a large number of workers mainly by means of differential thermal analysis (DTA) [27] and thermogravimetry (TG) [28-32].

In a recent review article, Sharp [32] concluded, however, that many of the methods developed for the kinetic analysis of DTA traces of solid state reactions yield unreasonable values for the activation energy and order of reaction. He concluded that DTA measurements in air or N_2 yield higher activation energies than does isothermal thermogravimetry in vacuum, probably because of the build-up of the water vapor pressure in the vicinity of the sample, and he reported the activation energy for the dehydration of pure Mg(OH)_2 in vacuum is ~84 kJ/mole which is close to the standard enthalpy of the reaction. However, Gordon and Kingery's kinetic study [31] by thermogravimetric technique of the dehydration of Mg(OH)_2 in vacuum yielded an activation energy of ~126 kJ/mole which is consistent with

the activation energy, ~130.5 kJ/mole obtained in the Kay and Gregory's Knudsen cell study.

From curve fitting of kinetic models, $\text{Mg}(\text{OH})_2$ decomposition has been reported to start at the edges normal to the basal plane and to proceed along the basal plane in the form of a contracting disk [29]. Although this scheme is plausible in terms of the structure of $\text{Mg}(\text{OH})_2$, it has not been clearly proven [31].

In this study, an open cell has been used for thermogravimetric measurements to check the activation energy of the reaction for $\text{Mg}(\text{OH})_2$ powder samples. Single crystals of $\text{Mg}(\text{OH})_2$ have also been decomposed in order to determine where the reaction starts and to determine how the reaction interfaces move.

There has been no previous Knudsen cell study of decomposition of MgCO_3 . From conventional kinetic studies of the decomposition, activation energies of $\sim 149 \pm 14$ kJ/mole and ~ 136 kJ/mole were reported by Britton et al. [33] and Li [34], respectively. These activation energies, much higher than that of the standard equilibrium reaction, ~ 113 kJ/mole, could indicate that the decomposition of MgCO_3 has a metastable equilibrium as found in the decomposition of $\text{Mg}(\text{OH})_2$. Therefore, single crystal and Knudsen cell decomposition measurements have been made of MgCO_3 to test whether the decomposition has a similar behavior to that observed in the Knudsen cell studies of $\text{Mg}(\text{OH})_2$ decomposition.

The overall kinetic study may delineate the effects of product gas and reactant structure on the decomposition of the magnesium compounds to the magnesium oxide.

2. Background

2.1. Thermodynamics and Kinetics of Decomposition Reactions

Decomposition reactions can occur when the Gibbs free energy change of the reactions is negative [38]. The Gibbs free energy change for the decomposition reactions is given by

$$\Delta G = \Delta G^\circ + RT \ln \left[\frac{a_{A(s)} a_{B(g)}}{a_{AB(s)}} \right]$$

where ΔG° denotes the standard Gibbs free energy change and each a is the activity indicated by its subscript. If the activity of solids is considered to be unity and the gas is an ideal gas with the standard state defined as unit pressure, the standard Gibbs free energy change is $\Delta G^\circ = -RT \ln P_{eq}$. Then, if the product pressure surrounding a reactant solid is lower than the equilibrium pressure, the reactant solid will be decomposed at the interfaces where a pressure gradient gives the driving force, $\Delta G = RT \ln(P/P_{eq})$, for the decomposition. Therefore, the standard Gibbs free energy change, ΔG° , is the starting information for a kinetic study of decomposition reactions.

The standard Gibbs free energy changes for $Mg(OH)_2$ and $MgCO_3$ decompositions in the experimental temperature range are given below in terms of the standard enthalpy and entropy changes of the reactions which are obtained from thermodynamic tables [35-37].



Although the Gibbs free energy change predicts the possibility of a reaction, the reaction rate can only be determined experimentally by a kinetic study.

The usual practice in kinetic studies of decomposition reactions is to get the reaction rate constants (k) from the best fit among kinetic models, such as those listed in Table 1, to a reaction rate curve such as the fraction reacted (α) versus time (t) curve and to obtain the activation energy of the reaction from the slope of $\log k$ versus $1/T$ plot [1-3,8]. Most solid state reactions give a linear plot of $\log k$ versus $1/T$ where $k = A \exp(-E/RT)$, A is the so-called pre-exponential factor, and E is called the activation energy of the reaction. Any deviation from linearity of an Arrhenius plot can be related to a change of rate limiting step, since the enthalpy and entropy change of reactions are usually nearly independent of temperature if there is no phase change other than those for the reaction [40].

The empirical Arrhenius equation was given some theoretical significance by van't Hoff who expressed the influence of temperature on the equilibrium constant (K_e) as a consequence of detailed balancing of reaction rates at equilibrium

$$K_e = k_1/k_2 = \exp(-\Delta G^\circ/RT) \quad (1)$$

where k_1 is the forward reaction rate constant and k_2 the backward reaction rate constant [39]. This equation provides a justification for comparison of the kinetically obtained activation energy with the standard enthalpy change of the reactions, but problems arise in its

application to real decomposition reactions because net decomposition cannot occur at equilibrium; equation (1) is only known to be exact at equilibrium.

The conventional curve fitting to kinetic models of Table 1 has been proven to be a notoriously poor way to decide the rate limiting step if the conditions of decomposition are not accurately defined and controlled so that the measured apparent activation enthalpy can be assigned to a rate limiting step [25,31,32].

Langmuir [41] argued that the flux of evaporating molecules should remain unchanged from the equilibrium flux if evaporation occurs into vacuum. He predicted the maximum possible flux by the equation

$$J_{\text{max.}} = P_{\text{eq}} (2\pi MRT)^{-1/2} ; P_{\text{eq}} = \exp (-\Delta G^{\circ}/RT)$$

where J, the flux density, has the units of number of moles per unit area per unit time and M is the molar weight of the gas.

Knudsen [42] showed, however, that pressures calculated from weight losses may sometimes be orders of magnitude lower than pressures measured under proved equilibrium conditions. He introduced a factor, α into the Langmuir equation so that it becomes,

$$J = \alpha P_{\text{eq}} (2\pi MRT)^{-1/2}$$

Then α , the decomposition coefficient, is defined as the ratio of experimentally observed flux from the crystal surface to the thermodynamic equilibrium flux [9,10].

Searcy [43] and Searcy and Beruto [44] expressed α in terms of fundamental thermodynamic parameters for the overall reaction and of fundamental kinetic parameters for elementary reaction steps. They

also applied transition state theory to explain reactions giving α less than unity. In transition state theory for reaction kinetics, the activated complex is the aggregate of atoms at the saddle point free energy position of the rate determining step of the reaction, and it is assumed that reactions occur by means of such an activated complex equilibrated with reactants. For a decomposition coefficient of unity, the saddle point enthalpy and entropy differ from the enthalpy and entropy of reactant solid in such a way that the activated complex is the gas phase and product solid, which are the thermodynamic equilibrium reaction products. For a decomposition coefficient of less than unity, the saddle point enthalpy and entropy of the rate determining step are no longer those for the thermodynamic equilibrium reaction products but for other activated complexes of higher thermal free energy state.

Searcy and Beruto [9,10] derived a general theory for determining the rate limiting steps for the decomposition reactions. They wrote equations for the molecular fluxes of each essential reaction step such as a chemical step, a diffusion step in the reactant solid, a surface or desorption step of the product gas molecule, and a gas phase diffusion step. They also evaluated the influence of the thermodynamic stability of the solid product. Their results are expressed in terms of derived fluxes which can be compared with the fluxes measured in single crystal decomposition experiments.

It should be pointed out that previous studies on decomposition reactions often concluded that a reaction is reversible if the measured activation energy is equal to or close to the standard enthalpy change of the reaction without prescribing data from which the activation entropy change of the reaction can be calculated. This conclusion based on the enthalpy change may not be correct because chemical reversibility can only be established by demonstrating that both the activation enthalpy and activation entropy changes of the reaction are equal to the corresponding changes of the equilibrium reaction [43].

To measure both the apparent enthalpy and entropy changes, the sample surface area must be defined in order to evaluate the flux from weight loss measurements. These fluxes can be converted to the pressures by the Hertz-Knudsen-Langmuir equation (HKL equation),

$$J = P(2\pi MRT)^{-1/2}$$

Thus pressures measured as a function of temperature provide a $\log P$ versus $1/T$ plot in which the slope and intercept give the apparent activation enthalpy and entropy changes of the reaction. To this end the decomposition of a single crystal with known surface area (a Langmuir experiment) and studies with powders in cells pierced by small orifices (Knudsen effusion experiments) are best used for kinetic study of decomposition reactions.

2.2. Langmuir and Knudsen Effusion Methods

The rate of escape of a gas per unit area of sample surface or of orifice cross sectional area (flux density, J) is related to the pressure by the HKL equation derived from gas kinetic theory. If the reaction rate is measured in vacuum with a single crystal of known surface area, the vapor pressure from the measured flux density is called the Langmuir kinetic vapor pressure (P_L) which is correlated with the equilibrium pressure (P_{eq}) through α (the vaporization coefficient in a congruent vaporization reaction or the decomposition coefficient for decomposition reactions).

$$P_L = \alpha P_{eq}$$

Here α is not less than zero, and takes a maximum value of unity if there is no excess thermal free energy barrier to the reaction. The significance of the Langmuir coefficient as a measure of activation enthalpy and entropy was already introduced in the previous section.

An equilibrium vapor pressure can be obtained for a reaction having a decomposition coefficient less than unity by measuring the vapor flux that escapes from Knudsen cells of different orifice areas and using the Whitman-Motzfeltdt extrapolation [45,46]. The Whitman-Motzfeltdt equation assumes a steady state gas flow and is given below [52]:

$$\frac{1}{P_K} = \frac{1}{P_{eq}} \left[1 + \frac{W_B B}{A} \left(\frac{1}{\alpha} + \frac{1}{W_A} - 2 \right) \right]$$

If the Knudsen cell is ideal, i.e., $W_A = 0.5$, the above equation becomes

$$\frac{1}{P_K} = \frac{1}{P_{eq}} \left(1 + \frac{W_B B}{\alpha A} \right)$$

where P_K = measured vapor pressure from the flux escaping through the orifice of Knudsen cell

P_{eq} = equilibrium vapor pressure

α = decomposition coefficient

A = effective sample surface area

B = cross sectional area of orifice

W_A = Clausing correction factor [47] of cell

W_B = Clausing correction factor of orifice

From weight loss measurements, P_K is given by the equation

$$P_K = J_K (2\pi MRT)^{1/2} = \frac{\Delta W}{MW_B B \Delta t} (2\pi MRT)^{1/2}$$

where $(\Delta W/\Delta t)$ is the weight loss per unit time and M the molar weight of effusing gas.

Using the Whitman-Motzfeltdt extrapolation, a plot of $1/P_K$ versus $W_B B$ will give an intercept which is the inverse of an equilibrium pressure at a given temperature. If there is no change of rate limiting step with the change of orifice area, the Whitman-Motzfeltdt extrapolation should be linear to zero orifice area [48].

The Knudsen cell pressure measured as a function of temperatures can be plotted on a log P versus 1/T plot to yield the apparent enthalpy and entropy change from the slope and intercept, respectively by the equation

$$\log P = - \frac{\Delta H}{2.303R} \left(\frac{1}{T} \right) + \frac{\Delta S}{2.303R}$$

If the equilibrium pressure is obtained from the linear extrapolation to zero orifice, the corresponding apparent enthalpy and entropy changes will be those for an equilibrium reaction. The other assumptions and implications of Knudsen cell experiments are well described in the literature [49-52].

3. Experimental Procedures

3.1. Starting Materials

Three kinds of Mg(OH)₂ and two kinds of MgCO₃ were used for this study. Their impurities are listed in Table 2.

The precipitated Mg(OH)₂ (hereafter referred to as G&A Mg(OH)₂) was synthesized in this laboratory according to the method described by Giauque and Archibald [13]. Details of the synthesis were described in the literature [13,17]. An SEM micrograph of G&A Mg(OH)₂ showed well defined hexagonal crystals (Fig. 2A). This G&A Mg(OH)₂ powder was used for open cell studies of decomposition of Mg(OH)₂.

Brucite A, which is natural brucite obtained from Wood's mine, Texas, Pennsylvania, had a clean and transparent single crystalline form and was used for single crystal decomposition experiments. This brucite was used for $\text{Mg}(\text{OH})_2$ decomposition by many other investigators [14,82,83] so that for comparison of different experimental results the effects of starting materials can be excluded.

An MgCO_3 sample (Magnesite A) obtained from the Baymag Plant, Calgary, Alberta, Canada, was a polycrystalline material which consisted of grains of 2 to 3 mm size. Magnesite A was crushed and ground. Uniform particles of 20 to 30 μm were obtained by use of an ultrasonic fine sieve. The powdered Magnesite A shown in Fig. 2B was used for Knudsen cell experiments. Magnesite B, which was obtained from Djebel Hadifa, Algeria, was provided as a large piece of single crystal and was used for single crystal experiments.

3.2. Thermogravimetric Experiments

The open cell study of $\text{Mg}(\text{OH})_2$ decomposition and all single crystal experiments were carried out with a thermogravimetric apparatus (hereafter referred to as Apparatus A) shown in Fig. 3. A cylindrical alumina sample cell of 0.98 cm inner diameter, 2.4 cm inner height, and 1.0 mm thickness was fitted in a platinum basket which was suspended from a 1.0 mm diameter quartz rod into the tube furnace of Apparatus A. The rod was connected to a Cahn 1000 microbalance, which measured the continuous weight change to a sensitivity of 1.0 mg full scale during the decomposition. Apparatus

A incorporated a vibration isolation system and valves to control the pressure in the system during the thermogravimetric reactions. A detailed description of the back pressure control system was given by Knutsen [53].

A tube furnace wound with Kanthal wire was used to heat the sample hung in the alumina tube. The temperature was measured with a chromel alumel thermocouple which was placed near the sample cell and connected to a digital readout device. The sample was hung in a 15 cm long uniform temperature zone to minimize the temperature gradient between thermocouple and sample. Sample weight changes were measured continuously on a strip chart recorder with 1 mg, 10 mg, or 100 mg full scale. A silicone oil diffusion pump maintained the pressure of the system below 5×10^{-5} torr (6.67×10^{-3} Pa) initially and at 10^{-3} to 10^{-4} torr (0.133 to 0.0133 Pa) during the decomposition reactions. The temperature was increased to a desired decomposition temperature at a rate of about 20°C/minute. This speed of temperature increase limited the decompositions to less than 2% before the desired temperature was reached. When a desired fraction of decomposition was achieved, the furnace power was turned off to cool the sample.

When the temperature was near room temperature, the vacuum system was closed and nitrogen gas was introduced to fill the apparatus to atmospheric pressure. The product solid MgO reacts with atmospheric moisture and CO₂; therefore the sample was removed, and either transferred as rapidly as possible to the appropriate apparatus for other experiments such as surface area measurements, XRD, and SEM.

observation, or was stored in a small sealed bottle in a desiccator dried by anhydrous CaSO_4 .

Another thermogravimetric apparatus (hereafter referred to as Apparatus B) shown in Fig. 4 was used for the Knudsen cell study of decomposition of MgCO_3 . Apparatus B provided a better vacuum to 5×10^{-7} torr (6.67×10^{-5} Pa) initially and less than 10^{-5} torr (1.33×10^{-3} Pa) during the decomposition. The better vacuum is the only reason that Apparatus B is used for the Knudsen cell study. For the decomposition experiment, other functions of Apparatus B are similar to those of Apparatus A.

The Knudsen cells used in this study were made of alumina with the different orifice dimensions shown in Fig. 5.

3.3. Temperature Calibration

The rates of chemical reactions increase exponentially with temperature. Cater [52] noted that the single most likely reason that discrepancies are found in effusion data between laboratories or between experiments is inaccurately measured temperatures or lack of temperature homogeneity within the cells.

In this study, the thermocouple was located as close to the sample as possible, the separation was 10 ± 2 mm. The temperature difference between thermocouple and sample was calibrated by means of Knudsen cell experiments with a material for which the vapor pressure is well known and is of similar magnitude to the vapor pressure of the material to be studied in the range of experimental temperatures.

For the temperature calibration of Apparatus A, zinc metal powder of reagent grade was decomposed in Knudsen cells of orifice diameters 0.50 mm and 0.24 mm. The measured vapor pressures and calculated equilibrium pressures are shown in the plot of $\log P$ versus $1/T$ in Fig. 6. The range of calibrated temperatures was 615 K to 860 K. The measured pressures indicate the equilibrium pressures since they are independent of orifice areas. At temperatures lower than 690 K, the measured pressures are lower by a factor of 0.97 ($\sim 7^\circ\text{C}$ lower in temperature scale) than the equilibrium ones, and at the temperatures higher than 750 K, the measured pressures are consistent with the equilibrium ones. Therefore the measured fluxes from $\text{Mg}(\text{OH})_2$ decomposition were converted to pressures with the calibrated temperatures shown in the plot of Fig. 7 under the assumption that the extrapolation is effective down to 470 K. The measured vapor pressures from MgCO_3 decomposition were considered to be those measured at the corrected thermocouple temperatures.

The temperature calibration of Apparatus B was done with lithium iodide powder (Johnson Matthey Chemicals Limited, Royston, Hertfordshire, England), which has impurities of less than 8 parts per million by weight, in Knudsen cells of orifice diameters of 0.42 and 1.00 mm. Lithium iodide sublimes as monomer and dimer. Total LiI fluxes measured from the Knudsen cell were converted to monomeric, LiI(g) pressures which were compared with the total monomeric pressures calculated from the equilibrium thermodynamic data by the equation [54]:

$$J = \frac{P_m}{(2\pi M_m RT)^{1/2}} + \frac{2P_d}{(2\pi M_d RT)^{1/2}} = \frac{P_m(1+\sqrt{2} K_{eq} P_m)}{(2\pi M_m RT)^{1/2}}$$

where the subscripts of m and d denote monomer and dimer, respectively and K_{eq} is the equilibrium constant for the reaction of dimer formation from two monomers. The calculated equilibrium pressures in Fig. 8 are the values of $P_m(1+\sqrt{2} K_{eq} P_m)$ which are compared with the measured vapor pressures as monomeric pressures.

At temperatures lower than 770 K, the measured pressures were independent of orifice areas implying that the measured pressures are the equilibrium pressures. Above 770 K the pressures are more or less higher, depending on orifice areas, than the linearly extrapolated pressures from lower temperatures. It is known that hydrodynamic flow gives the kind of deviation to higher gas pressures observed and that hydrodynamic flow prevails for mean free paths significantly shorter than effusion orifice dimensions [50]. At 770 K the Knudsen number, the ratio of gas mean free path to orifice diameter, is calculated to be about 10 when it is assumed that the gas molecule collision cross section is ~0.5 nm. Thus the enhanced vapor pressures are believed to be due to the transition of gas flow from Knudsen flow to hydrodynamic flow at temperatures above 770 K. The linearly extrapolated equilibrium pressures measured between 710 and 770 K can serve the purpose for temperature calibration above 770 K because it is known that the enthalpy and entropy changes of the reactions do not depend on the temperature within the range of extrapolation [35]. The

calibrated temperatures shown in the plot of Fig. 9 were used for the calibration of CO_2 pressures from the decomposition of MgCO_3 in the Knudsen cells.

4. Results and Discussion

4.1. Decomposition of $\text{Mg}(\text{OH})_2$

It has been suggested that decomposition of $\text{Mg}(\text{OH})_2$ occurs only at the edge area normal to the basal (cleavage) plane [29]. In order to test this suggested reaction scheme, single crystals of $\text{Mg}(\text{OH})_2$, Brucite A, having various ratios of edge area to cross sectional area were decomposed in vacuum at 605 K. A typical weight loss curve of the single crystal decomposition is shown in Fig. 10. The initial flux densities in directions parallel to the basal plane J_1 , and normal to it J_2 were calculated from the known edge and cross sectional areas by means of the equation

$$W_{\text{total}} = A_1 J_1 + A_2 J_2$$

where W_{total} is the weight loss per unit time. Two single crystal experiments provide the ratio of the flux densities, J_1/J_2 (Table 3). The initial rate of weight loss (W_{total}), which was measured from the steady state weight loss during 3 to 10% decomposition, is not directly proportional to the edge area but is dependent on the both edge area and the area of the basal planes. At 605 K about 10% of the total flux escapes in the normal direction of the basal planes.

The observed fluxes cannot be directly assigned to these two sets of directions because of the cracking of the $\text{Mg}(\text{OH})_2$ after a small amount of decomposition. This phenomenon is discussed later. However, it can be concluded that decomposition starts from all the surfaces because the cracking cannot occur without decomposition at the area of cracking.

Another thing to note from the single crystal experiments is that at the very beginning the rate of decomposition is slower than it is after one to one and one-half hours (see Fig. 10). Thus $\text{Mg}(\text{OH})_2$ has a so-called S-curve of weight loss versus time plot. The rate increases as cracks develop in the $\text{Mg}(\text{OH})_2$ [61]. Endothermic decomposition reactions usually do not have such an incubation period if isothermal conditions have been established before decomposition begins [55]. This slow initial rate was also clearly observed with the decomposition of G&A $\text{Mg}(\text{OH})_2$ at low temperatures. Perhaps the higher surface area of G&A $\text{Mg}(\text{OH})_2$ for a given weight of $\text{Mg}(\text{OH})_2$ makes the relatively low initial rate easier to observe.

After the initial slow decomposition, both $\text{Mg}(\text{OH})_2$ single crystals and powders decomposed at a steady state to about 40% decomposition. Then the rate slowed and essentially stopped after the weight loss was ~90% (Figs. 10 & 11) so that ~10% of the initial water is retained. The sample lost more weight when heated above ~900 K, and complete decomposition was achieved at ~1200 K. The water retained after low temperature decomposition has been reported from an infrared absorption study to be adsorbed as hydroxyl ions on the MgO

surface [22]. The fact that XRD measurements and TEM observations did not find any trace of $\text{Mg}(\text{OH})_2$ or any phase other than MgO supports the conclusion from the infrared study.

The effect of quantity of sample on the rate of decomposition of G&A $\text{Mg}(\text{OH})_2$ was studied in an open cylindrical alumina crucible. Changes of sample amount (and thus powder bed depth) did not greatly change the initial steady state flux as shown in Fig. 12. The fact that the flux was nearly independent of the sample amount implies that some sort of equilibrium is approached in the powder beds. The measured fluxes were $\sim 10^{-7}$ times the maximum possible fluxes for the decomposition reaction and $\sim 10^{-3}$ times the anomalous equilibrium fluxes measured by Kay and Gregory.

Searcy et al. [25] found a similar behavior in an open cell study of calcite powder decomposition. Their measured fluxes, $\sim 3 \times 10^{-4}$ times the equilibrium fluxes, were independent of sample amount, powder bed depth, and sample packing densities. But they did not find this metastable equilibrium behavior with calcite powder of particle size greater than $100 \mu\text{m}$. For large particles of CaCO_3 , initial rates of weight loss were directly proportional to the total sample surface area, not the crucible cross sectional area. The powder sample of G&A $\text{Mg}(\text{OH})_2$ has an average particle size of $400 \mu\text{m}$, which is much greater than the critical particle size for the observed metastable equilibrium in the calcite powder decomposition. But the initial particle size of G&A $\text{Mg}(\text{OH})_2$ would not be the size when weight losses are measured because the cracking of partly decomposed

Mg(OH)_2 continuously provides Mg(OH)_2 particles of $\sim 2 \mu\text{m}$ cross section [84,117].

For further characterization of the metastable equilibrium in a powder bed of G&A Mg(OH)_2 , samples of a constant initial weight, $195 \pm 1 \text{ mg}$ were decomposed at various temperatures to obtain a plot of $\log P$ versus $1/T$. Effective flux densities (j_b) from the powder bed were calculated from weight loss measurements by means of the equation

$$j_b = \Delta W / MA\Delta t$$

where ΔW is the weight loss for the time period, Δt , M the molar weight of effusing gas, and A the cross sectional area ($= 0.754 \text{ cm}^2$) of the alumina crucible. Corresponding effective pressures calculated by use of the HKL equation were plotted as $\log P$ versus $1/T$ (Fig. 13). From the data, apparent enthalpy and entropy changes of $\sim 126 \pm 5 \text{ kJ/mole}$ and $111 \pm 9 \text{ J/mole}$ were calculated.

The apparent equilibrium in the powder beds was characterized by a greater enthalpy change than that of the standard equilibrium reaction. This fact suggests two possible explanations. One is that the reactant solid and water vapor are in equilibrium with a metastable solid phase of higher energy than normal MgO . But this high resolution TEM study showed only topotactically grown normal MgO to be formed. Furthermore, if the equilibrium involved a metastable solid the equilibrium pressures approached in the open cell and in an effusion cell with a small orifice should be the same. But the

equilibria approached in an open cell was only $\sim 10^{-3}$ times that approached in the effusion cells.

The other possible explanation is that the water pressure was set by equilibrium between the $\text{Mg}(\text{OH})_2$ and water adsorbed on the MgO surface. The persistent adsorption of water to ~ 773 K indicates that water is more strongly bound in the adsorption state than in bulk $\text{Mg}(\text{OH})_2$. The fraction of surface covered by adsorbed water changes with its pressure. It can be expected that the hindrance to escape imposed by covering the cell with a lid pierced by only a small orifice would shift the adsorption equilibrium in closed cells toward greater adsorbed H_2O concentrations and greater cell pressures as observed.

Both Kay and Gregory's Knudsen cell study and this open cell study showed metastable equilibrium behavior, with the same apparent enthalpy change within the range of experimental error but different apparent entropy changes. The lower apparent entropy change in the open cells probably results from a steady state in which a lower fraction of MgO surface sites are occupied by adsorbed water than in the Knudsen cells.

Among the previous kinetic studies Gordon and Kingery [31] reported from their thermogravimetric experiment of $\text{Mg}(\text{OH})_2$ decomposition in vacuum the same activation enthalpy of ~ 125 kJ/mole as found in this study. They found the calculated activation energy to be nearly independent of many conventional kinetic equations applied. Sharp [32] also found the calculated activation enthalpy to

be insensitive to the kinetic model chosen, but his measured activation enthalpy was ~84 kJ/mole which is identical to the standard enthalpy change of decomposition of $\text{Mg}(\text{OH})_2$. Such a coincidence in values could be explained if the equilibrium pressure were attained in the sample in Sharp's study with the rate limited by vapor phase transport [56], but Sharp's studies were conducted in vacuum.

The insensitivity of calculated activation energy to many applied kinetic models proves in itself that curve fitting to conventional kinetic equations cannot be used to identify the rate limiting step or reaction mechanism of $\text{Mg}(\text{OH})_2$ decomposition. Nevertheless, the measured activation energies should be characteristic of given experimental conditions. So the different activation energies must result from an experimental error such as using incorrect temperatures. However, an exact source of the discrepancy in the activation energy between this and other studies could not be found because other studies did not provide clear information about geometry of sample cell, particle size, and other decomposition conditions so that the flux densities could be calculated for comparison with those of this study.

4.2. Decomposition of MgCO_3

Single crystals of Magnesite B were cleft to produce the characteristic rhombohedral angle (103.33°) of their cleavage unit cells and they were decomposed in Apparatus A. Typical weight loss curves are shown in Fig. 14. An SEM observation of a partly

decomposed single crystal showed the reaction interface to have the same contour as initial crystal surface (Fig. 61B), implying that the reaction interface moves inward at the same rate from each magnesite crystal surface. Therefore, for a certain scale thickness of porous product MgO the fraction of decomposition can be obtained from the ratio of the volume decomposed to the initial volume of MgCO_3 crystal. Alternatively the MgO scale thickness can be plotted versus decomposition time measured from the weight loss curve.

As shown in Fig. 14, the MgO scale thickness increased linearly with time to near complete decomposition. The flux remains directly proportional to reaction interface area. This fact implies that a chemical step of the decomposition process is slower than gas phase diffusion through the porous MgO scale [10]. Although the size of individual MgO particles is ~ 3 nm as shown in Fig. 51 and the pore size between the particles may be small enough to resist gas phase diffusion, cracking or aggregation of such small particles shown in Figs. 59-61 may provide alternate routes to reduce the resistance to gas phase diffusion.

The initial fluxes from single crystal surface were about 10^{-8} times the thermodynamic equilibrium fluxes. The corresponding plot of $\log P$ versus $1/T$ is shown in Fig. 16. The plot is curved near 825 K: The curvature is too great to be due to an experimental error. The curvature of the plot implies that the rate limiting step of decomposition at higher temperatures is different from that at lower temperatures. At temperatures higher than 825 K, the

calculated ΔH and ΔS are 170 ± 5 kJ/mole and 73 ± 6 J/mole-deg., respectively. At temperatures lower than 825 K, ΔH and ΔS are 270 ± 10 kJ/mole and 194 ± 13 J/mole-deg., respectively.

The apparent enthalpy changes from the higher and lower temperature ranges are ~ 57 kJ/mole and ~ 157 kJ/mole greater than that of the standard equilibrium reaction, respectively. Regardless of the temperature range, decomposition of single crystal MgCO_3 proceeded irreversibly as implied by the linear growth of porous MgO scale with time (Fig. 14) so that presumably no product is in equilibrium with the reactant.

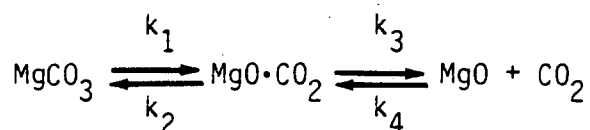
The entropy change of the reaction depend primarily on the number and kinds of gas molecules produced or consumed in a reaction [57]. Since in the lower temperature range the apparent entropy change is close to the standard entropy change for the decomposition of MgCO_3 , (175 J/mole-deg.), the rate determining step in the lower temperature decomposition probably involves formation of CO_2 gas. By the same reasoning, the rate determining step in the higher temperature decomposition should be an earlier step that does not involve CO_2 gas production.

Beruto et al. [58] found the enthalpy and entropy changes for adsorption of CO_2 on an MgO surface to be 216 ± 5 kJ/mole and 190 ± 10 J/mole-deg., respectively for the adsorption reaction at the higher coverage state (83% coverage). They noted that errors in determining the activation enthalpy are greater at the higher degree of coverage because of the asymptotic shape of the adsorption isotherms, and a

calculated variation of about 60 kJ/mole was found for only 3% variation of coverage from 83%. The higher enthalpy for the adsorption indicates that CO₂ is bound more strongly on MgO than in MgCO₃.

Considering Beruto et al.'s finding and the fact that the driving force for an exothermic adsorption reaction is increased with a decrease of temperature, the rate determining step of the lower temperature decomposition of MgCO₃ single crystal may be the desorption of CO₂ from an adsorbed state.

If the decomposition is considered as a two-step process involving the adsorbed state (MgO·CO₂), the reaction equation is expressed as follows



where k is the reaction rate constant for each elementary reaction step. For an irreversible reaction in vacuum, the rate of reaction step 4 can be neglected. Then the decomposition flux (J) is given by the following equation [43]

$$J = k_1 k_3 / (k_2 + k_3)$$

When k₂ is much greater than k₃, the intermediate MgO·CO₂ is near equilibrium with the MgCO₃. Desorption is the rate determining step but the apparent rate constant is (k₁/k₂)k₃. The apparent activation enthalpy is (ΔH₃^{*} - ΔH₂^{*} + ΔH₁^{*}) and the apparent entropy, (ΔS₃^{*} - ΔS₂^{*} + ΔS₁^{*}) has a value consistent with expectations for a

reaction that produces CO_2 gas. In the higher temperature decomposition, the desorption step cannot be the slowest step; k_3 must be greater than k_2 , and the rate determining step must be an earlier step of the process, reaction step 1 of the model [43].

While the decomposition of single crystals of MgCO_3 gave nearly linear weight changes with decomposition time to ~50% decomposition, the decomposition of powder samples in the alumina open cell was retarded at early stages of decomposition (Fig. 15). When the weight of sample was increased from 187.5 mg to 1313 mg, the initial flux was increased by a factor of 3 at 803 K. This change of flux with change of sample amount also implies that a near-equilibrium state like that observed in the decomposition of $\text{Mg}(\text{OH})_2$ is not established in the powder bed. A measurement of surface area for a 20% decomposed sample of 1313 mg proved that every particle in the powder bed contributes more or less to the observed flux since the surface area of sample from the top portion of powder bed was $80 \text{ m}^2/\text{g}$ and that from the bottom portion of powder bed was $25 \text{ m}^2/\text{g}$. If decomposition were completely irreversible in the isothermal bed, surface areas should be the same for powders sampled from the top of the bed as from the bottom [59]. If an complete equilibrium were established in the powder bed, the surface area from the bottom portion of powder bed should be close to that of initial undecomposed sample which is $\sim 3 \text{ m}^2/\text{g}$ in this case [25].

When powder samples were decomposed in Knudsen cells, the flux was still dependent on sample amount. The dependence was smaller at the higher decomposition temperatures. As shown in Fig. 16 of which the Knudsen cell data were obtained from the powder sample of 185 ± 1 mg, at the higher temperatures the fluxes were constant until 5% decomposition. At the lower temperatures they were sharply decreased at lower fraction of decomposition.

Now the question is why a more reversible state is approached as the decomposition temperature is increased. The reason may be found from the Whitman-Motzfeldt equation

$$(P_{eq}/P_K) = 1 + (W_B B/\alpha A)$$

If the curves for 2 to 3% and 4 to 5% decomposition are considered, (P_{eq}/P_K) is greater at the lower temperatures. Since $W_B B$ is independent of the temperatures, αA must decrease as the temperatures are decreased. But the effective surface area of sample is increased under the more irreversible condition of lower temperature decompositions. Therefore, the decomposition coefficient (α) must decrease with the decrease of temperatures, in agreement with observations of the Langmuir experiments with single crystals of $MgCO_3$.

Although the initial fluxes only approach steady state, plots of $\log P$ versus $1/T$ are linear for 0 to 1% decomposition. The plots yield apparent enthalpies of 105 ± 5 kJ/mole and 109 ± 5 kJ/mole for data taken with orifice diameters of 0.21 and 0.42 mm, respectively. These

apparent enthalpies are close to the standard enthalpy change of 113 kJ/mole. From the near agreement in the enthalpies one might think that the initial fluxes are characteristic of the standard equilibrium. But the initial fluxes cannot result from equilibrium between MgCO_3 , normal bulk MgO , and CO_2 gas because the fluxes are dependent on sample amount, and the extrapolated pressures to zero orifice area are only about 10^{-1} times the standard equilibrium pressures. So a clear interpretation of the effusion data is not possible at the present state of this study.

III. TEM STUDIES

1. Introduction

Decomposition reactions of some hydroxides and carbonates have long been known as topotactic reactions [60] in which three dimensional orientation relationships are observed and the initial crystal shape is conserved by an open framework of small particles and pores. The specific surface areas of product solids of such decomposition reactions are usually very high. Thus high surface areas are exploited in many industrial applications such as catalysis, gettering of detrimental gases, and sintering, etc. However, investigations of the decompositions that yield these porous solids have left unsettled a variety of controversial issues, e.g., the decomposition mechanism [83,84,99], the lattice parameters of product solids [91,93], the particle shapes and sizes of product solids [97], and the nature of cracking phenomena [84,117] during the decomposition, etc.

As mentioned in the general introduction, the primary objective of this study is to seek understanding of the reaction mechanisms of $\text{Mg}(\text{OH})_2$ and MgCO_3 decompositions. Since complete understanding of a reaction mechanism requires a detailed description of each elementary reaction step, an ideal method of studying a decomposition mechanism from a structural point of view is to trace the movement of each atom during the decomposition. Although there is no such tool by which such detail can be investigated, a decomposition path can be

deduced from observations of structural and morphological changes during the reactions.

Crystal structures can be identified from measurements of the diffraction of X-rays, neutrons, or electrons. Of these methods, only electron waves can be focussed to make morphological studies possible at a very high magnification. The limit of resolution is set by the equation

$$R = \frac{0.61\lambda}{\alpha}$$

where R is the size of the resolved object, λ is the wavelength, and α is identical to the effective aperture of the objective lens [62].

One possible explanation of the anomalously low apparent equilibrium H_2O pressures during $Mg(OH)_2$ decomposition in effusion cells is that a metastable solid phase was formed, but was present in amounts too small to be detected by X-ray diffraction. The scattering power of crystals for electrons is about four orders of magnitude greater than for X-rays [63]. This strong scattering power makes it possible to identify the material present in a very small volume element and thus makes it possible to use electron diffraction to detect any metastable phase which is present in layers as little as a few unit cells thick. For this reason, transmission electron microscopy (TEM) is best suited for detailed structural study of decomposition reactions as it is for most other solid-solid phase transformations [65]. Accordingly, the characteristics of the product

solids of $\text{Mg}(\text{OH})_2$ and MgCO_3 decompositions and their orientation relationships to the parent solid have been carefully explored mainly by TEM but with use of X-ray, SEM, N_2 -adsorption apparatus as supporting tools.

2. Background

Knowledge of crystal structures is indispensable information for understanding decomposition reaction. When the crystal structures of solids involved in the reaction are known, a path of the structural transformation from a reactant solid to its product solid can be identified from study of electron diffraction patterns and of morphologies by TEM. Accordingly, reactant and product crystal structures and the methods of structural study of decomposition reactions by TEM are reviewed as basic background.

2.1. Crystal Structures of $\text{Mg}(\text{OH})_2$, MgCO_3 , and MgO

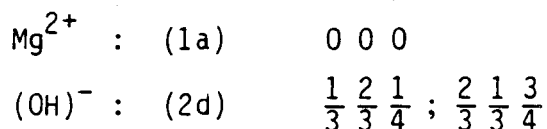
2.1.1. $\text{Mg}(\text{OH})_2$ Structure

$\text{Mg}(\text{OH})_2$ has a CdI_2 type structure in which Mg^{2+} ions form a primitive cell and $(\text{OH})^-$ ions form a close packed hexagonal cell [66,67]. The unit cell and the coordination of ions are shown in Fig. 17. A layer structure is formed by the stacking of a series of composite layers of $(\text{OH})^- \text{Mg}^{2+} (\text{OH})^-$ ions. The coordination octahedra lie in a sheet which allows each $(\text{OH})^-$ ion to be shared by three Mg^{2+} ions. Ions are asymmetrically coordinated: Mg^{2+} ions lie on only one side of each $(\text{OH})^-$ ion layer. The sheet formed of

two $(\text{OH})^-$ layers separated by an Mg^{2+} ion layer is electrically neutral because there are $6N/3 = 2N$ $(\text{OH})^-$ ions in the sheet containing N Mg^{2+} ions. Such a sheet can, therefore, be regarded as a molecule of infinite extent in two dimensions and is loosely bonded to neighbor sheets. This bonding configuration results in the easy cleavage along (0001) planes.

The asymmetric coordination of hydroxyl ions in the $\text{Mg}(\text{OH})_2$ structure must inevitably produce considerable polarization, and a more faithful picture is therefore that of a cylindrical dipole [66]. These dipoles contribute to bonding between layers. As expected from this argument, neutron diffraction studies have shown the hydrogen atoms to be 0.0995 nm from the oxygen atoms in a direction parallel to the c-axis and away from the plane of the Mg^{2+} ions [69].

Although the exact shape and position of the hydroxyl group is known from neutron diffraction, to a good approximation the $(\text{OH})^-$ ion behaves and can be considered as a spherical entity of radius 0.153 nm (intermediate in size between F^- and Cl^- ions). Accordingly, the position of ions in the hexagonal unit cell is generally described as follows:



Interatomic distances are reported in the literature [69]. Other relevant crystallographic information is listed in Appendix 1 [70].

2.1.2. MgCO_3 Structure

MgCO_3 has a rhombohedral structure of the calcite type, which can be described as a distorted NaCl structure formed by stretching along the triad axis [66]. The distortion of a cube is necessary to accommodate the large planar CO_3^{2-} ions each of which contains a carbon at the center of an equilateral triangle of oxygens. The planes of the CO_3^{2-} ions are all perpendicular to the triad axis of the unit cell, therefore the structure can be considered to have alternating layers of Mg^{2+} ions and CO_3^{2-} ions positioned perpendicular to the triad axis. The CO_3^{2-} ions in the alternate layers are rotated 180 degrees about the triad axis. Each Mg^{2+} ion is coordinated by six oxygen neighbors belonging to six different CO_3^{2-} ions (Fig. 20) [71]. The cleavage cell or morphological rhombohedron of four formula units shown in Fig. 21 is not the smallest unit cell. The unit cell having two formula units in it can contain the full identity period of CO_3^{2-} ions which are imposed with opposite orientations along the triad axis. The other two unit cells represent only half the identity period of CO_3^{2-} ions. Hence, the two formula cell can be considered as the true unit cell of the calcite type structure since it has the smallest volume having the full identity of CO_3^{2-} ions [71]. This two formula unit cell can be transformed to the hexagonal structure as shown in Fig. 19.

Transformation of indices following a change of unit cell is achieved with a transformation matrix by the method described in the literature [72]. The matrices for the transformation of unit cells of

MgCO₃ of 6 formula unit are summarized in Appendix 2. In this study, the hexagonal unit cell (Fig. 18) is used for all the crystallographic notations of the MgCO₃ structure to be consistent with usual practice [71]. The indices of a hexagonal structure can be described with Miller or Miller-Bravais notations [73,74]. Appendix 3 lists the equations relating Miller and Miller-Bravais indices and also the crystallographic relations of direct and reciprocal lattice for the hexagonal system.

Atomic positions in the hexagonal unit cell of MgCO₃ are as follows with Wyckoff notation [68]:

$$\text{Mg : (6b) } \pm(0 \ 0 \ \frac{1}{4}) ; \text{ rh}$$

$$\text{C : (6c) } \ 0 \ 0 \ 0 ; 0 \ 0 \ \frac{1}{2} ; \text{ rh}$$

$$\text{O : (18e) } \ U \ 0 \ 0 ; 0 \ U \ 0 ; \bar{U} \ \bar{U} \ 0 ; \bar{U} \ 0 \ \frac{1}{2} ; 0 \ \bar{U} \ \frac{1}{2} ; U \ U \ \frac{1}{2} ; \text{ rh}$$

$$\text{with } U = 0.2769$$

where the symbol rh means that the coordinates with respect to hexagonal axes are to be repeated about $\frac{1}{3} \ \frac{2}{3} \ \frac{2}{3}$ and $\frac{2}{3} \ \frac{1}{3} \ \frac{1}{3}$.

Interatomic distances were reported in the literature [75] and other relevant crystallographic information is listed in Appendix 1.

2.1.3. MgO Structure

MgO has the NaCl structure of which the Bravais lattice is face-centered cubic (FCC) since each ion makes the FCC structure. Fig. 22 shows the arrangement of the ions in the cubic unit cell of

MgO which has alternating layers of Mg^{2+} ions and O^{2-} ions along the [111] direction. This unit cell contains 8 ions, located at the lattice points which are interchangeable with translations of half-lattice parameter, as follows:

$$\begin{array}{l} Mg : (4a) \quad 0 \ 0 \ 0 ; \frac{1}{2} \ \frac{1}{2} \ 0 ; \frac{1}{2} \ 0 \ \frac{1}{2} ; 0 \ \frac{1}{2} \ \frac{1}{2} \\ O : (4b) \quad \frac{1}{2} \ \frac{1}{2} \ \frac{1}{2} ; \frac{1}{2} \ 0 \ 0 ; 0 \ \frac{1}{2} \ 0 ; 0 \ 0 \ \frac{1}{2} \end{array}$$

Each ion in the MgO is coordinated by six oppositely charged ions disposed at the corners of a regular octahedron. The MgO structure can thus be regarded as formed by the cubic close packing of the large oxygen ions with the octahedral interstitial positions all filled with cations.

Other relevant crystallographic information is listed in Appendix 1.

2.2. Structural Study of Decomposition Reactions by TEM

Many specific TEM techniques could be used to study decomposition reactions depending on a particular solid to be decomposed. The main TEM techniques for the reaction can conveniently be classified into electron diffraction studies and morphological observations.

2.2.1. Electron Diffraction

Electron diffraction described by the Fourier transformation of real crystals makes the reciprocal lattice of which the lattice points lying on (or close to) the surface of the Ewald sphere satisfy Bragg's

law and their intensities are proportional to the square of the structure factor, F_g defined by

$$F_g = \sum_j f_j (\sin \theta/\lambda) \exp (2\pi i g \cdot r_j)$$

where $f_j (\sin \theta/\lambda)$ is the atomic scattering factor of j th atom for the angle concerned, this atom being at the position r_j [62].

The electron diffraction patterns recorded on the photographic plate are indexed by the general procedure described in textbooks [62-64,76]. If any spots in addition to the expected ones from reactant and product solids arise, these additional spots may be caused by an intermediate phase or phases although there are many different origins possible for extra reflections.

A symmetrical diffraction pattern provides the orientation of a crystal. If a product solid of a decomposition reaction gives a diffraction pattern of spots or gives inhomogeneous intensity distributions of ring patterns, an orientation relationship can be determined by finding the orientation of symmetrical patterns of the reactant and product solids. Once the orientation relationship is found, one can make the corresponding stereographic projection in which the angular relationships of crystallographic planes of reactant and product solids are easily identified. The orientation relationship, which is usually expressed in terms of parallel planes and directions, provides a basis to determine if any invariant planes, lines or lattice sites are possible within the observed orientation relationship. It is established that such a matched structural unit

provides a least energy path for the solid-solid phase transformation [77-79].

2.2.2. Morphological Observations

In addition to the structural study by electron diffraction, morphological observations can provide information about the decomposition mechanism.

If a specimen is stable under an electron beam for the period of an analysis, contrast arising from defects related to the decomposition can be identified by the usual contrast analysis technique, i.e., dislocations at the reaction interfaces are identified by two beam tilting experiments so that the decomposition mechanism can be deduced in combination with observations of the orientation relationships.

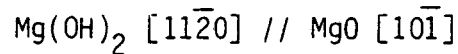
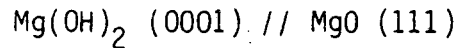
Niepce et al. [80] argued that a study of the state of division of the product solid can be used to detect the structural transformation mode which has caused that fragmentation to occur. TEM studies at high resolution can give direct information about the particle size, shape, and arrangement in space which they identify as needed.

Besides the contrast analyses and direct observations of morphological changes of reactant to product solids, dark field, Moiré fringes, stereomicroscopy, and high resolution techniques can also be helpful in understanding a reaction scheme if those techniques are applicable to a specific decomposition reaction.

3. Previous Studies

3.1. Orientation Relationships

The orientation relationship of Mg(OH)_2 decomposition is well established by X-ray and TEM work as follows [81-85];



Only Garrido [82] reported a variant in this orientation from his X-ray diffraction experiment. He observed two orientations. Orientation I is the one described above. Orientation II has intensities one-fourth as strong as orientation I and is rotated 60 degrees from orientation I about the [0001] direction of Mg(OH)_2 . He argued that this second orientation variant might result from a typical transformation twin. He suggested that the different intensities might result from the fact that in crystals having orientation I the Mg-O bonds have the same orientation as in the Mg(OH)_2 , while in crystals of orientation II the Mg-O bonds are rotated 60 degrees around the c-axis of Mg(OH)_2 from the directions the bonds had in the Mg(OH)_2 .

While only Garrido disagrees about the orientation relationship of Mg(OH)_2 decomposition, there is no general agreement about that of MgCO_3 decomposition. The previous studies are summarized in Table 4.

3.2. Lattice Parameter of Product Solid MgO

The lattice parameters of MgO from the thermal decomposition of Mg(OH)_2 and MgCO_3 were carefully measured by X-ray and TEM for two

different reasons, i.e., one for the decomposition study and the other for the effect of particle size on the lattice parameter.

From a decomposition study of $\text{Mg}(\text{OH})_2$ by TEM, Goodman [83] reported that during the first stage of the decomposition, the Mg-Mg distance in the basal plane of $\text{Mg}(\text{OH})_2$ changed from 0.312 nm ($\pm 0.5\%$) to 0.299 nm ($\pm 0.5\%$), exactly the distance required in the (111) plane of MgO. If his findings are correct, MgO produced from the decomposition has the normal lattice parameter from the start of the reaction.

Contrary to Goodman's observation, Gordon and Kingery [84], who also used TEM, found a gradual decrease of the lattice parameter of MgO during the decomposition from the parameter corresponding to the Mg-Mg distance in the (0001) plane of $\text{Mg}(\text{OH})_2$ to that of normal MgO. According to them, this variation was caused by a coherent interface reaction which produces about 4.5% shrinkage of Mg-Mg distance within the observed orientation relationship.

The lattice parameters to be expected of small particles have been a subject of controversy. Different theoretical calculations of the lattice parameters of small crystals of NaCl structure yielded contradicting predictions: Some calculations [86,87] predicted a contraction of the lattice parameter and others [88,89] a dilation of the lattice parameter as particle size becomes smaller. Earlier experimental work was also divided on whether the lattice spacings of small particles are decreased [90,91] or increased [92,93] from those of large particles.

Nicolson [86] calculated that there should be a lattice contraction in small ionic crystals. Using X-ray diffraction methods, he found only a small decrease in lattice parameter in MgO from MgCO_3 decomposition in air, but a marked decrease when the decomposition was carried out in vacuum. Nicolson suggested that even under vacuum there was incomplete removal of contamination from the surface.

Guilliatt and Brett [91] observed similar results with MgO prepared in vacuum from MgCO_3 decomposition and from Mg(OH)_2 decomposition, respectively, but found an expansion of the lattice when the crystals were exposed to air. This expansion of lattice was explained in terms of a dilatant volume stress imposed by a surface hydroxyl layer around the MgO crystallites.

While a lattice contraction was observed from small particles of MgO without contamination on the surface, Halliday et al. [92] observed by TEM a lattice dilation from crystals of LiF in the size range of 5-12 nm. Other alkali halides examined have been found to have normal lattice constants, although the particle size of the specimens studied was in no case less than 10 nm.

3.3. Morphological Observations

Single crystals of Mg(OH)_2 , MgCO_3 , and MgO are clean and transparent in optical observations. Goodman [83] observed a messy contrast by TEM. He concluded that the mottled appearance of his MgO must be due to a substructure within the crystal. Brindley and Ogilvie [94] have shown that brucite has a texture with a small

rotation of crystallites about the a-axis. Such a rotation would make some crystallites diffract electrons much more strongly than others. However, Goodman did not undertake a full contrast analysis to identify the mottled contrast. Other workers did not comment at all about it, probably because it was absent in their specimens. The reaction interface, which might exist in the $\text{Mg}(\text{OH})_2$ decomposition, had not been resolved by TEM in any previous study although Anderson and Horlock [29] showed isolated point sources in the partly decomposed brucite with an optical micrograph.

The shapes of MgO crystallites from the decomposition of $\text{Mg}(\text{OH})_2$ and MgCO_3 have been generally assumed to be cubic since the (100) surface has the lowest surface energy and is electrically neutral. With a TEM, Moodie and Warble [95,96] observed cube-like shapes for MgO obtained from the decomposition of basic magnesium carbonates ($4\text{MgCO}_3 \cdot \text{Mg}(\text{OH})_2 \cdot 4\text{H}_2\text{O}$) and from the oxidation of magnesium metal powders. However, they did not obtain clear observations of the particle shape of MgO from $\text{Mg}(\text{OH})_2$ or MgCO_3 decompositions. These parent solids may have a different path of decomposition to MgO from that of the basic magnesium carbonate. Guilliat and Brett [97] assessed the shape of MgO crystallites prepared from the thermal decomposition of $\text{Mg}(\text{OH})_2$ by the variance method of X-ray profile analysis. They concluded that the microcrystals of MgO are not perfectly cubic as is commonly supposed, but are best approximated by octahedral shape. Guilliat and Brett also calculated the MgO

crystallite size from Fourier integral breadth measurements of X-ray line profiles, and found the size to be dependent on the parent hydroxide plate thickness with a lower limit of ~5 nm. Other X-ray measurements and TEM observations yielded several different larger sizes of MgO crystallites, depending on the process conditions of the decompositions. Only Goodman reported MgO of sizes smaller than 5 nm, i.e., 2 to 4 nm, but without clear evidence, in his TEM experiment.

An interesting phenomenon known as polycrystallization [29] or cracking [84] as mentioned before has been observed in the decomposition of $\text{Mg}(\text{OH})_2$. The cracking was suggested to occur because of an accumulated strain at the semi-coherent reaction interface, but definite evidence of the exact origin was not obtained.

There are no pertinent morphological studies for the decomposition of MgCO_3 except Dai's TEM experiment in which the approximate size of MgO particles was estimated to be ~5 nm [98]. The shape of MgO from MgCO_3 decomposition has never been clearly resolved by any visual techniques.

3.4. Suggested Decomposition Mechanism

3.4.1. Mechanisms of $\text{Mg}(\text{OH})_2$ Decomposition

Three different mechanisms of $\text{Mg}(\text{OH})_2$ decomposition have been suggested in the literature, i.e., a homogeneous mechanism, an inhomogeneous mechanism, and a nucleation and growth mechanism.

3.4.1.1. Homogeneous Mechanism

Goodman [83], on the basis of his TEM study, proposed that H₂O vapor is formed by combining adjacent (OH)⁻ ions in every hexagonal unit cell of Mg(OH)₂ that the H₂O vapor diffuses away from in the crystal. Goodman's model is often referred as the "homogeneous mechanism". It would require that only slight shrinkage (~5%) occur in the basal plane and large shrinkage (~49%) occur along the c-axis during the H₂O formation in every unit cell of Mg(OH)₂ in order to allow the Mg²⁺ ions to shift their positions in brucite to the positions required in MgO. The resultant strain can then be responsible for the maze of cracks that form in the Mg(OH)₂ crystal. Then a collapse of the planes down the original <0001> direction of the Mg(OH)₂ crystal produces small crystallites of MgO. This collapse, according to Goodman, is controlled by the migration of water molecules from between basal planes to a surface where they can escape. However his electron diffraction work was made only with the electron beam parallel to the [0001] direction of Mg(OH)₂ crystal. This orientation cannot give any structural information about the c-axis of Mg(OH)₂. All the other TEM studies [29,84] also report only diffraction patterns with this orientation, perhaps because of the difficulty of preparing specimens or of producing high angle tilting of specimen at the time of their studies.

Anderson and Horlock [29] supported the homogeneous mechanism on the basis of their TEM study with similar observations of a change of Mg-Mg distance in the (0001) plane of Mg(OH)₂ to that in the cubic MgO

structure. They envisaged the reaction as occurring in three stages: During the initial stage, some perturbation of the hydroxide lattice results from the interaction of adjacent hydroxyl ions, and this perturbation may involve dimensional changes and consequent stresses which result in the observed polycrystallization phenomenon without loss of water. This primary process is followed by removal of water from the minute crystals, and finally crystallization of the dehydrated product occurs with the formation of MgO crystallites in the size range of 7.5-10 nm.

Niepce et al. [80] obtained X-ray measurements of the state of division of CdO from the decomposition of $\text{Cd}(\text{OH})_2$, which has the same structure as $\text{Mg}(\text{OH})_2$. They argued from these results that MgO crystallites produced by such a homogeneous mechanism would be formed via a shear transformation requiring only reordering of Mg^{2+} and O^{2-} ions without any long range diffusion of ions. From a high temperature X-ray analysis of the decomposition of $\text{Mg}(\text{OH})_2$ powder, Freund and Spering [100] found the survival of (0001) and $(11\bar{2}0)$ reflections of $\text{Mg}(\text{OH})_2$ beyond the time which produced substantial dehydration until nearly anhydrous MgO was formed. They found a shift of these reflections with increasing temperature with little or no line broadening. They attributed the observed survival of $\text{Mg}(\text{OH})_2$ reflections to a nearly anhydrous high defect MgO of the brucite structure. They suggested that this defect MgO of relict structure collapses progressively to the cubic MgO during the decomposition.

This model is essentially the same as the Niepce and Wattle's shear transformation mechanism [99] and also as the homogeneous mechanism suggested by Goodman.

3.4.1.2. Inhomogeneous Mechanism

Ball and Taylor [101] proposed another mechanism, one known as the inhomogeneous mechanism. This mechanism was proposed to explain X-ray observations of an apparent intermediate phase of spinel structure. The reaction was assumed to occur simultaneously throughout the bulk of the $\text{Mg}(\text{OH})_2$ crystal. That reaction was suggested to cause later separation into "donor" and "acceptor" regions by migration of Mg^{2+} ions from the donor to the acceptor regions with counter migrations of protons. Finally, the acceptor regions become MgO crystallites while protons combine with hydroxyl ions to form water molecules which escape from the donor regions leaving inter-crystalline pores. Ball and Taylor hypothesized that the intermediate phase of spinel structure would be formed during the migration of some cations into tetrahedral sites formed at some early stage by a slip of hexagonal close packed oxygen layers into cubic close packed layers. They favored this proposed mechanism over the homogeneous mechanism because it accounted for the occurrence of the intermediate phase, required less rearrangement of structure for the observed topotaxy, could be accomplished by migrations of small cations and protons instead of H_2O molecules, and could account for a porous decomposition product which consists of fine crystallites of MgO . However, later the X-ray

reflections of the spinel structure was shown to be due to the reaction of Fe impurities to form MgFe_2O_4 [102]. Therefore, this mechanism seems to be invalid.

3.4.1.3. Nucleation and Growth Mechanism

A third mechanism was proposed by Gordon and Kingery [84] from electron and optical studies of $\text{Mg}(\text{OH})_2$ decomposition in which they interpreted the reaction as a normal nucleation and growth process: MgO nuclei form coherently with the brucite matrix introducing large strains, and cause extensive fissuring (cracking or polycrystallization of $\text{Mg}(\text{OH})_2$). The basis for this mechanism, according to Gordon and Kingery, is, besides the cracking of $\text{Mg}(\text{OH})_2$ at a time much of the water is still present, the observation of electron diffraction spots of MgO which show a gradual decrease of Mg-Mg distances from those in $\text{Mg}(\text{OH})_2$ to the distance in normal MgO .

Librant and Pampuch [103] gave a similar interpretation from their study of decomposition of magnesium compounds (hydroxide, carbonate, basic carbonate, and oxalate) by means of X-ray and infrared; an intermediate phase of hybrid crystals, in which the transformed and untransformed regions coexist coherently without the establishment of phase boundaries, is continuously transformed into new phases in topotactic decomposition reactions such as $\text{Mg}(\text{OH})_2$ and MgCO_3 .

3.4.2. Mechanisms of MgCO_3 Decomposition

As shown in Table 4, the orientation relationship of MgCO_3 decomposition has not been settled [104-107]. Nevertheless, some mechanisms based on crude evidence and assumptions have been suggested.

From comparison of the structure of MgCO_3 and MgO and from his observed orientation relationship, Dasgupta [104] suggested the following mechanism: When MgCO_3 is heated, CO_2 escapes from the CO_3^{2-} layers. As a result strain is produced along the three-fold axis. With the complete expulsion of CO_2 , the rhombohedral cell changes into a cubic cell of periclase. Thus a three-fold axis of the magnesite becomes a three-fold axis of the periclase with three diad axes of both phases being interchanged.

Oh et al. [107] observed four preferred orientation relationships from their X-ray study of MgCO_3 decomposition (Table 4). They presumed that those periclase crystals which formed with the orientations (2), (3), and (4) consisted of three kinds of equivalent individuals which were related by the three-fold axis of the original magnesite. They also suggested a possible mechanism for the formation of periclase pseudomorphs of magnesite: The nuclei of periclase initially form epitaxially on the magnesite surface either by vapor deposition or by the occasional formation of periclase nuclei at the reaction boundary. These epitaxial nuclei then grow into an aggregate of oriented periclase crystals.

4. Experimental Procedures

4.1. Materials

The materials used in this study are indicated in Table 2. Among them, Brucite A, which provided large pieces of single crystal, was used for $\text{Mg}(\text{OH})_2$ decomposition unless otherwise noted, and Magnesite B alone was used for MgCO_3 decomposition since it was formed of single crystals.

4.2. Preparation of TEM Specimen

Insulating materials such as $\text{Mg}(\text{OH})_2$, MgCO_3 , and MgO undergo electron charging [108] when they are exposed to an electron beam, and they are also so brittle that they can not be shaped into discs which fit into the specimen holders. These problems were overcome by using a conducting aid and a specimen supporting grid, respectively. All the TEM specimen were sandwiched with 150 mesh copper folding grids of which one inner side had been covered with a thin carbon film. The resistance heating of a graphite rod in vacuum produces carbon vapor which is deposited on the glass or mica plates to make a thin film. The deposited film, scored with a sharp blade into about 2x2 mm squares, was put into water and separated from the substrate plates by exploiting the hydrophobic and hydrophilic behavior of carbon and the substrate plates, respectively. The carbon films floated on water and were caught on one side of a folding grid to support a specimen with the sandwiched arrangement. This sandwiched arrangement of specimen effectively prevented electron charging of the non-conducting materials.

Specimens of $\text{Mg}(\text{OH})_2$ were prepared by a cleavage method, a dispersion of small particles, and an ion-beam milling.

Single crystals of $\text{Mg}(\text{OH})_2$ are easily cleaved along their (0001) habit plane because of the bonding described in the Background section. An adhesive tape was attached to a crystal and was removed with crystal flakes adhering to the tape. A suitably thin specimen was picked to be sandwiched as described above. This method provided enough thin sections for the TEM works.

Precipitated $\text{Mg}(\text{OH})_2$, dispersed in an organic liquid, methanol or acetone, was dropped on the carbon film with an eye dropper. As the liquid evaporated, small particles of $\text{Mg}(\text{OH})_2$ remained stuck to the carbon film. Some particles were thin enough to make TEM observations possible.

The two methods described above provided only orientations with the (0001) plane approximately normal to the electron beam because of the plate shape of the specimens. The specimen can be tilted enough to yield information about the lattice parameter of the c-axis, but not enough to give morphological observations about the planes which are normal to the (0001) habit planes. It is these normal planes which undergo about 50% shrinkage in interplanar distance of Mg^{2+} layers during the decomposition to produce the observed orientation relationships. For observations of these normal planes, the specimen

of $\text{Mg}(\text{OH})_2$ should be a thin plate of which the orientation is normal to c-axis of $\text{Mg}(\text{OH})_2$ or within the limit of tilting of the stage ($\pm 30^\circ$).

To this end, specimens were prepared by ion-beam milling. Thin plates for ion-beam milling can only be cut at a maximum angle of ~ 60 degrees from the habit plane because of the highly anisotropic bonding. The tilting stage permitted observation of the desired orientations and the associated morphological changes with the specimens.

The apparatus for ion-beam milling has been described in the literature [119]. The optimum conditions for the initial milling of a section ground to $\sim 30 \mu\text{m}$ thick with argon ions turned out to be an accelerating voltage of 6 KV, a total beam current of 0.4–0.6 mA, and an angle of incidence of the beam on the specimen of 20–22 degrees. With these conditions it usually took 8 to 10 hours to perforate the specimen. After the sample was perforated, the accelerating voltage was reduced to 5 KV, the total beam current to 0.3 mA, and the angle of incidence to 12 degrees for 1 to 2 hours to remove some of the surface damage on the specimen caused by ion-beam milling at the higher voltage. All the ion milling was done with a Gatan cold specimen stage, which is connected to liquid nitrogen, in order to prevent the decomposition of the specimen by the substantial heating that arises during the ion-beam milling.

All the specimens of MgCO_3 were prepared by ion-beam milling with conditions similar to those used for the $\text{Mg}(\text{OH})_2$ specimens. Although MgCO_3 powders, prepared by grinding of single crystals and dropped onto the carbon film, were tried for TEM observations, they were not so effective as the specimen prepared by ion-beam milling. For the in-situ calibration of lattice parameters gold was deposited to the thickness of 10-30 nm on the specimens prepared by the methods described above.

4.3. Transmission Electron Microscopy (TEM)

The specimens were examined in Philips 301, Hitachi 650, Siemens 102, and JEM 200CX microscopes to get maximum information by taking advantage of the design capability of each microscope.

Most conventional TEM work such as diffraction analysis and morphological observation was done with the Philips 301. The in-situ decompositions of $\text{Mg}(\text{OH})_2$ and MgCO_3 crystals were achieved in this microscope by electron beam illumination, which is known to be effective for specimen heating [108]. The orientation relationships were checked by the normal procedure described in the Background section. Sequential diffraction patterns and morphological changes during the decompositions were recorded on plastic films. At least two different orientations were used to reveal the decomposition behavior in three dimensions. Special attention was given to observe any change that might arise from an intermediate reaction product or products. A cold specimen stage at liquid nitrogen temperature,

designed for this microscope, was used to determine the morphology, i.e., contrasts of the initial undecomposed $\text{Mg}(\text{OH})_2$. Specimens of $\text{Mg}(\text{OH})_2$ decompose so quickly under a moderate intensity of electron beam that the observed initial contrasts without such a cold stage cannot be assumed to result from the inherent initial structure of the specimen.

The Hitachi 650 is a high voltage electron microscope in which the maximum accelerating voltage is 650 KV. The advantages of high voltage microscopes are well listed in the literature [62]. The greater penetration depth obtained by higher energy electrons and their reduced ionization damage for ionic solids with smaller effective scattering cross sections are major justifications for the use of this microscope. Also a double tilt hot stage and a Swann-type environmental cell (E-cell) designed for this microscope made it possible to decompose the specimens solely by the heat of the hot stage and to study the in-situ decomposition under a controlled atmosphere. The specifics of the hot stage and E-cell are well described in the literature [109,110]. In-situ lattice parameter measurements of specimen on which gold had been deposited were carried out. Mixed diffraction patterns of gold and the specimen were recorded on glass plates. The use of glass plates eliminates any bending or shrinkage when recorded negatives are under light illumination for a microdensitometer measurement or printing. An accelerating voltage of 500 KV was high enough to use for all the above described experiment.

Siemens 102 and JEM 200 CX microscopes were used mainly to observe the morphology of the product solid MgO in detail. Both microscopes, which are designed for high resolutions with minimized lens aberration, were effective in resolving the shape and size of MgO crystals by the high resolution technique. Since the MgO particles produced from the decompositions were very small, as little as ~2 nm in cross section, a detailed determination of shape and size was possible only with complete correction of lens astigmatism. Efforts were made to get maximum resolution with the optimum defocus condition known as the Scherzer defocus (ΔZ_{Sch}):

$$\Delta Z_{Sch} = 2.5 \left(\frac{C_s \lambda}{2\pi} \right)^{1/2}$$

where ΔZ_{Sch} indicates the distance of underfocus of the objective lens, C_s is the spherical aberration coefficient of the objective lens, and λ is the wavelength of the electron [111]. This condition optimizes the contrast transfer function to make a closest one to one correspondence between real structure and experimental image [112]. Although this condition for maximum resolution is critical, particularly to lattice fringe or lattice imaging, the same principle is applicable to the resolution of fine morphology. These high resolution microscopes were also used to get lattice fringe images of the reaction interface during the decomposition and of the product solid MgO.

4.4. Other Analyses Supporting the TEM Work

4.4.1. X-ray Diffraction (XRD) Measurements

The XRD measurements were carried out in a Siemens X-ray diffractometer using $\text{Cu K}_{\alpha 1}$ radiation of wavelength, 0.15405 nm to check the crystallinity and to accurately measure lattice parameters of the $\text{Mg}(\text{OH})_2$ and MgCO_3 used in this study. Powder samples were packed in a plastic sample holder or stuck to the organic paste which was applied on the plastic plate. The operating conditions were: 20 mA, 40 KV, 2 degrees $2\theta/\text{min.}$, and 1000 counts/sec. Samples were scanned from 10 degrees to 80 degrees of 2θ angle. This scan range includes all the major diffraction peaks of $\text{Mg}(\text{OH})_2$ and MgCO_3 .

4.4.2. Microdensitometer Measurements

For lattice parameter measurements of MgO aggregated of small particles, intensity variations of electron diffraction patterns, recorded on the glass plates were converted to signal lines on a graph paper of a chart recorder by a microdensitometer in which the collimated light beam passing through any medium undergoes intensity variations with changes in the optical densities of the medium. Much easier and less ambiguous measurements can be made with the signal lines from the microdensitometer than with the diffraction patterns on a negative or an enlarged print. Deposited gold and initial reactant solids, whose lattice parameters were accurately determined by XRD measurements, were used as the standard for in-situ calibrations of camera constants to each diffraction pattern.

4.4.3. Optical Diffraction

Optical diffraction was performed on some micrographs of MgO particles produced from the decomposition of $\text{Mg}(\text{OH})_2$ in order to examine the periodic contrast modulations which result from any regularity of the particle shape and size or any regular spatial arrangements of particles and pores [62]. When any periodicity was detected as a sort of intensity distribution on the optical diffractions, the corresponding distances of the periodicity source was calibrated with the optical diffraction of a standard high resolution micrograph having lattice fringes by means of the equation,

$$P_2 = (P_1 R_1 M_1) / (R_2 M_2)$$

where P_1 and P_2 are the spacings of periodic modulations, R_1 and R_2 the measured distances from the screen center to diffracted spots, and M_1 and M_2 the magnifications at which the micrographs of a standard and a material to be analysed were taken, respectively.

4.4.4. Scanning Electron Microscopy (SEM)

Observations by SEM were made on specimens of various degrees of decomposition. Such observations are helpful supplements to the TEM studies since SEM makes it easy to observe larger regions of specimen that cannot be conveniently studied by TEM. All the specimens for SEM observations were stuck on a carbon coated sample holder and their surfaces were coated with a gold layer of ~3 nm thickness to prevent electron charging in the sample. The ISI-130 SEM, which was used for this study, has a maximum resolution of about 3 nm.

4.4.5. BET Surface Area Measurements

Surface areas of some samples were measured by N_2 -adsorption at 78 K in a BET apparatus manufactured by Quantachrome Corp. The theoretical background and techniques of BET surface area measurements are described in the literature [113].

Once the surface area is obtained, an average particle size can be calculated from a reasonable assumption about the shape of the particles by means of the following equation

$$l = (fM)/(Sd)$$

where l is the the size of particle, f is a shape factor which is 6 for a cube or sphere, M the molar weight, S the molar surface area, and d the density of material. Calculated particle sizes for MgO from decomposition of $Mg(OH)_2$ and $MgCO_3$ were compared with those observed by TEM to get an idea of pore size. The particle size calculated from BET surface areas will be much greater than that observed by TEM if closed pores are present or if some pores are too small for nitrogen gas molecules to enter.

5. Results and Discussion

5.1. Structural and Morphological Changes

Sequential pictures of electron diffraction patterns and morphological changes, a) confirmed that the decompositions of $Mg(OH)_2$ and $MgCO_3$ are topotactic reactions which produce pseudomorphic MgO products, b) showed no product other than normal NaCl-type MgO is present during the decompositions, and c) revealed

orientation relationships between the reactant and product solids. In addition to the characteristics of the topotactic reactions possible variants in the orientation relationships were checked with at least two different orientations for each system, and morphological observations of the reaction interfaces were made.

5.1.1. Decomposition of $\text{Mg}(\text{OH})_2$

A pseudomorphic behavior of the decomposition of $\text{Mg}(\text{OH})_2$ was found with the retention of the external shape and size of the initial $\text{Mg}(\text{OH})_2$ crystals as shown in Fig. 23. The resulting apparent porosity of the product solid MgO would be about 54%, which is the theoretical porosity as calculated in Appendix 4.

The diffraction spots of the initial $\text{Mg}(\text{OH})_2$ crystal progressively faded. Simultaneously spots of MgO grew in intensity in positions which showed a definite orientation relationship (Fig. 24) which was identical to that found in other studies [83-85]. From these observations of pseudomorph and spot patterns of MgO , the product solid MgO could be considered as an imperfect single crystal which has a high porosity. The positions of $\text{Mg}(\text{OH})_2$ spots never changed as the decomposition progressed. This observation, which was exactly reproducible with several repeated experiments, is consistent with the findings of Gordon and Kingery [84] but not with those of Goodman [83] or Anderson and Horlock [29]. These last two sets of investigations reported that before the decomposition starts with the appearance of MgO spots the position of $(11\bar{2}0)$ $\text{Mg}(\text{OH})_2$ spot moves

out to that of $(20\bar{2})$ MgO spots in the $[0001]$ orientation of $\text{Mg}(\text{OH})_2$. Although the observation of the preserved $\text{Mg}(\text{OH})_2$ spots was consistent with the findings of Gordon and Kingery, their reported 2-3% greater MgO lattice spacing at the early stage of decomposition was not observed in this study. Possibly, they mistook the double diffraction spot resulting from the $(11\bar{2}0)$ $\text{Mg}(\text{OH})_2$ spot ($d=0.1573$ nm) and the $(20\bar{2})$ MgO spot ($d=0.1489$ nm) for the $(40\bar{4})$ MgO spot. This double diffracted spot from $(11\bar{2}0)$ - $(20\bar{2})$ spots appears as overlapped between the $(22\bar{4}0)$ $\text{Mg}(\text{OH})_2$ spot and the $(40\bar{4})$ MgO spot (cf. Fig. 24). Furthermore, it has a greater intensity at the initial stage of the decomposition than the $(40\bar{4})$ MgO spot. The double diffracted spot, interpreted as the $(40\bar{4})$ MgO spot, would give a fictitious lattice spacing for MgO which is 2.8% greater than normal MgO lattice.

In order to observe the first order spot in the absence of a double diffraction spot, an increased diffraction lens current was used to obtain an enlarged diffraction pattern (Fig. 25) in which the $(20\bar{2})$ MgO spot was clearly separated from the $(11\bar{2}0)$ $\text{Mg}(\text{OH})_2$ spot and the position of the MgO spot corresponded approximately to that for normal MgO. The lattice parameter of the small MgO particles will be discussed further in the next section.

The observed orientation relationship shown in Fig. 24 was used to make a stereographic projection of planes of $\text{Mg}(\text{OH})_2$ and MgO (Fig. 26). In this stereographic projection, 60 degree rotation around the projection pole gives an exact superposition for $\text{Mg}(\text{OH})_2$ family

planes but not for MgO family planes, although only the planes parallel to the [111] direction of MgO have the superposition. Therefore, there is an ambiguity. Either the MgO spots in the [111] orientation arose from the MgO particles having the single orientation shown in the projection or from having two orientations which are rotated 60 degrees to each other around the [111] orientation of MgO (cf. Fig. 27). The first interpretation is shown correct by observations of diffraction patterns with orientations in which the mirror plane of $\text{Mg}(\text{OH})_2$ is not parallel to the mirror plane of MgO. If the MgO particles had two variants in the orientation relationship, the spots of the same family planes of MgO will have a mirror image to the mirror plane of $\text{Mg}(\text{OH})_2$. Figure 28 shows only a single orientation since the MgO spots do not have the mirror image to the $(1\bar{1}00)$ mirror plane of $\text{Mg}(\text{OH})_2$.

This result is contrary to Garrido's observation [82] of two different orientations expected from the orientation variants described above. The origin of the discrepancy is uncertain; it might result from the different histories of the decompositions.

From the diffraction measurements of the $[11\bar{2}0]$ and $[1\bar{1}02]$ $\text{Mg}(\text{OH})_2$ orientations (Figs. 28 & 29, respectively), the lattice parameter of the c-axis is found to be unchanged as the decomposition proceeded. This result disproves the Goodman hypothesis that at the early stage of the decomposition the lattice shrinks along the c-axis because of chemical condensation of water in each unit cell of

Mg(OH)_2 , and thus, together with the fixed positions of Mg(OH)_2 spots in the [0001] orientation, rules out the suggested homogeneous mechanism.

The diffraction patterns in all the orientations investigated in this study showed no additional spots which could be assigned to any possible intermediate phases.

The sequential bright field (BF) images corresponding to the diffraction patterns of Fig. 24 are shown in Fig. 30. The BF image of the initial Mg(OH)_2 has a mottled contrast which slowly disappeared as the MgO diffraction spot became more intense. This type of contrast was always visible even with micrographs taken as soon as the specimen was inserted in the microscopes. Much effort was given to identify the origin of this mottled contrast, which might result from the Mg(OH)_2 structure, the initial decomposition, or both of them.

First, Mg(OH)_2 specimens from other sources were checked since other investigators, except for Goodman, did not mention the initial contrast; his Mg(OH)_2 was from the same locality as that used in this study. Figure 31 shows three BF images of Mg(OH)_2 from different sources. Their contrasts are more or less the same.

Second, a specimen was observed at liquid nitrogen temperature to exclude any possible decomposition in the high vacuum of the microscope at room temperature. Figure 32 still shows a similar contrast with some aggravation due to the adsorption of residual gases in the microscope.

Third, in-situ BF images were taken before and after water vapor was admitted to the microscope as the 80 torr mixture of He-H₂O gas. During the flow of water vapor, the electron beam was turned off to prevent beam heating. If the contrast were a consequence of any decomposition, it should diminish with the flow of water since the saturated H₂O pressure of the mixed He-H₂O gas is about 4 orders of magnitude greater than the equilibrium H₂O pressure of Mg(OH)₂ decomposition at room temperature. Figure 33 shows no noticeable change in the contrast before and after a two-hour flow of the gas.

By examination, the results of above three experiments suggest that the initial contrast is due to structural defects which are inherent from the bonding and structural character of Mg(OH)₂. Contrast analysis was applied in an effort to identify the type of defects. Decomposition of Mg(OH)₂ occurs so quickly in an electron beam that a perfect analysis was impossible, although some instructive data were obtained. As shown in Fig. 34, the contrast was stronger with excitation of the (11 $\bar{2}$ 0) spot, nearly vanished with excitation of the (10 $\bar{1}$ 0) spot, and invisible in the [11 $\bar{2}$ 0] orientation.

The stronger contrast with the (11 $\bar{2}$ 0) spot may imply that the direction of a displacement vector, R responsible for the contrast lies closer to the $\langle 11\bar{2}0 \rangle$ direction than to other principal directions, i.e., the value of $g \cdot R$ may be greatest with $g = \langle 11\bar{2}0 \rangle$. This result is consistent with the $\langle 11\bar{2}0 \rangle$ type edge dislocation model which Brindley and Ogilvie [94] suggested to interpret the texture of Mg(OH)₂ observed by X-ray single crystal experiments.

Furthermore, the streak-like extra spots shown in Fig. 35 and the streaks shown in Fig. 28A might result from the suggested texture, which could be described as small perfect $\text{Mg}(\text{OH})_2$ crystallites connected with the $\langle 11\bar{2}0 \rangle$ type edge dislocations to make an imperfect crystal of $\text{Mg}(\text{OH})_2$ having a range of orientations of the c-axis but with no rotation of the a-axes around the c-axis. The streaks surely arose from the $\text{Mg}(\text{OH})_2$ crystals since the diffraction patterns from three experiments for the recognition of the initial contrasts always showed them. But their origin could not be clearly identified. They may not reflect a structural feature of the $\text{Mg}(\text{OH})_2$ that affected the overall path of the decomposition [83].

In disagreement with Anderson and Horlock's suggestion that decomposition is initiated and advances only at the surfaces normal to the basal plane of $\text{Mg}(\text{OH})_2$, the kinetic study described in an earlier section of this thesis implied that decomposition starts over the entire surface, though with different basal and edge rates. If so, with the $[0001]$ $\text{Mg}(\text{OH})_2$ orientation Moiré fringes should be visible in which atomic distances are mismatched by about 5% in the semi-coherent planes of (0001) $\text{Mg}(\text{OH})_2$ and (111) MgO . Indeed, the Moiré fringes were observed in small scale as shown in Fig. 36 at an early stage of decomposition. They were not visible at the later stage of decomposition, probably because of the superimposed contrasts of the weak Moiré fringes and MgO fine particles.

A fine probe electron beam changed the contrast of only the areas intercepted by the beam. Simultaneously MgO diffraction spots

appeared (Fig. 37). The bright area of partially decomposed Mg(OH)_2 was bounded by the dark area of undecomposed Mg(OH)_2 . This observation disproves the hypothesis that the reaction occurs only at the edge area of crystal because decomposition was completed in the area of beam heating without any decomposition at the crystal edges. The hot stage TEM experiments and the SEM observations, which will be discussed later, also proved that decomposition starts on the entire Mg(OH)_2 surface and advances toward the inside of the crystals with a kind of cracking.

5.1.2. Decomposition of MgCO_3

Figure 38 shows that initial MgCO_3 shape and size are unchanged by decomposition. The porosity of the resulting MgO is about 60% (Appendix 4).

Electron beam heating decomposed MgCO_3 crystals at slower rates than it does Mg(OH)_2 crystals. A quantitative analysis of the heating is nearly impossible [108], but it is known that an electron beam can heat such insulating materials to as high as 800 K. The diffraction spots of MgCO_3 crystals in the [0001] orientation changed preferentially to those of the [111] orientation of MgO (Fig. 39). This orientation relationship implies that MgO crystallites are strongly oriented despite the high porosity. In the [0001] orientation of MgCO_3 , the $\{10\bar{1}0\}$ and $\{20\bar{2}0\}$ spots are missing, as shown in Fig. 39, due to a zero value of the structure factor. The orientation relationship of MgCO_3 decomposition is similar to that

of $\text{Mg}(\text{OH})_2$ decomposition. But they are rotated 30 degrees to each other around the three fold axes in comparison to the parallel planes as understood from the stereographic projections with the observed orientation relationships (Figs. 26 & 40).

Since there is an ambiguity of variant in the orientation relationship with the parallel three fold axes as discussed for the $\text{Mg}(\text{OH})_2$ decomposition, MgCO_3 was decomposed in the other orientations in order to check for such a variant. Decomposition at the $[10\bar{1}1]$ orientation of MgCO_3 showed, for the first time, that there is a variant (Fig. 41). The (200) MgO spots are not at 90 degree but are rotated about 55 degrees to each other. This means MgO spots arise from two different orientations which are proved with dark field micrographs (Fig. 52). Although the dark field micrographs were not taken at the typical two-beam condition, they can still serve to identify the distribution of MgO particles which have two different orientations. Therefore, MgO crystallites produced from MgCO_3 decomposition must have two variants in orientation relationship, which are rotated 60 degrees to each other around the three fold axis. The orientation relationship observed in this study differs by a 30 degree rotation around the three fold axis from Dasgupta's and is inconsistent with the relationships of Sing Dev and Floquet and Niepce. The major orientation relationship found by Oh et al. agrees with the orientation relationship from this study. Of the three minor orientation relationships by Oh et al., only two were found in this

study from the diffraction pattern of an $[111]$ orientation (Fig. 42), i.e., the minor orientation relationship (2); $(0001) \text{MgCO}_3 // \bar{(112)} \text{MgO}$, $[\bar{1}\bar{2}10] \text{MgCO}_3 // [111] \text{MgO}$ and the minor orientation relationship (3); $(0001) \text{MgCO}_3 // (110) \text{MgO}$, $[\bar{1}\bar{2}10] \text{MgCO}_3 // [001] \text{MgO}$. However, the observed minor orientation relationships had three variants with six (111) and (200) spots placed at the corners of regular hexagon. Such an arrangement of (111) and (200) spots in the $[\bar{1}\bar{1}\bar{2}]$ and $[110]$ orientations, respectively, could result from three equivalent orientations rotated 120 degrees to each other around the three fold axis of MgCO_3 . The origin of the minor orientation relationships with three variants and the major one with two variants will be discussed in the next section. The reason for the other inconsistencies between orientation relationships from this study and previous studies is not certain. One reason may be that diffraction spots from several crystallographically equivalent orientation variants have been interpreted as non-equivalent orientation variants.

Since no diffraction spots other than those from MgCO_3 and MgO crystals were found in this study, the possibility of any detectable intermediate phases is excluded. The morphological observations (Fig. 43) of MgCO_3 decomposition showed the decomposed regions to be sharply bounded. Dark contrast, which might be related to a strain field or to a change in orientation, appeared at the reaction interfaces. The source of the contrast could not be resolved and identified because of decomposition under the electron beam. In the

bright field image of partly decomposed MgCO_3 (Fig. 44), the interface moved so quickly as the decomposition proceeded that high resolution observations of the interface could not be obtained. The MgO , which was produced by electron beam heating, had an average particle size of about 3 nm. A cracking occurred abruptly at the later stages of the decomposition (Fig. 45). The average particle size and the cracking will be discussed later.

5.1.3. Origin of the Orientation Variants

The electron diffraction work discussed in the previous sections showed several variants of the orientation relationships between the parent solids and the MgO . Decomposition of MgCO_3 has two variants of the major and three variants of the minor orientation relationships while decomposition of Mg(OH)_2 produces only one variant. These orientation relationships can only be established for the highly porous product solids by preserving during decomposition a sort of structural unit such as an invariant (or coherent) plane or a line which has the coincident lattice sites [78]. Preserved lines or planes provide a minimum energy path for a solid-solid phase transformation [77]. In the decomposition of Mg(OH)_2 , the (0001) plane of Mg(OH)_2 can from an atomistic point of view be a semi-coherent plane with the (111) plane of MgO . However, the small size of the cubic MgO particles (~2 nm) (Figs. 48 & 49) considered in terms of a schematic packing of such particles in space (Fig. 50) exclude the possibility of a long range semi-coherent plane. The

reaction interfaces could not be flat to provide the observed morphology. Furthermore, if the (0001) plane of $\text{Mg}(\text{OH})_2$ is the semi-coherent plane, the evolution of H_2O gas molecules would be extremely difficult across the plane, contrary to the results found in the kinetic study.

The only possibility for the observed orientation relationships, except the minor ones from the MgCO_3 decomposition, would be for the oxygen octahedra in the parent solid to be preserved in the MgO . The $\text{Mg}(\text{OH})_2$ and MgCO_3 have one and two types of oxygen octahedra in terms of their orientations, respectively. Figures 46 & 47 show that the orientations of these oxygen octahedra match well with the major orientation relationships of the decompositions, under the assumption that the MgO particles start to grow from the oxygen octahedra in the parent solids. The directions of oxygen-oxygen bonds in the projected parallel planes are perfectly preserved for the decomposition of $\text{Mg}(\text{OH})_2$. For the decomposition of MgCO_3 those in the one triangular face of oxygen octahedra and those in the next triangular face parallel to the first are rotated 7 degrees in opposite directions (see Fig. 47) around the projection axis. This angular mismatch and the change of the irregular octahedron of MgCO_3 to the regular one of MgO might contribute to the arc of MgO diffraction spots, which spans about 14 degrees. The interatomic distances and angles of the oxygen octahedra in the parent solid and MgO structures are close enough to support the hypothesis that the octahedra of the parent solids are the starting building blocks or the nuclei for the

decompositions. These nuclei could grow to a certain optimum size by a cooperative movement of ions from the surrounding disrupted lattice due to loss of the gaseous product.

The minor orientation relationships from the decomposition of MgCO_3 could not be rationalized with any invariant planes either. But probably the main relations reflect preservation of a line of interatomic bonds in the (0001) plane of MgCO_3 . For the minor orientation relationship (3), the O-O bond, which is 0.285 nm in MgCO_3 would become the O-O bond of 0.2979 nm in MgO. This O-O bond direction is consistent with the orientation relationship so that the O-O bonds in the (0001) plane of MgCO_3 may be the starting structural units for the growth of MgO within the observed orientation relationship. By the same analogy, the minor orientation relationship (2) could be understood to be derived from a change of the Mg-Mg bond of 0.46332 nm in MgCO_3 to the Mg-O-Mg bond of 0.4213 nm in MgO by preservation of the Mg-Mg bond directions and movement of oxygen ions to the middle of the original Mg-Mg bonds by travelling about 0.142 nm from the sites of the oxygen ions in the next layers. Growth of MgO with random preservation of O-O or Mg-Mg bonds in the (0001) plane of MgCO_3 may produce the observed minor orientation relationships since the bonds have threefold symmetry about the [0001] axis.

5.2. Lattice Parameter of the Product Solid MgO

For the lattice parameter measurements the diffraction patterns were recorded after cooling to room temperature. Consequently, the measured lattice parameters can be compared directly with those reported in the literature [70].

The calibration of the experimental method with the gold film and the initial reactant solids proved that the method utilizing the high accelerating voltage of 500 KV and microdensitometer provides lattice parameters correct within about 0.05% error range (Fig. 25). For the calibration and other measurements, only the diffraction spots and rings measured along straight lines were compared to minimize any possible error due to distortion effects from non-uniform magnetic or electric fields in space. Such non-uniform fields distort the rings into ellipses [76].

The measured lattice parameters of gold, Mg(OH)_2 , and MgCO_3 were consistent with those reported in the JCPDS file (Appendix 1) within an error range of 0.05%. The measured lattice parameters of MgO produced from Mg(OH)_2 (hereafter referred to as h-MgO) by decomposition at 600 K were $0.6 \pm 0.2\%$ greater than those reported for normal MgO. Neither the diffraction spots of MgO nor of Mg(OH)_2 or MgCO_3 changed their positions throughout the decompositions. The lattice parameter of h-MgO from a partially decomposed Mg(OH)_2 was also greater by $0.6 \pm 0.2\%$. But annealing of h-MgO at 875 K for an hour gave a lattice parameter which was within $\pm 0.1\%$ of that for large crystals of MgO without an increase in the particle size of h-MgO.

The lattice parameter of MgO produced from the decomposition of MgCO_3 (hereafter referred to as c-MgO) was also within $\pm 0.1\%$ of that for large crystals of MgO. As previously reported [91], the greater lattice parameter observed prior to annealing could result from water vapor adsorption on the surface of the tiny h-MgO particles, since h-MgO annealed at 875 K and c-MgO had the same lattice parameter as normal MgO. The lattice parameter of c-MgO hydrated in air for a week was about 0.8% greater than normal. This hydrated specimen, after heating to 600 K, had lattice constants about 0.7% greater than normal MgO. It is known that this treatment does not remove all the water, which is strongly chemisorbed as surface $(\text{OH})^-$ ions. These results are consistent with those of the kinetic studies. The persistent adsorption of water molecules on the surface of MgO particles up to 800 K is almost certainly responsible for the expanded lattice.

The observed average particle sizes of h-MgO and c-MgO (Figs. 48 & 51) are 2 and 3 nm, respectively. The MgO particles are cubic. Since the measured lattice parameters of such small particles without the adsorption of water were within $\pm 0.1\%$ of those for normal MgO, the lattice parameter is probably independent of particle size as long as the particle shape is cubic and at least 2 nm on an edge. This unchanged lattice parameter is inconsistent with the previous studies which reported a lattice contraction [86,91].

There is no clear theoretical prediction of what condition, if any, should be expected for small particles. For particles with curved

surfaces, the lattice parameter change for small particles is given by the Laplace equation as follows

$$\frac{da}{a} = \frac{\beta\gamma}{3} \left(\frac{1}{r_1} + \frac{1}{r_2} \right)$$

where r_1 and r_2 are the principal radii of a curved surface, β the compressibility, and γ the surface tension [88]. According to the above equation, a flat surface does not have any pressure difference across the surface. The surface of MgO particles should be stretched or contracted in order to form a curved surface, and then the surface tension would be applied in the curved surface. Marks [114] reported inhomogeneous strains in small particles with the observation of strain contrast (intensity variations along an extinction contour) by dark field microscopy. But it is still obscure how the energy balance around the corners, edges, and surfaces of cubic particles contribute to the lattice parameter measured by diffraction technique, which is in reality an averaged value.

5.3. Particle Size and Shape of the Product Solid MgO

5.3.1. Direct Observation

The particle size and shape of h-MgO was hardly visible with the Philips 301 because the maximum magnification was only 220000. The JEM 200 CX and the Siemens 102 high resolution microscopes revealed the size and shape of the MgO particles in detail when a complete

correction of the objective lens astigmatism had been made and fine focussing had been achieved.

Figure 48 shows the h-MgO particles produced by electron beam heating in the [100] orientation. As shown in the figure, the contrast exhibits sharp edges and perpendicular corners, which implies that the MgO particles have a shape in which the (100) surfaces perpendicularly meet at their edges, i.e., a cubic, tetragonal, or orthorhombic shape. A tetragonal or orthorhombic shape is not likely since every (100) surface of MgO has exactly the same surroundings as in the parent solid structure of $\text{Mg}(\text{OH})_2$ (cf. Fig. 26). The cubic shape of h-MgO particles is proved by optical diffraction in the next section. The contrast of h-MgO particles (Fig. 48) is best fit by a 2 nm particle edge length.

The electron beam causes more or less ionization damage to many ionic solids [108], so there is danger that the electron beam causes enough damage to the $\text{Mg}(\text{OH})_2$ to make it decompose to MgO by a mechanism different from the thermal decomposition mechanism. To see if any difference is caused in the morphological evolution by the electron beam, a single crystal of $\text{Mg}(\text{OH})_2$ was decomposed in vacuum at 600 K, and a thin specimen of the h-MgO was prepared by the cleavage method described above. Figure 49 shows the morphology of the h-MgO from the thermal decomposition, which is similar to that from the electron beam heating. The electron diffraction measurements did not show any differences in the

decomposition by the two methods, either. Thus electron-specimen interaction does not play a significant role.

The c-MgO particles were shown to be the cubes of ~3 nm average size (Fig. 51). But in contrast to h-MgO, some of the c-MgO particles have different edge directions. These may consistently reflect the orientation variants discussed above. This conjecture is supported by the dark field micrographs (Fig. 52) which show a relatively uniform distribution of MgO particles from two variants in the major orientation relationship.

5.3.2. Optical Diffractions

The optical diffraction pattern in Fig. 53 shows the streaked satellite spots in which the direction agrees well with those of the electron diffraction pattern (Figs. 48 & 49). These streaks are the expected ones from the interference functions for small cubic particles in electron diffraction and from the contrast of square and rectangular arrangements in the optical diffraction [62,63].

The image of the [111] orientation of h-MgO showed uniformly rounded contrasts (Fig. 54), but its magnification was too high to get an optical diffraction pattern of reasonable size. The optical diffraction patterns of the low magnification micrographs of the [100], [110], and [111] orientations of h-MgO showed the shapes in the intensity distributions of the diffracted beams to be a square, an oval, and a circle, respectively as shown in Fig. 55. This result proves that the h-MgO particles have cubic shapes and that they are

regularly stacked in space with the same orientation as shown schematically in Fig. 50.

The optical diffraction patterns of c-MgO particles show shapes similar to those of h-MgO particles. The [111] orientation of c-MgO shows the isotropic circular intensity distribution (Fig. 56B), and Fig. 56A shows a distorted distribution probably due to the two major orientations of the particles. The average particle sizes calculated from the optical diffraction patterns do not conform well to the sizes directly observed. Probably the discrepancy is a consequence of the overlapped contrasts of many particles.

5.3.3. Comparison of the Surface Areas by BET and TEM Methods

The surface areas of h-MgO measured by the BET method differ widely in the literature [17-20,115]. But most surface areas of h-MgO from single or well defined crystals of $\text{Mg}(\text{OH})_2$ have been reported to be 50 to 200 m^2/g . These values are consistent with those measured in this study. But surface area calculated from the particle size, ~2 nm observed by TEM is ~800 m^2/g . This difference in calculated and measured surface areas implies that a part of the surface area of h-MgO is not accessible to N_2 gas molecules. The discrepancy has been ascribed in a recent study of the H_2O catalyzed sintering of MgO to a high relative volume of closed pores [116]. The surface areas of c-MgO measured by the BET and TEM measurements are consistent to $500 \pm 100 \text{ m}^2/\text{g}$. This result implies that perhaps; because of the orientation variants, all pores of the c-MgO are

accessible to N_2 . Sintering studies are planned with c-MgO which will test the conclusion that its pores are all open while a large fraction of those in h-MgO are closed.

5.4. Cracking Phenomena of Decomposition Reactions

During the decomposition of $Mg(OH)_2$ and $MgCO_3$, cracking was observed as shown in Figs. 57-61.

Cracking occurred for only partially decomposed $Mg(OH)_2$. This fact was apparent because the diffraction patterns show the $Mg(OH)_2$ and MgO diffraction spots together (Fig. 57). Gordon and Kingery [84] and other previous investigators [29,117] proposed that the cracking occurred to relieve strain that accumulated at the semi-coherent reaction interfaces. But as described above, the present diffraction study did not find any significant accumulated strain. And if accumulated strain were responsible for the cracking, it must somehow be continuous between the cracks. But the cross sectional distances between cracks are 1 to 3 μm , distances about 1000 times greater than the h-MgO particle size of 2 nm so that the strain cannot be continuous between the cracks.

The cracking in the decomposition of $MgCO_3$ occurred after the decomposition was nearly complete (Figs. 45 59). This observation suggests that the cracking does not occur because of accumulated strain but because of some other driving force.

The only identifiable driving force for the cracking is the high surface energy arising from the small particles. Figure 62

schematically suggests the cracking mechanism: The small particles aggregate at a certain scale to reduce the high surface energy, at the same time a stress will develop along the reaction interface. This stress acts on both the product and reactant layers. Because of the weak bonding normal to the basal planes of $\text{Mg}(\text{OH})_2$, cracks can propagate into it. Cracks did not propagate through MgCO_3 , probably because of its stronger bonds. The Mohs hardness of MgCO_3 and $\text{Mg}(\text{OH})_2$ are 3.5-4.5 and 2.5, respectively [118].

Cracking occurred so abruptly that continuous recording could not be made by TEM. Such an abrupt change is characteristic of exothermic reactions [55]. The resultant exothermic heat may be related to the reported exothermic peaks of DTA studies of decomposition reactions [26] and to the origin of the explosive ejection of powder samples during seemingly steady state decomposition [25].

IV. GENERAL DISCUSSION

The TEM studies do not reveal any structurally metastable phases which could be responsible for the observed anomalously low equilibrium H_2O pressures during $Mg(OH)_2$ decomposition. Instead very small cubic MgO particles of the normal NaCl-type structure were found to form from $Mg(OH)_2$ or $MgCO_3$ of normal lattice constants. An equilibrium between $Mg(OH)_2$, product MgO , and the water adsorbed as $(OH)^-$ ions on the MgO appears to be attained in the $Mg(OH)_2$ open cell and effusion studies.

Comparison of Reis' and Beruto et al's calorimetric measurements on MgO with adsorbed water and MgO with the water removed implies that the adsorption of water reduces the excess energy content of the high surface area MgO from ~ 73 kJ/mole to near zero. Thus the chemisorbed water is held more tightly than water in the reactant solid $Mg(OH)_2$.

An adsorption equilibrium is therefore to be expected when H_2O pressures are below the equilibrium decomposition pressure. An adsorption reaction has a different equilibrium pressure as the fraction of surface covered by adsorbed species changes with accompanying change of configurational entropy. Similar apparent enthalpy changes but different apparent entropy changes of the metastable equilibrium behavior from Kay and Gregory's Knudsen cell and open cell of this study are consistent with the conclusion that the escape fluxes reflect adsorption equilibrium with different

fractions of surface coverage. However, a careful adsorption study would be necessary to identify the relationship between the equilibrium pressure and the fraction of surface adsorbed by water under similar experimental conditions to those of this study so that the above suggested mechanism of adsorption equilibrium can be proved.

Decomposition of MgCO_3 is essentially irreversible in open cells and does not as readily approach metastable equilibrium in Knudsen cells as does Mg(OH)_2 decomposition. From Beruto et al.'s apparent enthalpy of adsorption equilibrium, it is known that the CO_2 adsorbed on the surface of MgO is also more tightly held than that in the parent reactant, MgCO_3 . This fact and the close value of apparent activation entropy to the entropy of MgCO_3 decomposition may imply that the decomposition of MgCO_3 single crystals at the temperatures lower than ~ 825 K is governed by desorption of CO_2 . But at the temperatures higher than ~ 825 K, the reaction must be determined by an early irreversible step as discussed above.

From the observations of orientation relationships and particle size and shape of the product solid MgO , it is proposed that the structural transformations of both Mg(OH)_2 and MgCO_3 start from coherent nuclei of oxygen octahedra in the reactant solids which grow to an optimum size perhaps by a cooperative movement of ions and production of a mobile adsorbed state of the product gases. From equilibrium studies, it is known that the H_2O and CO_2 are bound on the surface of MgO more strongly than in Mg(OH)_2 or MgCO_3 ,

respectively. The fact that sintering of MgO is catalyzed by H₂O [116] and CO₂ [58] suggests these gases can catalyze the movement required for formation of the initial 2 nm or 3 nm MgO particles.

These small MgO particles aggregate perhaps to reduce the very high energy from the large specific surface area. After this aggregation the initial MgO particle size and shape seem to be preserved, but with a bimodal pore size distribution, i.e., cracks of ~10 to 50 nm cross section at 1 to 3 μm intervals and ~1 to 3 nm pores between the small particles.

Rao et al., on the basis of observations of X-ray diffraction line sharpening, attributed the DTA exothermic peaks found in the decomposition reactions of some hydroxides and carbonates to the annihilation of defects of product solids. But no evidence of significant defects was found in the MgO formed from either Mg(OH)₂ or MgCO₃ decomposition. The exothermic peaks observed when these solids are decomposed may be due to the aggregation of small particles which generate heat. X-ray line sharpening would result if the particles aggregate in such a way as to give more coherent scattering of X-rays.

V. SUMMARY AND CONCLUSIONS

Kinetic and TEM studies showed that the decomposition of $\text{Mg}(\text{OH})_2$ and MgCO_3 starts on all the surfaces of the reactant solids where coherent nuclei grow to form cubic MgO particles, and continues autocatalytically with definite orientation relationships by a movement of ions from the lattice disrupted due to the removal of gas molecules at the reaction interfaces.

No intermediate phase or metastable MgO, which could be responsible for the anomalous equilibrium behavior from the decomposition of $\text{Mg}(\text{OH})_2$ observed by Kay and Gregory, was found. Both $\text{Mg}(\text{OH})_2$ and MgCO_3 decompose topotactically to yield porous aggregates of MgO with the external shape and size of the reactant crystals. Thus the product solid MgO has from the two reactions about 54% and 60% porosities, respectively.

While the decomposition of $\text{Mg}(\text{OH})_2$ yields MgO with a single orientation relationship; $(0001) \text{Mg}(\text{OH})_2 // (111) \text{MgO}$, $[11\bar{2}0] \text{Mg}(\text{OH})_2 // [10\bar{1}] \text{MgO}$, that of MgCO_3 has two variants in a major orientation relationship; $(0001) \text{MgCO}_3 // (111) \text{MgO}$, $[11\bar{2}0] \text{MgCO}_3 // [2\bar{1}\bar{1}] \text{MgO}$; and three variants in two minor orientation relationships. These major orientation relationships and the fact that cubic MgO particles of 2 to 3 nm are formed suggest that the oxygen octahedra in the reactant solids are the coherent nuclei for the construction of such observed MgO particles.

The small cubic MgO particles which have high excess surface energy and are in contact may aggregate spontaneously to reduce the excess energy and make the ~10 to 50 nm cracks which are formed at 1 to 3 μm intervals during decomposition of $\text{Mg}(\text{OH})_2$ crystals. These cracks provide low impedance routes for gas phase diffusion through the porous MgO scale. Similar cracks are not formed in decomposing MgCO_3 crystals although the aggregation occurred to form the porous product solid MgO. The aggregation might be responsible for the exothermic heat reported from the decomposition of some carbonates and the explosive ejection of powder reported from partially decomposed powder samples.

Considering the strong adsorption of water on the surface of MgO particles and the results of TEM studies, the anomalous equilibrium of $\text{Mg}(\text{OH})_2$ decomposition seems to be due to an adsorption equilibrium which is maintained with different steady state pressures that are established during the decomposition in Knudsen cells and in open cells.

Decomposition of MgCO_3 single crystal is an irreversible process, with the rate limiting step changing at 825 K. Knudsen cell studies of MgCO_3 powder decomposition suggest a transition from an irreversible to a reversible rate limiting step as the decomposition temperature was increased and as the area of orifice was decreased with the apparent enthalpy changes from a high value to the standard one.

ACKNOWLEDGMENTS

I express my sincere gratitude to Professor Alan W. Searcy for his guidance and encouragement which he provided with kindness and patience throughout the course of this investigation. I also thank him for correcting my English and helping me to revise this manuscript.

I also wish to express my gratitude to Professors Ronald Gronsky and David H. Templeton for reviewing this manuscript.

I would like to thank Dr. Dario Beruto for many helpful discussions and invaluable information concerning the kinetic studies of this dissertation, and to thank Dr. Ulrich Dahmen for many delightful discussions and instruction in crystallography and solid state phase transformations related to the TEM studies of this dissertation.

My thanks to Dr. David J. Meschi who kindly helped me to understand some problems of gas-solid reaction kinetics and thermodynamics.

I extend my appreciation to the LBL staff, especially David W. Ackland and Donald J. Jurica for their technical assistance with TEM experiments, and Valerie Kelly for her efficient word processing and typing of this manuscript.

I am and will remain indebted to my wife Young Sook and my parents for their endless understanding and support.

Special thanks to the Korean Government for supporting me with its scholarship for four years while I have been studying here at Berkeley.

This work was supported by the Director, Office of Energy Research, Office of Basic Energy Sciences, Materials Sciences Division of the U.S. Department of Energy under Contract No. DE-AC03-76SF00098.

REFERENCES

1. D.A. Young, "Endothermic Decompositions," Ch. 3, in Decomposition of Solids, Pergamon Press, 1966.
2. H. Schmalzreid, Solid State Reactions, Academic press, 1974.
3. C.H. Bamford and C.F.H. Tipper (eds.), "Reactions in the Solid State," Vol. 22, in Comprehensive Chemical Kinetics, Elsevier, 1980.
4. W.D. Kingery, H.K. Bowen, and D.R. Uhlman, Introduction to Ceramics, 2nd ed., John Wiley and Sons, 1976.
5. D.W. Richerson, Modern Ceramic Engineering, Marcel Dekker, 1982.
6. L.L. Hench and D.R. Ulrich (eds.), Ultrasture Processing of Ceramics, Glasses, and Composites, John Wiley and Sons, 1984.
7. O. Bowles, "The Lime Industry," U.S. Bur. Mines Info. Circ., 7651 (1952).
8. W.E. Garner, "Kinetics of Endothermic Solid Reactions," Ch. 8, in Chemistry of the Solid State, W.E. Garner (ed.), Academic Press, 1955.
9. A.W. Searcy and D. Beruto, J. Phys. Chem., 80, 425 (1976).
10. A.W. Searcy and D. Beruto, J. Phys. Chem., 82, 163 (1978).
11. J. Green, J. Mat. Sci., 18, 637 (1983).
12. V.A. Philips, H. Opperhauser, and J.L. Koble, J. Am. Cer. Soc., 61, 75 (1978).
13. W.F. Giauque and R.C. Archibald, J. Am. Chem. Soc., 59, 561 (1937).

14. E. Kay and N.W. Gregory, J. Phys. Chem., 62, 1079 (1958).
15. N.W. Gregory and R.H. Mohr, J. Am. Chem. Soc., 77, 2142 (1955).
16. G.F. Knutsen, A.W. Searcy, and D. Beruto, J. Am. Cer. Soc., 65, 219 (1982).
17. T.A. Reis, Ph.D. Thesis, University of California, Berkeley, 1983.
18. D. Beruto, P.F. Rossi, and A.W. Searcy, J. Phys. Chem., 89, 1695 (1985).
19. R.I. Razouk and R.Sh. Mikhail, J. Phys. Chem., 59, 636 (1955).
20. D.T. Livey, B.M. Wanklyn, M. Hewitt, and P. Murray, Trans. Brit. Cer. Soc., 56, 217 (1957).
21. P.J. Anderson and P.L. Morgan, Trans. Faraday Soc., 60, 930 (1964).
22. P.J. Anderson, R.F. Horlock, and J.F. Oliver, Trans. Faraday Soc., 61, 2754 (1965).
23. R.K. Webster, T.L. Jones, and P.J. Anderson, Proc. Brit. Cer. Soc., 5, 153 (1965).
24. M.G. Kim, M.S. Thesis, University of California, Berkeley, 1982.
25. A.W. Searcy, M.G. Kim, and D. Beruto, "The Kinetics of Decomposition in Powder Beds: Theory and Experiment," in High Temperature Materials Chemistry - II, Z. A. Munir and D. Cubicciotti (eds.), The Electrochemical Soc., 1983.
26. C.N.R. Rao, S.R. Yoganarasimhan, and M.P. Lewis, Can. J. Chem., 38, 2359 (1960).
27. B.S. Girgis, Trans. and J. Brit. Cer. Soc., 71, 177 (1972).
28. S.J. Gregg and R.I. Razouk, J. Chem. Soc., 61, S36 (1949).

29. P.J. Anderson and R.F. Horlock, *Trans. Faraday Soc.*, 58, 1993 (1962).
30. R.C. Turner, I. Hoffman, and D. Chen, *Can. J. Chem.*, 41, 243 (1963).
31. R.S. Gordon and W.D. Kingery, *J. Am. Cer. Soc.*, 50, 8 (1967).
32. J.H. Sharp, *Trans. Brit. Cer. Soc.*, 72, 21 (1973).
33. H.T.S. Britton, S.J. Gregg, and G.W. Winsor, *Trans. Faraday Soc.*, 48, 63 (1952).
34. M. Li, Ph.D. Thesis, The Pennsylvania State Univ., 1984.
35. JANAF Tables, (U.S. Government Printing Office, Washington, D.C.).
36. K.H. Stern and E.L. Wise, "High Temperature Properties and Decomposition of Inorganic Salts. Part 2, Carbonates," NSRDS-NBS 30, 1969.
37. Y. A. Chang and N. Ahmad, Thermodynamic Data on Metal Carbonates and Related Oxides, The Metal. Soc. of AIME, 1982.
38. K. Denbigh, The Principles of Chemical Equilibrium, 4th ed., Cambridge University Press, 1981.
39. K.J. Laidler, Chemical Kinetics, 2nd ed., McGraw-Hill, 1965.
40. M. Boudart and G. Djéga-Mariadassou, Kinetics of Heterogeneous Catalytic Reactions, Princeton University Press, 1984.
41. I. Langmuir, *Phys. Rev.*, 8, 149 (1916).
42. M. Knudsen, The Kinetic Theory of Gases, John Wiley and Sons, 1950.

43. A.W. Searcy, "Kinetics of Evaporation and Condensation Reactions," Ch. 6, in Chemical and Mechanical Properties of Inorganic Materials, A.W. Searcy, D.V. Ragone, and U. Colombo (eds.), Wiley-Interscience, 1970.
44. A.W. Searcy and D. Beruto, J. Phys. Chem., 78, 1298 (1974).
45. C.I. Whitman, J. Chem. Phys., 20, 161 (1952).
46. K. Motzfeldt, J. Phys. Chem., 59, 139 (1955).
47. P. Clausing, J. Vacuum Sci. and Tech., 8, 636 (1971):
Translated from [Ann. Physik, 12, 961 (1932)].
48. K.H. Lau, D. Cubicciotti, and D.L. Hildenbrand, J. Chem. Phys., 66, 4532 (1977).
49. G.M. Rosenblatt, "Evaporation from Solids," Ch. 3, in Treatise on Solid State Chemistry, Vol. 6A, N. B. Hannay (ed.), Plenum Press, 1976.
50. K.D. Carson, "The Knudsen Effusion Method," Ch. 5, in The Characterization of High Temperature Vapors, J. Margrave (ed.), Wiley, 1967.
51. R.C. Paule and J. Margrave, "Free-Evaporation and Effusion Techniques," Ch. 6, in The Characterization of High Temperature Vapors, J. Margrave (ed.), Wiley, 1967.
52. E.D. Cater, "The Effusion Method at Age 69: Current State of the Art," NBS Special Publication, 561, 1978.
53. G.F. Knutsen, Ph.D. Thesis, University of California, Berkeley, 1980.
54. D.J. Meschi, T.K. Basu, and A.W. Searcy, High Temp. Sci., 9, 263 (1977).

55. A.W. Searcy, private communication.
56. E.K. Powell and A.W. Searcy, *Met. Trans.*, 118, 427 (1980).
57. A.W. Searcy, "Entropy and High-Temperature Physical and Chemical Processes," Ch. 2, in Chemical and Mechanical Behavior of Inorganic Materials, A.W. Searcy, D.V. Ragone, and U. Colombo (eds.), Wiley-Interscience, 1970.
58. D. Beruto, R. Botter, and A.W. Searcy, unpublished work.
59. G.M. Rosenblatt, *J. Electrochem. Soc.*, 110, 563 (1963).
60. H. Manohar, "Topotactic Reactions in Inorganic Oxycompounds," Ch. 3, in Solid State Chemistry, C.N.R. Rao (ed.), Marcel Dekker, 1974.
61. F. Freund, K. Martens, and N.Sh. Ol-Eslami, *J. Thermal Anal.*, 8, 525 (1975).
62. G. Thomas and M.J. Goringe, Transmission Electron Microscopy of Materials, Wiley-Interscience, 1979.
63. P. Hirsch, A. Howie, R.B. Nicholson, D.W. Pashley, and M.J. Whelan, Electron Microscopy of Thin Crystals, 2nd ed., Robert E. Krieger Publishing Co., 1977.
64. J.W. Edington, Practical Electron Microscopy in Materials Science Vol.2 - Electron Diffraction in the Electron Microscope, MacMillan Philips Technical Library, 1975.
65. J.W. Edington, Practical Electron Microscopy in Materials Science Vol.4 - Typical Electron Microscope Investigations, MacMillan Philips Technical Library, 1976.
66. R.C. Evans, An Introduction to Crystal Chemistry, 2nd ed., Cambridge University Press, 1966.

67. R.W.G. Wyckoff, Crystal Structures Vol. 1, 2nd ed., Interscience Publishers, 1963.
68. R.W.G. Wyckoff, Crystal Structures Vol. 2, 2nd ed., Interscience Publishers, 1963.
69. F. Zigan and R. Rothhauer, N. Jahrb. Min., 4/5, 137 (1967).
70. Powder Diffraction Data, (International Centre for Diffraction Data, formerly Joint Committee in Powder Diffraction Standards).
71. F. Lippmann, Sedimentary Carbonate Minerals, Springer-Verlag, 1973.
72. A. Kelly and G. W. Groves, Crystallography and Crystal Defects, Addison-Wesley, 1970.
73. H.M. Otte and A.G. Crocker, Phys. Stat. Sol., 9, 441 (1965).
74. P.G. Partridge, Met. Rev., Rev. 118, 12, 169 (1967).
75. K.D. Oh, H. Morikawa, S. Iwai, and H. Aoki, Am. Mineral., 58, 1029 (1973).
76. K.W. Andrews, D.J. Dyson, and S.R. Keown, Interpretation of Electron Diffraction Patterns, Plenum Press, 1967.
77. J.W. Christian, Transformations in Metals and Alloys - Part. 1, Equilibrium and General Kinetic Theory, Pergamon Press, 1975.
78. D. Gratias, T. Portier, and M. Fayard, Acta Cryst., A35, 885 (1979).
79. R.W. Balluffi, A. Brokman, and A.H. King, Acta Metall., 30, 1453 (1982).
80. J.-C. Niepce, G. Watelle, and N.H. Brett, J. Chem. Soc. Faraday Trans. I, 74, 1530 (1978).

81. C.D. West, Am. Mineral., 19, 281 (1934).
82. J. Garrido, Am. Mineral., 36, 773 (1951).
83. J.F. Goodman, Proc. Roy. Soc., A247, 346 (1958).
84. R.S. Gordon and W.D. Kingery, J. Am. Cer. Soc., 49, 654 (1966).
85. W.H. Rhodes and B.J. Wuensch, J. Am. Cer. Soc., 56, 495 (1973).
86. M.M. Nicholson, Proc. Roy. Soc., A228, 490 (1955).
87. P.J. Anderson and A. Scholz, Mat. Res. Bull., 64, 2973 (1968).
88. R. Shuttleworth, Proc. Roy. Soc., A63, 444 (1950).
89. R.C. Garvie, Mat. Res. Bull., 1, 161 (1966).
90. F.W.C. Boswell, Proc. Roy. Soc., A64, 465 (1951).
91. I.F. Guilliat and N.H. Brett, Trans. Faraday Soc., 65, 3328 (1969).
92. J.S. Halliday, T.B. Rymer, K.H.R. Wright, Proc. Roy. Soc., A225, 548 (1954).
93. A. Cimino, P. Porta, and M. Valigi, J. Am. Cer. Soc., 49, 152 (1966).
94. G.W. Brindley and G. J. Ogilvie, Acta Cryst., 5, 412 (1952).
95. A.F. Moodie and C.E. Warble, Phil. Mag., 16, 891 (1967).
96. A.F. Moodie and C.E. Warble, J. Cryst. Growth, 10, 26 (1971).
97. I.F. Guilliat and N.H. Brett, Phil. Mag., 23, 647 (1971).
98. T.T. Dai, Ph.D. Thesis, University of California, Berkeley, 1981.
99. J.C. Niepce and G. Watelle, J. de Phys., 38, 365 (1977).
100. F.Freund and V. Spring, Mat. Res. Bull., 11 621 (1976).
101. M.C. Ball and H.F.W. Taylor, Min. Mag., 32, 754 (1961).
102. N.H. Brett and P.J. Anderson, Trans. Faraday Soc., 65, 251 (1967).

103. Z. Librant and R. Pampuch, J. Am. Cer. Soc., 51, 109 (1968).
104. D.R. Dasgupta, Min. Mag., 35, 634 (1965).
105. R. Singh Dev, N. Jahrb. Min., 1, 12 (1972).
106. N. Floquet and J.C. Niepce, J. Mat. Sci., 13, 766 (1978).
107. K.D. Oh, H. Morikawa, S. Iwai, and M. Akao, Yogyo Kyokai Shi (J. Cer. Soc. Japan), 88, 431 (1980).
108. L.W. Hobbs, "Radiation Effects in Analysis of Inorganic Specimens by TEM," Ch. 17, in Introduction to Analytical Electron Microscopy, J.J. Hren, J.I. Goldstein, and D.C. Joy (eds.), Plenum Press, 1979.
109. P.R. Swann and N.J. Tighe, Jernkont. Ann., 155, 497 (1971).
110. M-F. Rau, Ph.D. Thesis, University of California, Berkeley, 1985.
111. O. Scherzer, J. Appl. Phys., 20, 20 (1949).
112. R. Gronsky, "High Resolution Transmission Electron Microscopy" in Treatise on Materials Science and Technology: Experimental Techniques 19B, H. Herman (ed.), Academic Press, 1983.
113. S.J. Gregg and K.S.W. Sing, Adsorption, Surface Area, and Porosity, Academic Press, 1967.
114. L.D. Marks, Surface Sci., 150, 302 (1985).
115. M. Natrajan, T.S. Sarma, J.C. Ahluwalia, and C.N.R. Rao, Trans. Faraday Soc., 65, 3088 (1969).
116. D. Beruto, R. Botter, and A.W. Searcy, to be published.
117. F. Freund, Ber. Dtsch. Ker. Ges., 52, 53 (1975).
118. W.A. Deer, R.A. Howie, and J. Zussman, An Introduction to the Rock Forming Minerals, Longman, 1980.
119. D.J. Barber, J. Mat. Sci., 5, 1 (1970).

Table 1. Conventional Rate Equations Used in Kinetic Studies of Solid State Reactions.

Classification	Equation
1. Acceleratory	
Power law	$\alpha^{1/n} = kt$
Exponential law	$\ln(\alpha) = kt$
2. Sigmoid	
Avrami-Erofeev	$[-\ln(1-\alpha)]^{1/n} = kt$ $n = 2, 3, 4$
Prout-Tompkins	$\ln[\alpha/(1-\alpha)] = kt$
3. Deceleratory	
3.1 Based on diffusion mechanism	
One-dimensional	$\alpha^2 = kt$
Two-dimensional	$(1-\alpha)\ln(1-\alpha) + \alpha = kt$
Three-dimensional	$[1-(1-\alpha)^{1/3}]^2 = kt$
Ginstling-Brounshtein	$[1-(2\alpha/3)] - (1-\alpha)^{2/3} = kt$
3.2 Based on geometric models	
Contracting geometry	$1-(1-\alpha)^{1/n} = kt$ $n = 1, 2, 3$
3.3 Based on order with respect to	
First order	$-\ln(1-\alpha) = kt$
Second order	$1/(1-\alpha) = kt$
Third order	$1/(1-\alpha) = (kt)^2$

Table 2. Spectrographic Analyses* of Starting Materials (reported as oxide percent).

	G&A Mg(OH) ₂	Brucite A	Brucite B	Magnesite A	Magnesite B
Mg	----- Principal Constituent -----				
Si	1.0	<0.002	0.08	0.12	1.0
Fe	0.006	0.05	0.003	0.35	0.75
Ca	0.04	0.005	0.02	0.3	0.3
Mn		0.4	0.06	0.01	0.01
Sr					0.008
Ba					0.008
Al	0.02	<0.002	0.002	0.05	<0.003
Cu	<0.001			<0.001	<0.001
B	0.1			0.02	<0.01
Pb					<0.003
Co					<0.001
Ni	0.01				
Na	<0.1				
Mo			0.004		

G&A Mg(OH)₂: Mg(OH)₂ made in this lab. by a precipitation method.

Brucite A: Wood's Mine, Texas, Pennsylvania

Brucite B: Gabbs, Nye County, Nevada

Magnesite A: Baymag plant, Calgary, Alberta, Canada

Magnesite B: Djebel Hadifa, Algeria

*Analysis done by American Spectrographic Laboratories, San Francisco, California

Table 3. Decomposition of Single Crystal $Mg(OH)_2$ (Brucite A) at 605 K.

Sample Wt. (mg)	Edge Area (A_1) (m^2) $\times 10^5$	Cross Sectional Area (A_2) (m^2) $\times 10^4$	Total Area (m^2) $\times 10^4$	Initial Weight Loss Rate (W_{total}) (mg/min)	Apparent Max. Decomposition (%)
339.1	7.56	1.68	2.44	0.62	92
395.3	6.85	2.26	2.95	0.62	91
278.6	6.13	1.87	2.48	0.55	93
140.9	5.54	1.28	1.83	0.46	92
182.9	3.76	2.42	2.80	0.44	91
91.5	2.48	2.18	2.43	0.32	90

$$W_{total} = A_1 J_1 + A_2 J_2$$

$J_1 = 0.666 \pm 0.070$ mg/ m^2 ·min ; flux density parallel to basal plane

$J_2 = 0.077 \pm 0.019$ mg/ m^2 ·min ; flux density normal to basal plane

$$J_1/J_2 = 8.65$$

*Here J_1 and J_2 values are the calculated average ones with 15 first order simultaneous equations.

Table 4. Orientation Relationships Reported from the Decomposition Study of Calcite-Type Carbonates.

Crystal	Orientation Relationship	Reference
MgCO ₃ -MgO	(0001) _c // (111) _o [11 $\bar{2}$ 0] _c // (1 $\bar{1}$ 0) _o	Dasgupta (1965)
MgCO ₃ -MgO	(10 $\bar{1}$ 4) _c // (110) _o	Sing Dev
CaCO ₃ -CaO	[01 $\bar{1}$ 0] _c // (100) _o	(1972)
CdCO ₃ -CdO	[0001] _c // [1 $\bar{4}$ 0] _c (0 $\bar{1}$ 11) _c // (210) _o (10 $\bar{1}$ 1) _c // (210) _o ($\bar{1}$ 101) _c // (210) _o	Floquet and Niepce (1978)
MgCO ₃ -MgO	(1). (0001) _c // (111) _o [1 $\bar{2}$ 10] _c // [$\bar{1}$ 1 $\bar{2}$] _o (2). (0001) _c // ($\bar{1}$ 1 $\bar{2}$) _o [1 $\bar{2}$ 10] _c // [111] _o (3). (0001) _c // (110) _o [1 $\bar{2}$ 10] _c // [001] _o (4). (0001) _c // (001) _o [1 $\bar{2}$ 10] _c // [110] _o (1) is the major and (2), (3) and (4) the minor orientation relationships.	Oh et al. (1980)

c = Carbonate in the hexagonal cell of 6-formula unit
o = Oxide

Appendix 1. X-Ray Crystallographic Information of $Mg(OH)_2$, $MgCO_3$ and MgO .

7-239 MINOR CORRECTION

d	2.37	4.77	1.79	4.77	$Mg(OH)_2$
I/I ₀	100	90	55	90	MAGNESIUM HYDROXIDE (BRUCITE)
Rad. $CuK\alpha_1$ λ 1.5405 Filter Ni Dia. \star Cut off I/I ₀ DIFFRACTOMETER Ref. NBS CIRCULAR 539, VOLUME 6 (1956)					
Sys. HEXAGONAL (TRIGONAL) S.G. $D_{6h}^2 - P\bar{6}m1$ (164) a 3.147 b c 4.769 A C 1.5154 α β γ Z 1 Dx 2.37 Ref. ISID.					
d 1.561 n 1.581 f γ Sign + SV D 2.39 mp Color COLORLESS Ref. ISID. DANA'S SYSTEM OF MINERALOGY 7TH ED. VOL 1					
SAMPLE PREPARED AT NBS FROM MgO AND WATER HELD AT 600°C AND 20,000 PSI FOR 3 DAYS; SPECT. ANALYSIS SHOWS <0.1% Ca , <0.01% Ag , Al , B , Fe , Si , Sr , Ti ; <0.001% Ba , Cd , Cu . CaI_2 STRUCTURE TYPE. PATTERN MADE AT 26°C.					
d Å	I/I ₀	hkl	d Å	I/I ₀	hkl
4.77	90	001	0.9001	<1	105
2.725	6	100	.8974	2	204
2.365	100	101	.8923	2	301
1.794	55	102	.8643	6	213
1.573	35	110	.8156	4	115
1.494	16	111	.7865	4	220
1.373	16	103			
1.363	2	200			
1.310	12	201			
1.192	2	004			
1.183	10	202			
1.118	2	113			
1.092	4	104			
1.034	6	203			
1.030	2	210			
1.0087	8	211			
0.9543	2	005			
.9503	6	114			
.9455	8	212			
.9085	4	300			

8-479 MINOR CORRECTION

d	2.74	2.10	1.70	2.74	$MgCO_3$
I/I ₀	100	45	35	100	MAGNESIUM CARBONATE (MAGNESITE)
Rad. $CuK\alpha_1$ λ 1.5405 Filter Ni Dia. \star Cut off I/I ₀ DIFFRACTOMETER Ref. NBS CIRCULAR 539 Z 28 (1957)					
Sys. TRIGONAL S.G. $R\bar{3}c$ (167) a 4.6332 b c 15.015 A C 3.2407 α β γ Z 6 (hex) Dx 3.009 2 (rhomb) Ref. ISID.					
d 1.510 n 1.700 f γ Sign - SV D mp Color COLORLESS Ref. ISID.					
SAMPLE FROM THE BAKER CHEMICAL CO., PHILLIPSBURG, N.J., HEATED AT 120,000 PSI AND 280°C FOR 4 DAYS. SPECT. ANAL. <0.1% Ca , Mg <0.01% Al , Fe , Mn , Mo , Pb , Si , Sr ; <0.001% Ba , Cd , Cu , Ni . CALCITE STRUCTURE TYPE. PATTERN MADE AT 25°C.					
d Å	I/I ₀	hkl	d Å	I/I ₀	hkl
2.742	100	104	1.0669	4	2.1.10.134
2.503	18	006	1.0510	2	226
2.318	4	110	1.0145	<1	1.2.11
2.102	45	113	0.9692	2	404
1.939	12	022	.9573	2	318
1.769	4	024	.9455	<1	2.0.14
1.700	35	116			2.1.13
1.510	4	211	.9188	4	1.1.15.321
1.488	6	122			3.0.12
1.426	4	L.O.10.214	.9134	8	1.0.16
1.371	4	208			324
1.354	8	119	.8941	<1	048
1.338	8	300	.8837	2	140
1.252	4	0.0.12	.8758	2	418.3.1.11
1.2386	<1	217	.8628	<1	327
1.2022	<1	0.2.10	.8460	<1	0.0.18
1.1798	<1	128.306	.8346	<1	4.0.10
1.1583	<1	220	.8265	<1	416.238
1.1297	<1	2.0.11	.7981	2	2.1.16.502
1.1011	<1	1.1.12			

4-0829 MAJOR CORRECTION

d	2.11	1.49	1.22	2.431	MgO
I/I ₀	100	52	12	10	MAGNESIUM OXIDE PERICLASE
Rad. $CuK\alpha_1$ λ 1.5405 Filter Ni Dia. \star Cut off I/I ₀ DIFFRACTOMETER Ref. SWANSON AND TAYOR, JC FEL. REPORTS, NBS 1949					
Sys. CUBIC S.G. $O_h^c - Fm\bar{3}m$ a 4.213 b c A C α β γ Z 4 Ref. ISID.					
d n 1.732 f γ Sign SV D ₃ 581 mp Color Ref. ISID.					
HIGH PURITY PHOSPHOR SAMPLE FROM RCA HEATED AT 1800°C FOR 3 HRS. AT 26°C TO REPLACE 1-1235, 2-1207, 3-0898					
d Å	I/I ₀	hkl	d Å	I/I ₀	hkl
2.431	10	111			
2.106	100	200			
1.499	52	220			
1.270	4	311			
1.216	12	222			
1.0533	5	400			
0.9665	2	331			
.9419	17	420			
.8600	15	422			
.8109	3	511			

Appendix 2. Transformation of Miller Indices Following a Change of Unit Cell.

Miller indices of old cell; hkl

Miller indices of new cell; HKL

$$\begin{pmatrix} H \\ K \\ L \end{pmatrix} = \begin{pmatrix} t_{11} & t_{12} & t_{13} \\ t_{21} & t_{22} & t_{23} \\ t_{31} & t_{32} & t_{33} \end{pmatrix} \begin{pmatrix} h \\ k \\ l \end{pmatrix}$$

where t_{ij} relates the translation vectors of old cell to new cell as follows, i.e., a, b, c to A, B, C

$$\begin{pmatrix} A \\ B \\ C \end{pmatrix} = \begin{pmatrix} t_{11} & t_{12} & t_{13} \\ t_{21} & t_{22} & t_{23} \\ t_{31} & t_{32} & t_{33} \end{pmatrix} \begin{pmatrix} a \\ b \\ c \end{pmatrix}$$

(1) Transformation between rhombohedral and hexagonal unit cell.

$$\begin{pmatrix} H \\ K \\ L \end{pmatrix}_{\text{hex}} = \begin{pmatrix} 1 & -1 & 0 \\ 0 & 1 & -1 \\ 1 & 1 & 1 \end{pmatrix} \begin{pmatrix} h \\ k \\ l \end{pmatrix}_{\text{rh.}} ; \begin{pmatrix} H \\ K \\ L \end{pmatrix}_{\text{rh.}} = \begin{pmatrix} \frac{2}{3} & \frac{1}{3} & \frac{1}{3} \\ -\frac{1}{3} & \frac{1}{3} & \frac{1}{3} \\ -\frac{1}{3} & -\frac{2}{3} & \frac{1}{3} \end{pmatrix} \begin{pmatrix} h \\ k \\ l \end{pmatrix}_{\text{hex.}}$$

(2) Transformation of rhombohedral to other rhombohedral unit cells

(Z = number of the formula unit in a unit cell)

(i) Transformation between rhombohedral unit cells of Z = 1 and

Z = 2

$$\begin{pmatrix} H \\ K \\ L \end{pmatrix}_{Z=1} = \begin{pmatrix} \frac{1}{2} & -\frac{1}{2} & \frac{1}{2} \\ \frac{1}{2} & \frac{1}{2} & -\frac{1}{2} \\ -\frac{1}{2} & \frac{1}{2} & \frac{1}{2} \end{pmatrix} \begin{pmatrix} h \\ k \\ l \end{pmatrix}_{Z=2} ; \begin{pmatrix} H \\ K \\ L \end{pmatrix}_{Z=2} = \begin{pmatrix} 1 & 1 & 0 \\ 0 & 1 & 1 \\ 1 & 0 & 1 \end{pmatrix} \begin{pmatrix} h \\ k \\ l \end{pmatrix}_{Z=1}$$

ii) Transformation between rhombohedral cells of Z=1 and Z=4

$$\begin{pmatrix} H \\ K \\ L \end{pmatrix}_{Z=1} = \begin{pmatrix} \frac{1}{2} & 0 & \frac{1}{2} \\ \frac{1}{2} & \frac{1}{2} & 0 \\ 2 & \frac{1}{2} & \frac{1}{2} \end{pmatrix} \begin{pmatrix} h \\ k \\ l \end{pmatrix}_{Z=4} \quad \begin{pmatrix} H \\ K \\ L \end{pmatrix}_{Z=4} = \begin{pmatrix} 1 & 1 & -1 \\ -1 & 1 & 1 \\ 1 & -1 & 1 \end{pmatrix} \begin{pmatrix} h \\ k \\ l \end{pmatrix}_{Z=1}$$

$$\begin{pmatrix} H \\ K \\ L \end{pmatrix}_{Z=2} = \begin{pmatrix} 1 & \frac{1}{2} & \frac{1}{2} \\ \frac{1}{2} & 1 & \frac{1}{2} \\ \frac{1}{2} & \frac{1}{2} & 1 \end{pmatrix} \begin{pmatrix} h \\ k \\ l \end{pmatrix}_{Z=4} ; \begin{pmatrix} H \\ K \\ L \end{pmatrix}_{Z=4} = \begin{pmatrix} \frac{3}{2} & \frac{1}{2} & \frac{1}{2} \\ -\frac{1}{2} & \frac{3}{2} & -\frac{1}{2} \\ -\frac{1}{2} & -\frac{1}{2} & \frac{3}{2} \end{pmatrix} \begin{pmatrix} h \\ k \\ l \end{pmatrix}_{Z=2}$$

Appendix 3. Crystallographic Relationships for Hexagonal Systems

(1) Indices of directions

3-axis notation ; UVW

4-axis notation ; uvtw where $u+v+t = 0$

$$U = u-t \quad ; \quad V = v-t \quad , \quad W = w$$

$$u = \frac{1}{3} (2U-V) \quad ; \quad v = \frac{1}{3} (2V-U) \quad , \quad t = -(u+v) \quad , \quad w = W$$

(2) Indices of planes

Miller index ; HKL

Miller-Bravais index ; hkil where $h+k+i = 0$

$$(HKL) = (hkil)$$

(3) Relationship between a crystal plane (hkil) and its normal direction [uvtw].

i) The direction [uvtw] normal to the plane (hkil)

$$[uvtw] = [hkil\lambda^{-2}]$$

ii) The plane (hkil) normal to the direction [uvtw]

$$(hkil) = (uvtw\lambda^2)$$

$$\text{where } \lambda^2 = \frac{2}{3} \left(\frac{c}{a}\right)^2.$$

(4) Dot products

Direct lattice vector, $r = ua_1 + va_2 + ta_3 + wc = [uvw]$

Reciprocal lattice vector, $g = hA_1^* + kA_2^* + iA_3^* + lC^* = [hki]$

i) $g \cdot r = hu + kv + it + lw$

ii) $r_1 \cdot r_2 = \frac{3a^2}{2} (u_1u_2 + v_1v_2 + t_1t_2 + \lambda^2 w_1w_2)$

iii) $g_1 \cdot g_2 = \frac{2}{3a^2} (h_1h_2 + k_1k_2 + i_1i_2 + \lambda^{-2} l_1l_2)$

(5) Magnitude of vectors

i) $|r|^2 = \frac{3a^2}{2} (u^2 + v^2 + t^2 + \lambda^2 w^2)$

ii) $|g|^2 = \frac{2}{3a^2} (h^2 + k^2 + i^2 + \lambda^{-2} l^2) = \frac{1}{d^2}$

(6) Angle relationships

i) Interdirectional angle

$$\cos (r_1 \cdot r_2) = \frac{r_1 \cdot r_2}{|r_1| |r_2|} = \frac{u_1u_2 + v_1v_2 + t_1t_2 + \lambda^2 w_1w_2}{(u_1^2 + v_1^2 + t_1^2 + \lambda^2 w_1^2)^{1/2} (u_2^2 + v_2^2 + t_2^2 + \lambda^2 w_2^2)^{1/2}}$$

ii) Interplanar angle

$$\cos (\mathbf{g}_1 \cdot \mathbf{g}_2) = \frac{\mathbf{g}_1 \cdot \mathbf{g}_2}{|\mathbf{g}_1| |\mathbf{g}_2|} = \frac{h_1 h_2 + k_1 k_2 + i_1 i_2 + \lambda^{-2} l_1 l_2}{(h_1^2 + k_1^2 + i_1^2 + \lambda^{-2} l_1^2)^{1/2} (h_2^2 + k_2^2 + i_2^2 + \lambda^{-2} l_2^2)^{1/2}}$$

iii) Angle between a plane and a direction

$$\cos (\mathbf{r} \cdot \mathbf{g}) = \frac{\mathbf{r} \cdot \mathbf{g}}{|\mathbf{r}| |\mathbf{g}|} = \frac{hu + kv + it + lw}{(u^2 + v^2 + t^2 + \lambda^2 w^2)^{1/2} (h^2 + k^2 + i^2 + \lambda^{-2} l^2)^{1/2}}$$

Appendix 4. Theoretical porosity resulting from the decomposition reactions without external shrinkage.

$$\text{porosity (\%)} = \frac{\text{molar volume of reactant} - \text{molar volume of product}}{\text{molar volume of reactant}} \times 100$$

	<u>Mg(OH)₂</u>	<u>MgCO₃</u>	<u>MgO</u>
Density (g/cm ³)	2.36	2.96	3.58
Molar weight (g/mole)	58.33	84.32	40.3
Molar volume (cm ³ /mole)	24.72	28.49	11.26

From the decomposition of Mg(OH)₂

$$\text{porosity of MgO} = 54.4\%$$

From the decomposition of MgCO₃

$$\text{porosity of MgO} = 60.5\%$$

FIGURE CAPTIONS

- Fig. 1. Hypothetical Gibbs free energy vs. composition diagram for the system $\text{MgO-Mg(OH)}_2\text{-H}_2\text{O}$.
- Fig. 2. SEM micrographs of starting materials; (A) G&A Mg(OH)_2 and (B) Magnesite A.
- Fig. 3. Thermogravimetric apparatus (Apparatus A).
- Fig. 4. Thermogravimetric apparatus (Apparatus B).
- Fig. 5. Knudsen cells used for the decomposition of MgCO_3 .
- Fig. 6. $\log P_{\text{Zn}}$ vs. $1/T$ plot for the temperature calibration of Apparatus A.
- Fig. 7. Calibrated temperatures of Apparatus A ; Broken line indicates the extrapolation from the experimental range of heavy line. Diagonal line indicates reference for no deviation of temperature.
- Fig. 8. $\log P_{\text{LiI}}$ vs. $1/T$ plot for the temperature calibration of Apparatus B ; Points numbered in order measured.
- Fig. 9. Calibrated temperatures of Apparatus B ; Broken line indicates the extrapolation from experimental range of heavy line. Diagonal line indicates reference for no deviation of temperature.
- Fig. 10. Rate of decomposition of single crystal Mg(OH)_2 .
- Fig. 11. Rate of decomposition of powder (G&A) Mg(OH)_2 .
- Fig. 12. Effective initial flux density (j_b) vs. sample weight from the decomposition of G&A Mg(OH)_2 .

- Fig. 13. Log P_{H_2O} vs. $1/T$ plot from the open cell study of decomposition of G&A $Mg(OH)_2$ and those from other studies; G&A from Giaque and Archibald and K&G from Kay and Gregory.
- Fig. 14. Rate of decomposition of single crystal $MgCO_3$.
- Fig. 15. Rate of decomposition of powder $MgCO_3$ (Magnesite A).
- Fig. 16. Log P_{CO_2} vs. $1/T$ plot from single crystal and Knudsen cell experiments of $MgCO_3$ decomposition. Extrapolated values are from the Whitman-Motzfeltdt extrapolation to zero orifice area with the pressures measured during the 0 to 1% decomposition. The pressures from an orifice diameter of 9.80 mm are those from the open crucible.
- Fig. 17. Structure of hexagonal $Mg(OH)_2$.
- Fig. 18. Structure of rhombohedral and hexagonal $MgCO_3$.
- Fig. 19. Rhombohedral and hexagonal unit cells showing the transformation relationship between the two cells. Refer to Appendix 2 for the transformation equations.
- Fig. 20. [0001] projection of calcite-type carbonate showing the oxygen octahedra of cation; M indicates the cation and Z the height of ions in the c-axis of hexagonal structure of 6-formula unit.
- Fig. 21. Calcite-type carbonate of three rhombohedral unit cells; Z = number of formula unit in the unit cells.
- Fig. 22. Structure of face centered cubic MgO .

- Fig. 23. Retention of external shape and size of crystals during the decomposition of $\text{Mg}(\text{OH})_2$; (A) and (B) Optical micrographs, and (C) and (D) TEM micrographs of before and after the decomposition, respectively.
- Fig. 24. Sequential diffraction patterns of $[0001] \text{Mg}(\text{OH})_2$ decomposition to MgO ; (A) $\text{Mg}(\text{OH})_2$, (B) partly decomposed $\text{Mg}(\text{OH})_2$, and (C) MgO .
- Fig. 25. Diffraction patterns in the $[0001] \text{Mg}(\text{OH})_2$; (A) partly decomposed $\text{Mg}(\text{OH})_2$, (B) partly decomposed $\text{Mg}(\text{OH})_2$ and gold ring pattern. Trace of microdensitometer measurement of (B); H, O, and G indicate the hydroxide, oxide, and gold, respectively.
- Fig. 26. Stereographic projection representing the orientation relationship between $\text{Mg}(\text{OH})_2$ and its vacuum decomposed MgO .
- Fig. 27. MgO cubic particles rotated 60 degrees to each other about the $[111] \text{MgO}$.
- Fig. 28. Sequential diffraction patterns of $[11\bar{2}0] \text{Mg}(\text{OH})_2$ decomposition to MgO ; (A) $\text{Mg}(\text{OH})_2$, (B) partly decomposed $\text{Mg}(\text{OH})_2$, and (C) MgO .
- Fig. 29. Sequential diffraction patterns of $[1\bar{1}02] \text{Mg}(\text{OH})_2$ decomposition to MgO ; (A) $\text{Mg}(\text{OH})_2$, (B) partly decomposed $\text{Mg}(\text{OH})_2$, and (C) MgO .
- Fig. 30. Sequential bright field images of $\text{Mg}(\text{OH})_2$ decomposition to MgO corresponding to the diffraction patterns of Fig. 24.

- Fig. 31. Bright field images of $\text{Mg}(\text{OH})_2$; (A) G&A $\text{Mg}(\text{OH})_2$, (B) Brucite B, and (C) Brucite A.
- Fig. 32. Bright field image of $\text{Mg}(\text{OH})_2$ at the liquid nitrogen temperature.
- Fig. 33. Bright field images of $\text{Mg}(\text{OH})_2$ before (A) and after (B) two hour flow of ~ 370 Pa water vapor.
- Fig. 34. Bright field images and their corresponding diffraction patterns of $\text{Mg}(\text{OH})_2$.
- Fig. 35. Diffraction pattern of $[0001]$ $\text{Mg}(\text{OH})_2$. Note the streak-like spots around $(10\bar{1}0)$ $\text{Mg}(\text{OH})_2$ spots.
- Fig. 36. Bright field image and its corresponding diffraction pattern of slightly decomposed $\text{Mg}(\text{OH})_2$. Note the (200) MgO diffraction spot ($d = 0.2106$ nm) is too close to be separately visible from $(10\bar{1}1)$ $\text{Mg}(\text{OH})_2$ spot ($d = 0.2365$ nm).
- Fig. 37. Decomposition of $\text{Mg}(\text{OH})_2$ in the $[0001]$ orientation by the heating of focussed electron beam; Bright center area of the picture is decomposed.
- Fig. 38. Retention of external shape and size of crystals during the decomposition of MgCO_3 ; (A) and (B) Optical micrographs, and (C) and (D) TEM micrographs of before and after the decomposition, respectively.
- Fig. 39. Sequential diffraction patterns of $[0001]$ MgCO_3 decomposition to MgO; (A) MgCO_3 , (B) partly decomposed MgCO_3 , and (C) MgO.

- Fig. 40. Stereographic projection representing the orientation relationship between MgCO_3 and its vacuum decomposed MgO .
- Fig. 41. Sequential diffraction patterns of $[\bar{1}0\bar{1}1]$ MgCO_3 decomposition to MgO ; (A) MgCO_3 , (B) partly decomposed MgCO_3 , and (C) MgO .
- Fig. 42. Diffraction pattern of MgO from the decomposition of $[0001]$ MgCO_3 . Note the weak MgO spots of (111), (200), and (420) belong to two minor orientations.
- Fig. 43. Bright field image of partly decomposed MgCO_3 ; Bright area is decomposed.
- Fig. 44. Bright field images of MgCO_3 (A) and partly decomposed MgCO_3 (B) corresponding to Fig. 41A&B, respectively.
- Fig. 45. Bright field image of MgO from the decomposition of MgCO_3 corresponding to Fig. 41C. Note the crack crossing the center of the picture.
- Fig. 46. Projection of $[0001]$ $\text{Mg}(\text{OH})_2$ and $[111]$ MgO showing the coordination of oxygen octahedra.
- Fig. 47. Projection of $[0001]$ MgCO_3 and $[111]$ MgO showing the triangular faces of oxygen octahedra.
- Fig. 48. TEM micrograph of MgO particles from the decomposition of $\text{Mg}(\text{OH})_2$ by electron beam heating.
- Fig. 49. TEM micrograph of MgO particles from the decomposition of $\text{Mg}(\text{OH})_2$ by hot stage heating.

- Fig. 50. Schematic spatial arrangements of MgO cubes from the decomposition of $\text{Mg}(\text{OH})_2$. After Guilliat and Brett, Phil. Mag., 21, 671 (1970).
- Fig. 51. TEM micrograph of MgO particles from the decomposition of MgCO_3 by electron beam heating.
- Fig. 52. Bright field and two dark field micrographs (C) and (D) which were taken with the diffraction spots (c) and (d) of diffraction pattern (A), respectively.
- Fig. 53. High resolution image of $[100]$ MgO from the decomposition of $\text{Mg}(\text{OH})_2$, its electron diffraction (bottom left), and optical diffraction pattern (bottom right).
- Fig. 54. TEM micrograph of $[111]$ MgO from the decomposition of $\text{Mg}(\text{OH})_2$.
- Fig. 55. Optical diffractograms of bright field images (magnification 30000) of (A) $[100]$, (B) $[110]$, and (C) $[111]$ MgO from the decomposition of $\text{Mg}(\text{OH})_2$ and (D) the high resolution image (magnification 380000) of Fig. 53.
- Fig. 56. Optical diffractograms of bright field images (magnification 36000) of (A) MgO orientation of Fig. 41C, and (B) $[111]$ MgO from the decomposition of MgCO_3 and (C) the high resolution image (magnification 380000) of Fig. 53.
- Fig. 57. TEM micrographs of partly decomposed $\text{Mg}(\text{OH})_2$; (A) and (B) $[0001]$ $\text{Mg}(\text{OH})_2$ and their corresponding diffraction pattern (C), and (D) $[11\bar{2}0]$ $\text{Mg}(\text{OH})_2$ and its corresponding diffraction pattern (E).

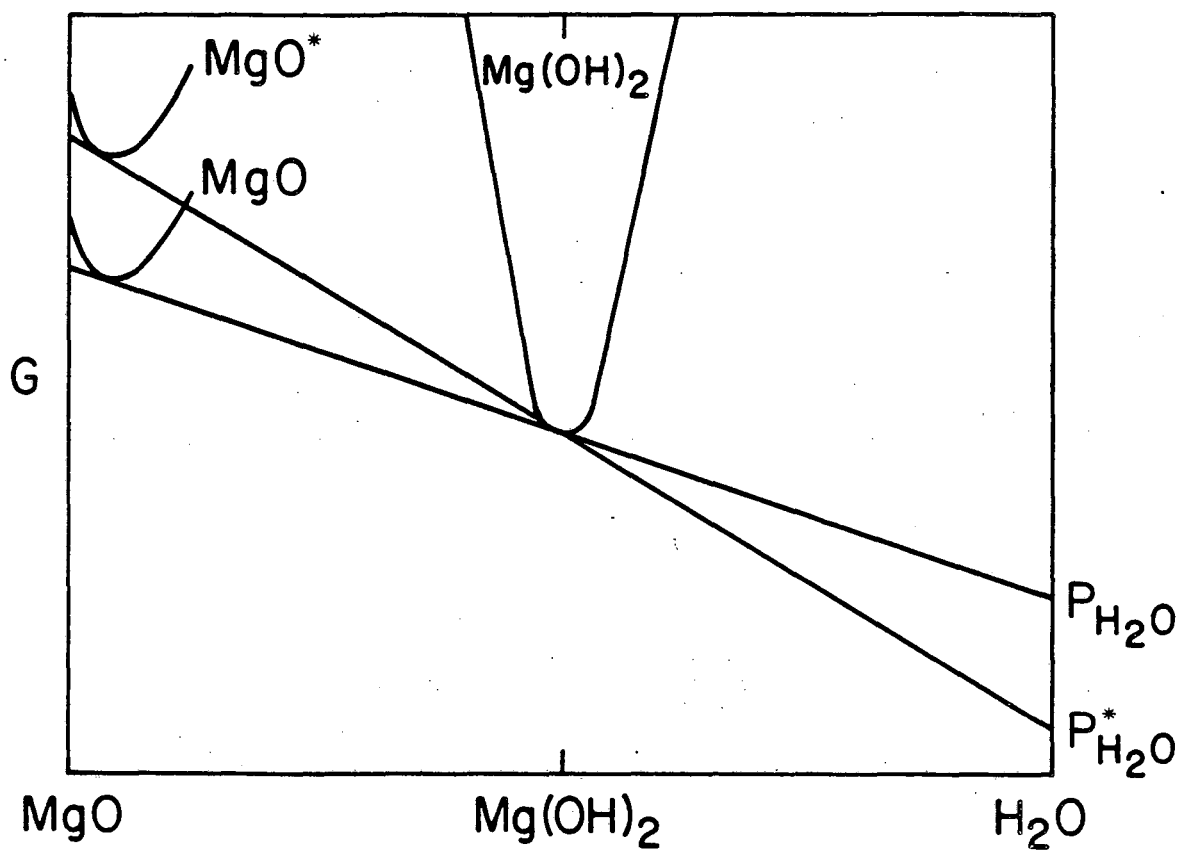
Fig. 58. SEM micrographs of partly decomposed $\text{Mg}(\text{OH})_2$; (A) initial cleavage surface, (B) cleavage surface of middle of the crystal showing the uncracked (left) and cracked (right) area, and (C) edge surface normal to the cleavage surface.

Fig. 59. Bright field images of MgO from the decomposition of MgCO_3 .

Fig. 60. SEM micrographs of partly decomposed MgCO_3 . Note the cracks are continuous to the reaction interfaces.

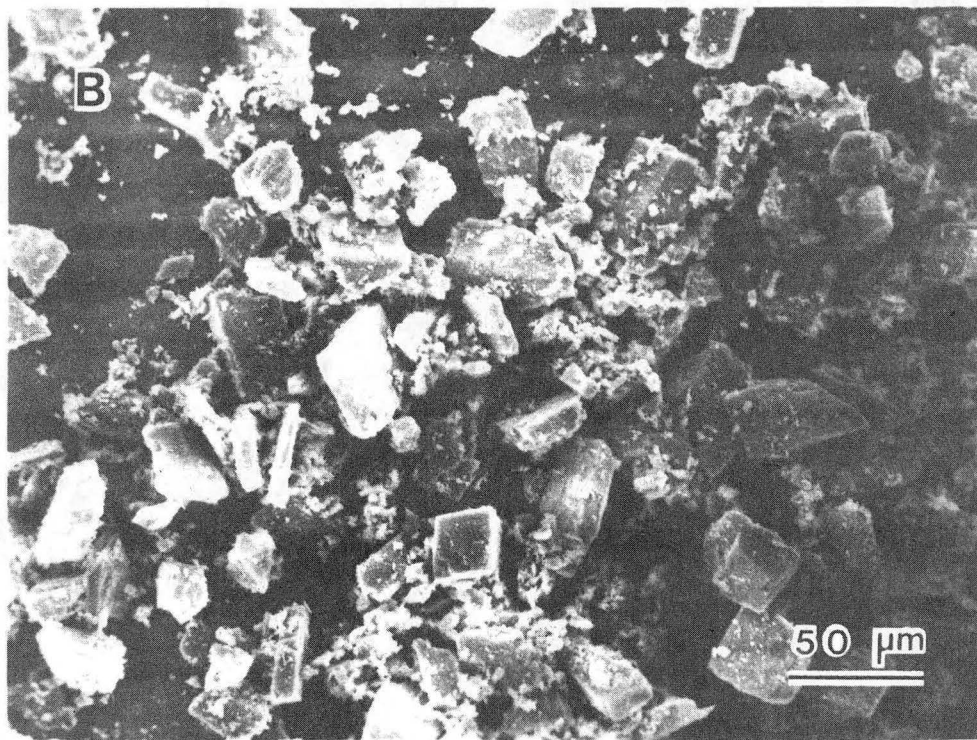
Fig. 61. SEM micrographs of partly decomposed MgCO_3 ; (A) initial cleavage surface, (B) cleavage surface of middle of the crystal showing the decomposed (left) and undecomposed (right) area, and (C) magnified micrograph of (B).

Fig. 62. Schematic drawing of sequential mechanism of $\text{Mg}(\text{OH})_2$ decomposition.



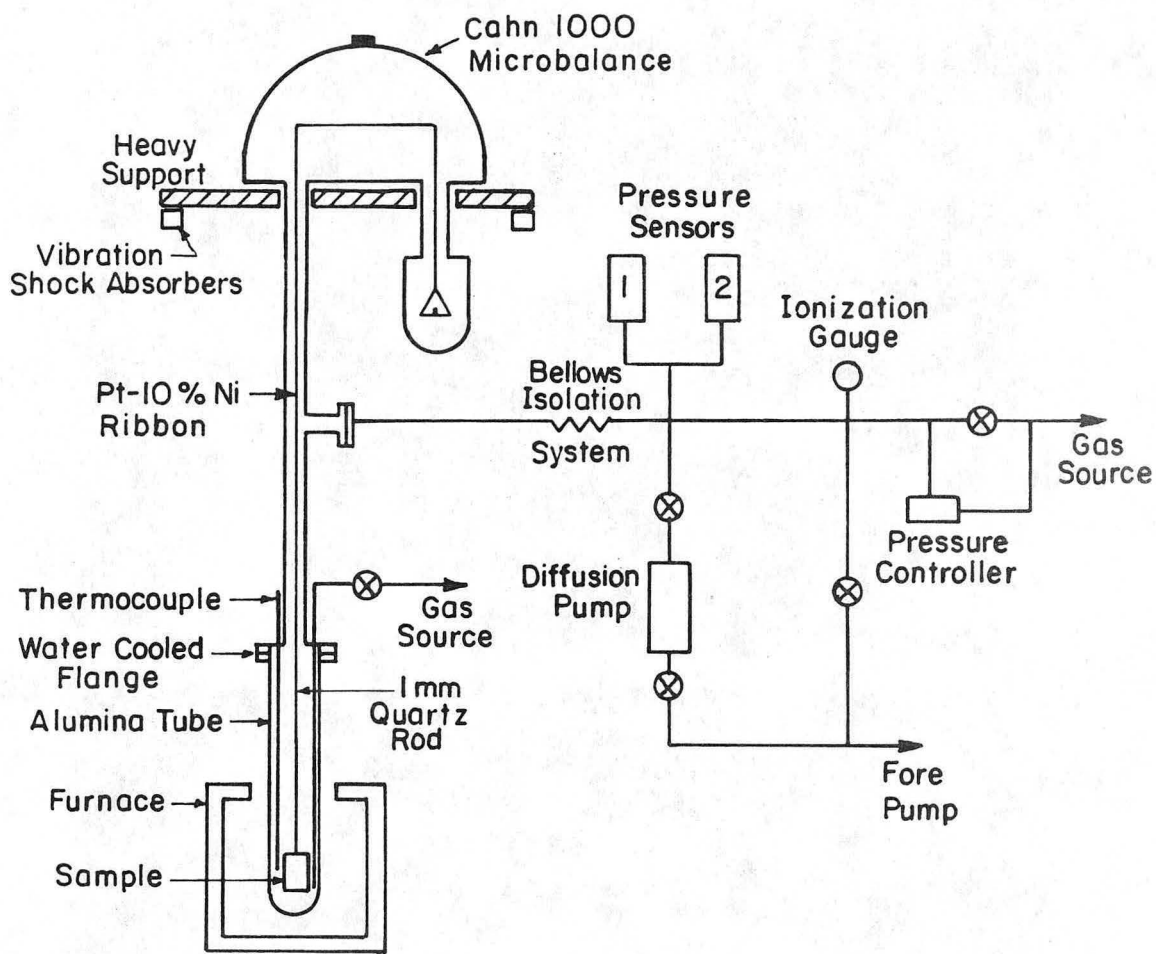
XBL823-2081

Fig. 1



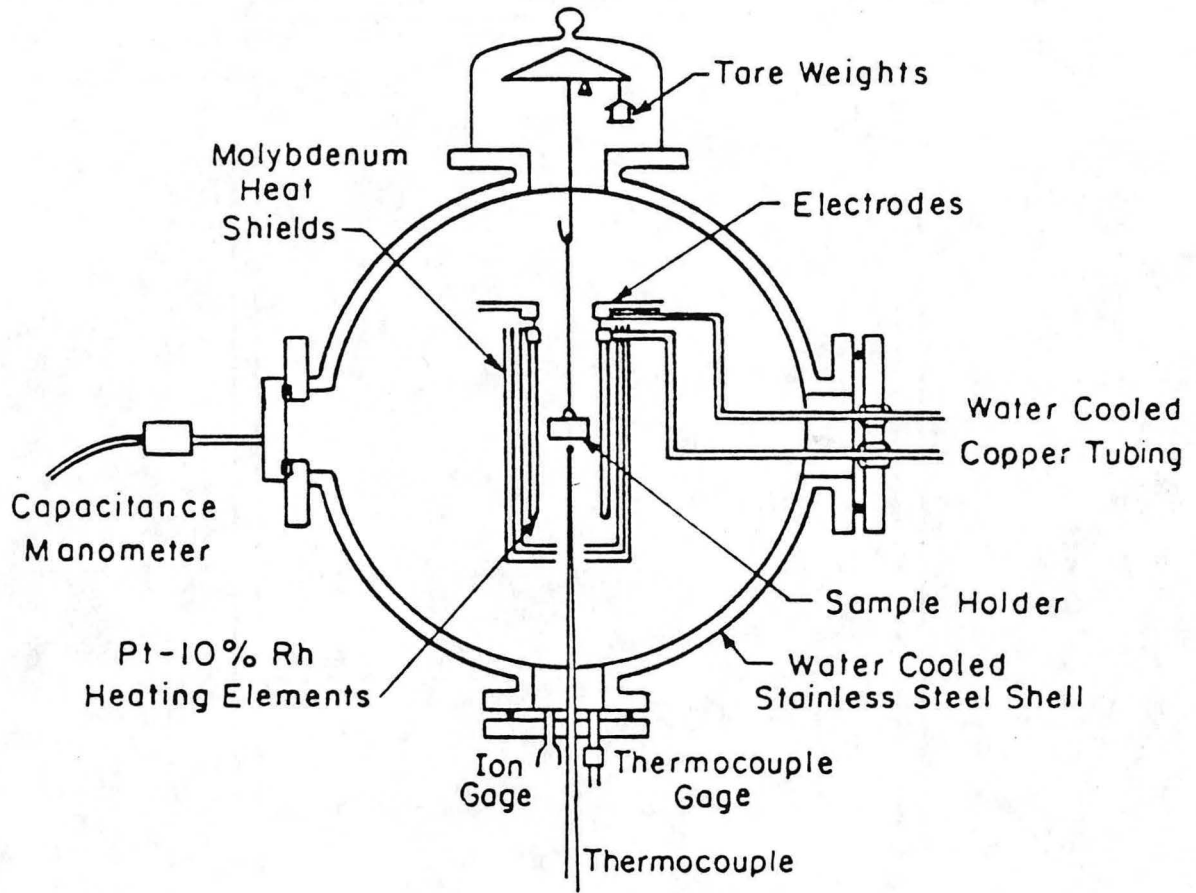
XBB 859-7044

Fig. 2



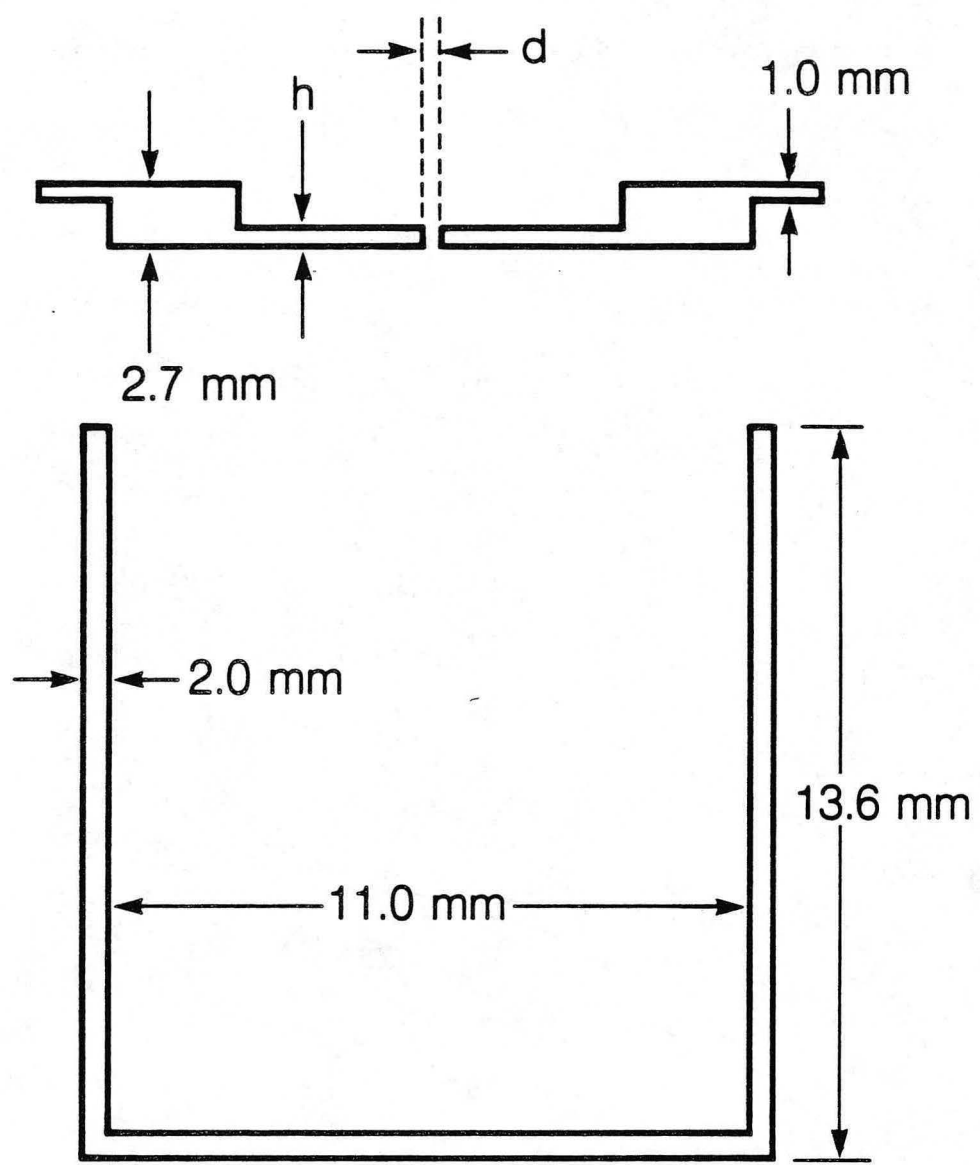
XBL 801-4515

Fig. 3



XBL784-4857

Fig. 4

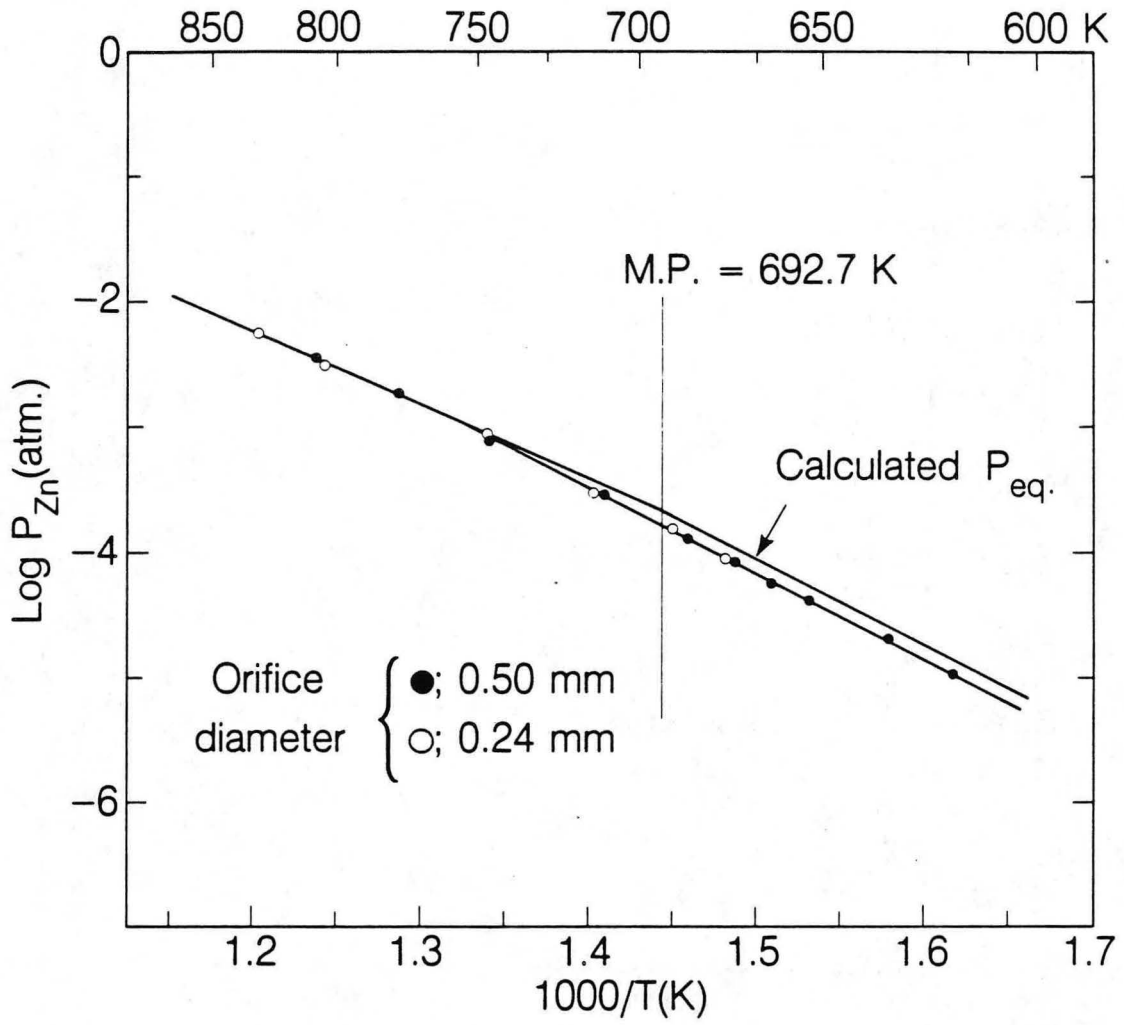


Orifice diameter, d 0.21 0.42 (mm)

Orifice height, h 0.90 1.10 (mm)

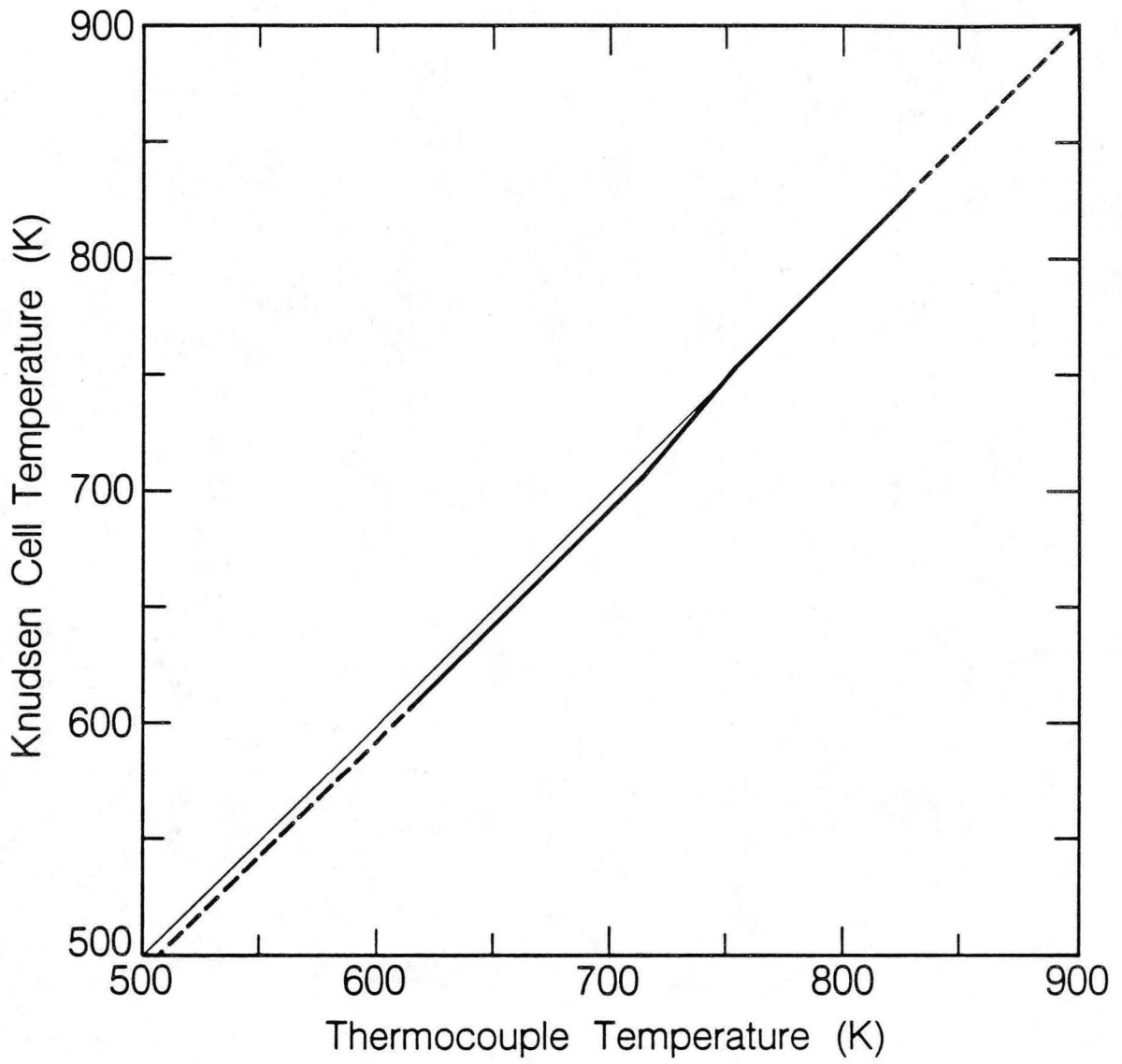
XBL 859-3842

Fig. 5



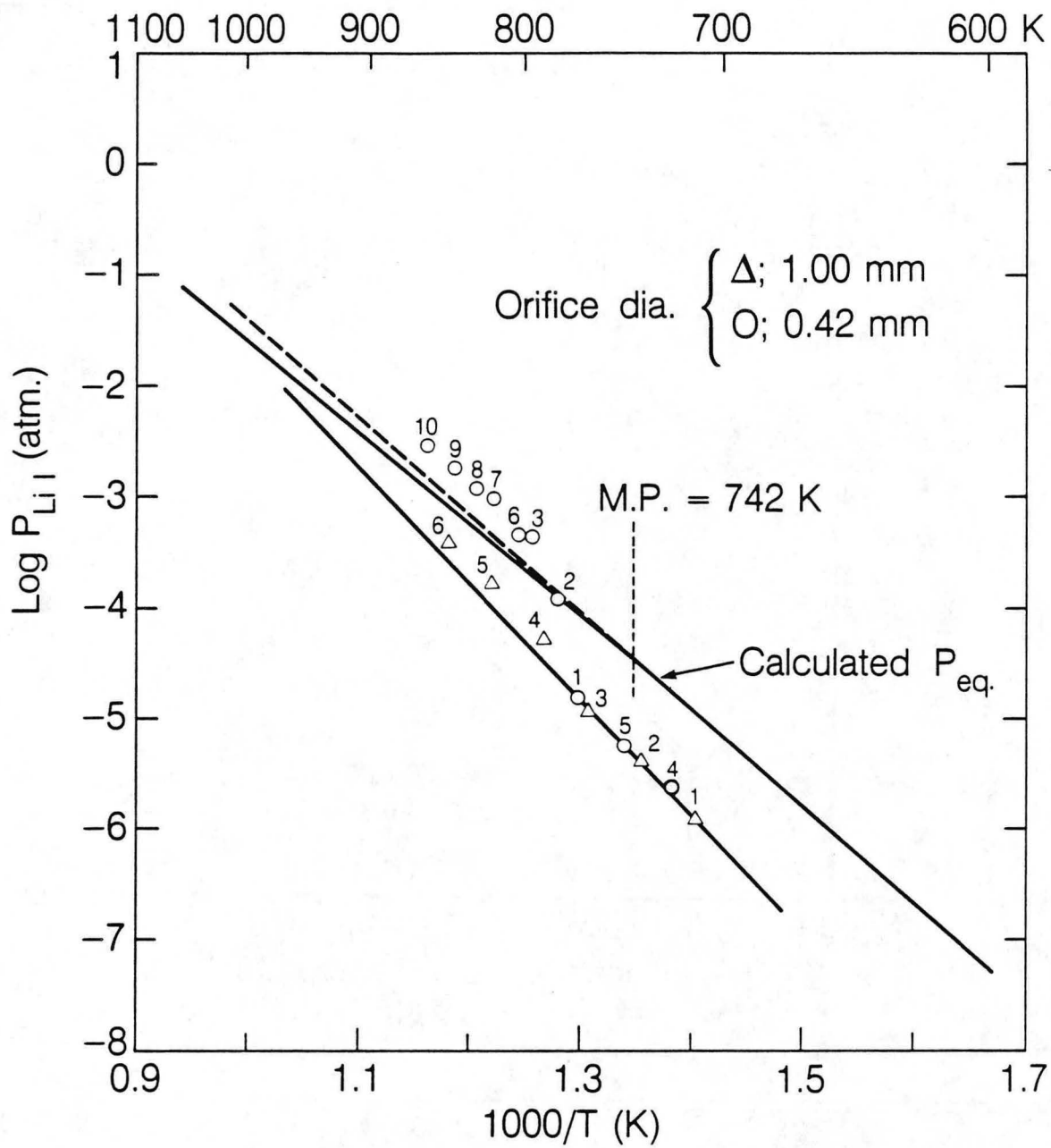
XBL 859-11691

Fig. 6



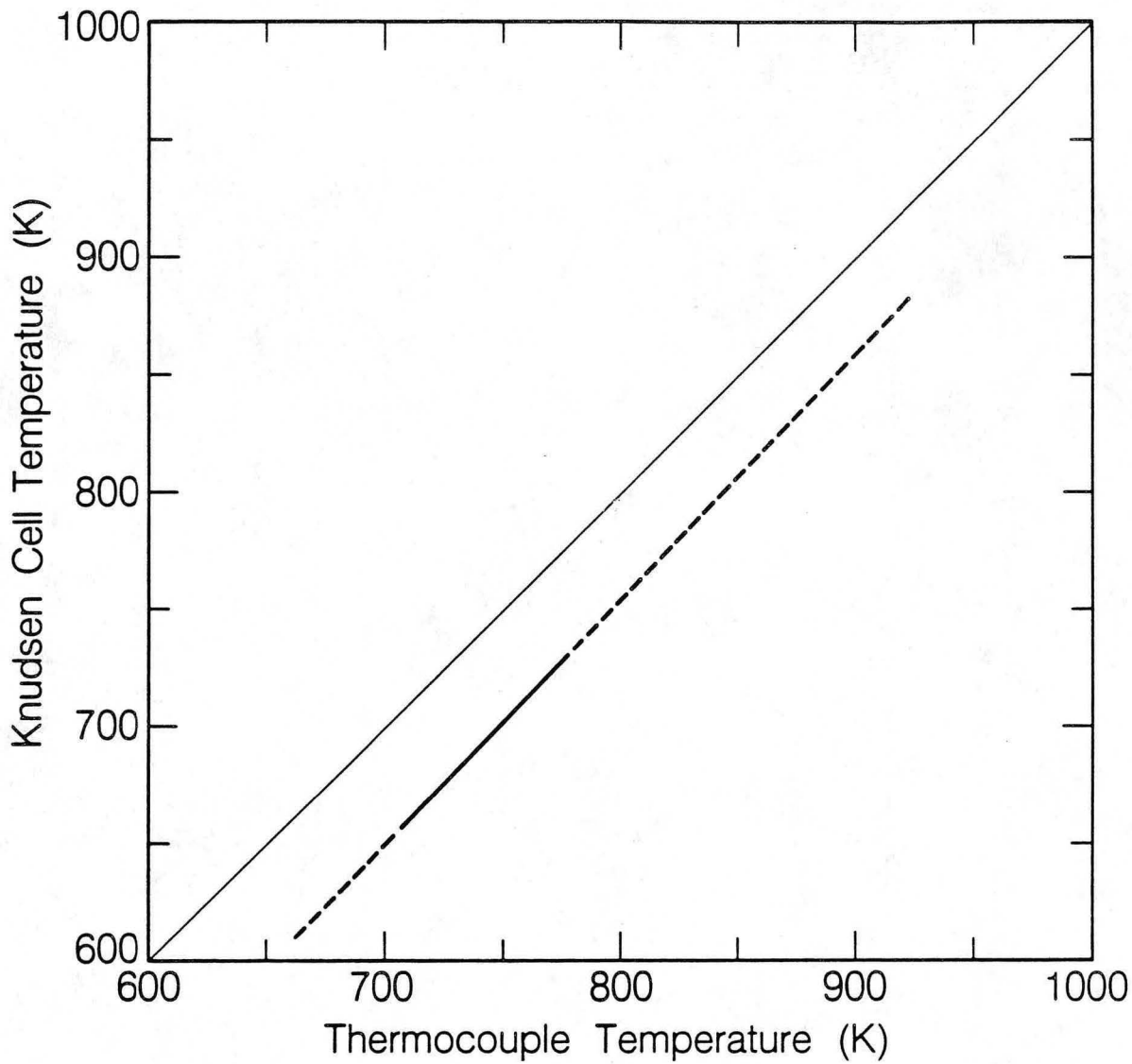
XBL 859 3837

Fig. 7



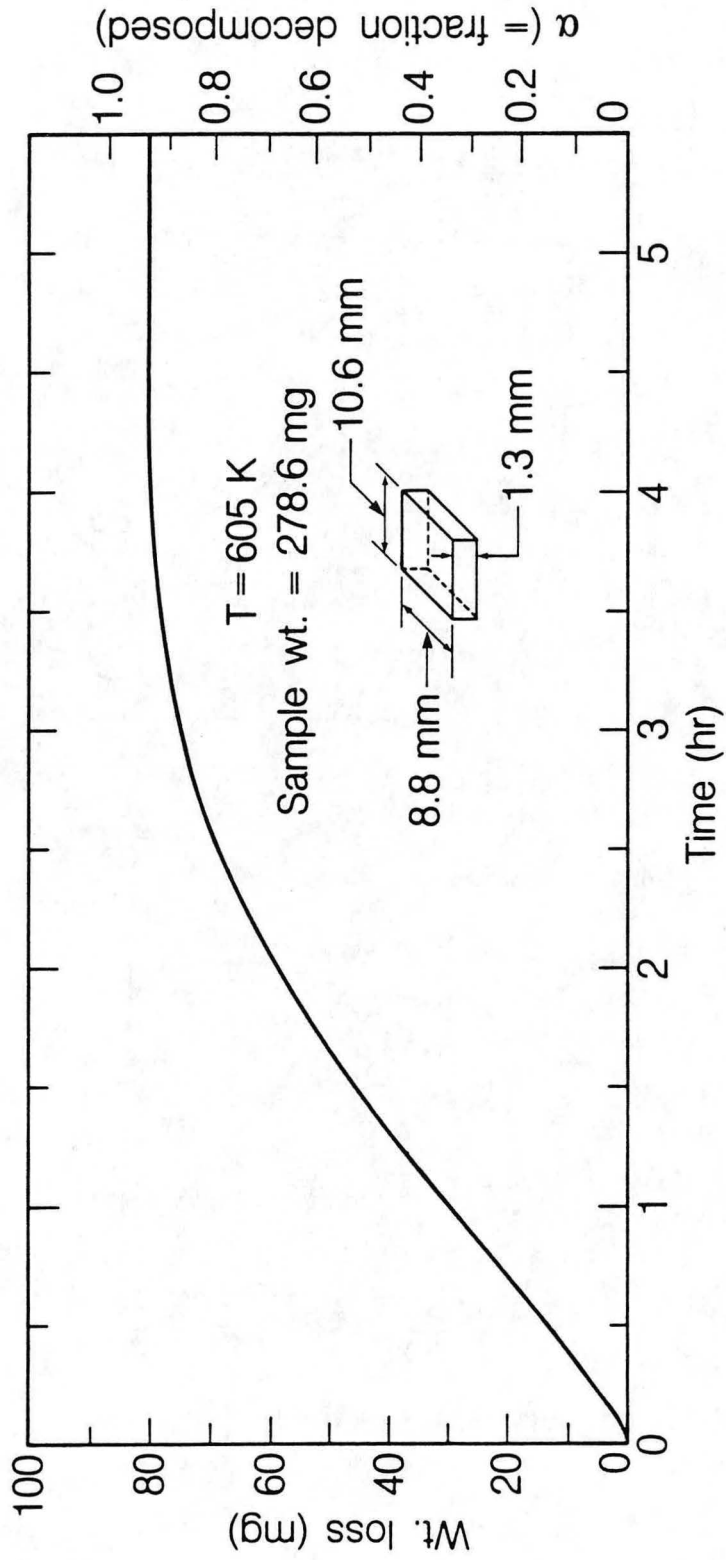
XBL 859 3840

Fig. 8



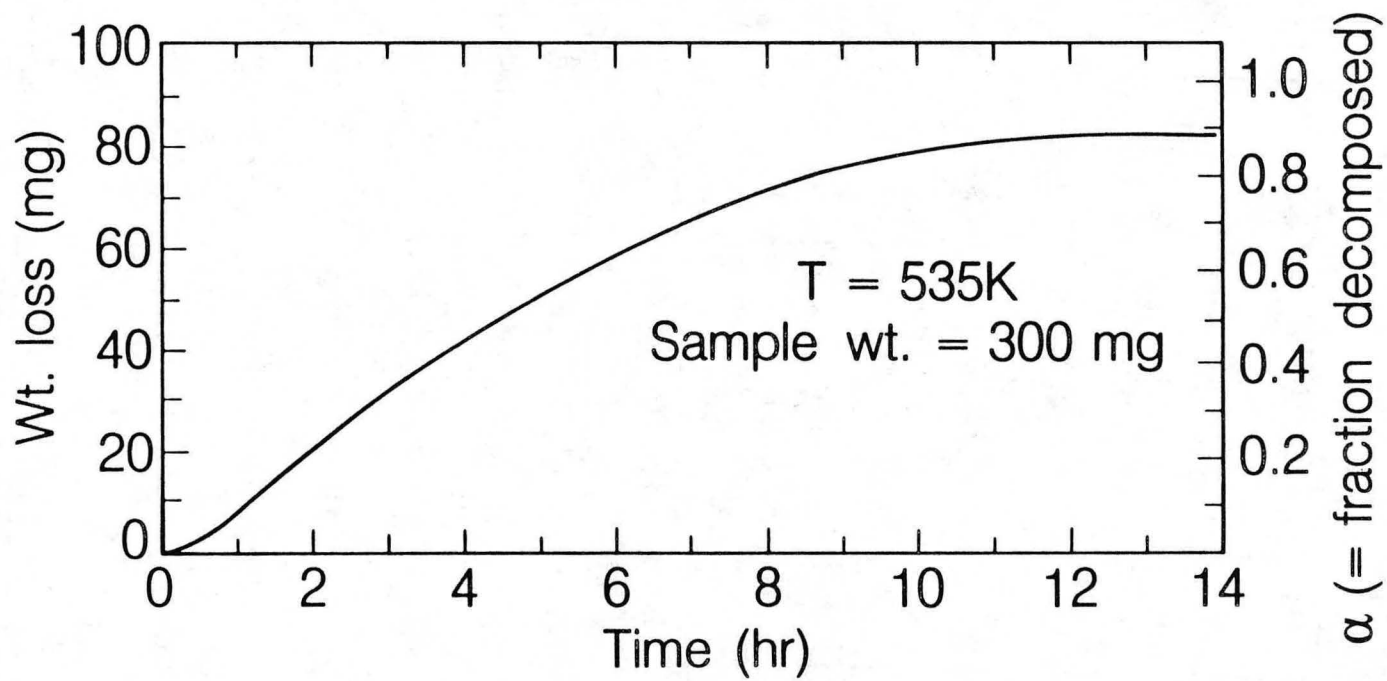
XBL 859 3838

Fig. 9



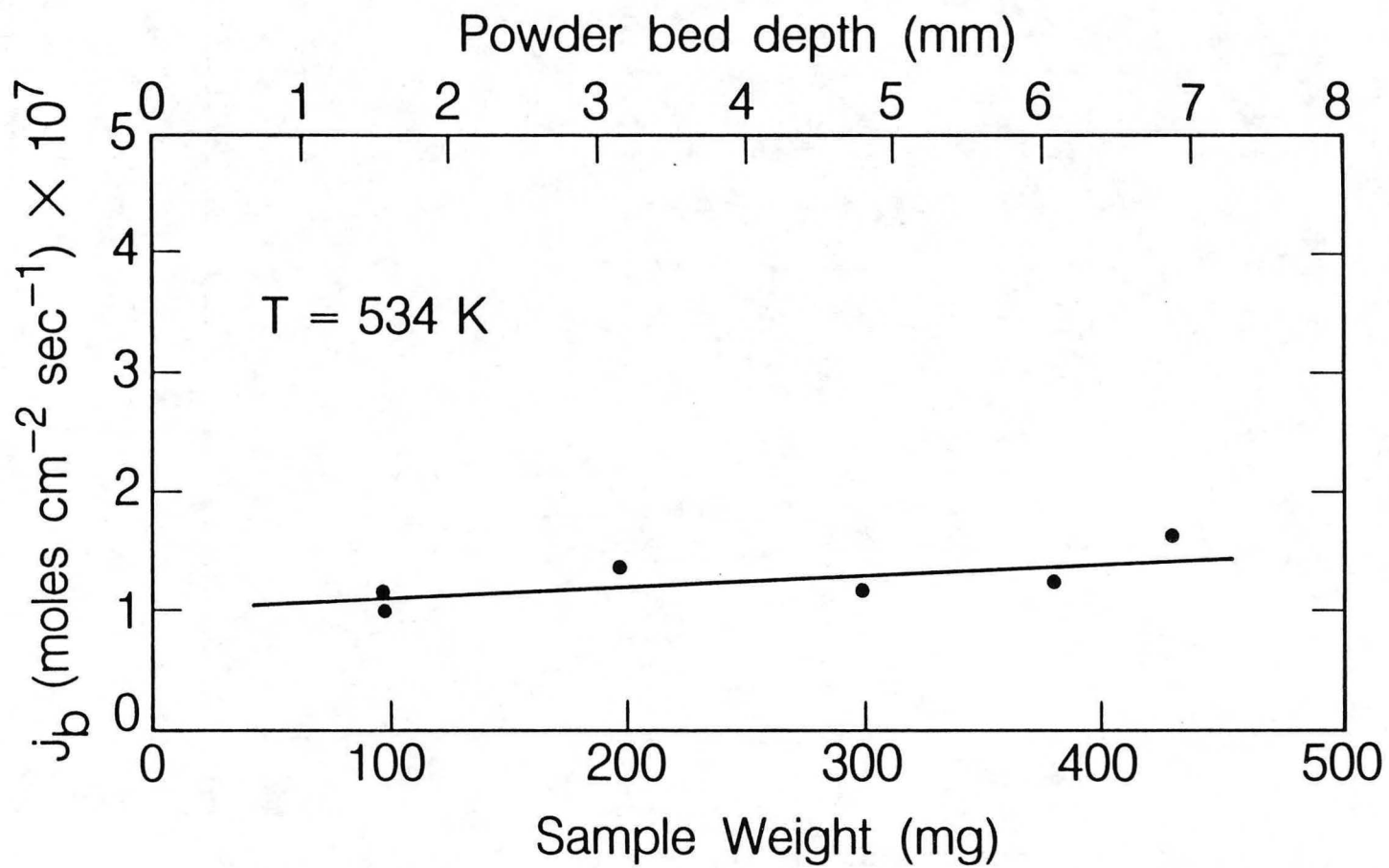
XBL 859-3847

Fig. 10



XBL 859-3846

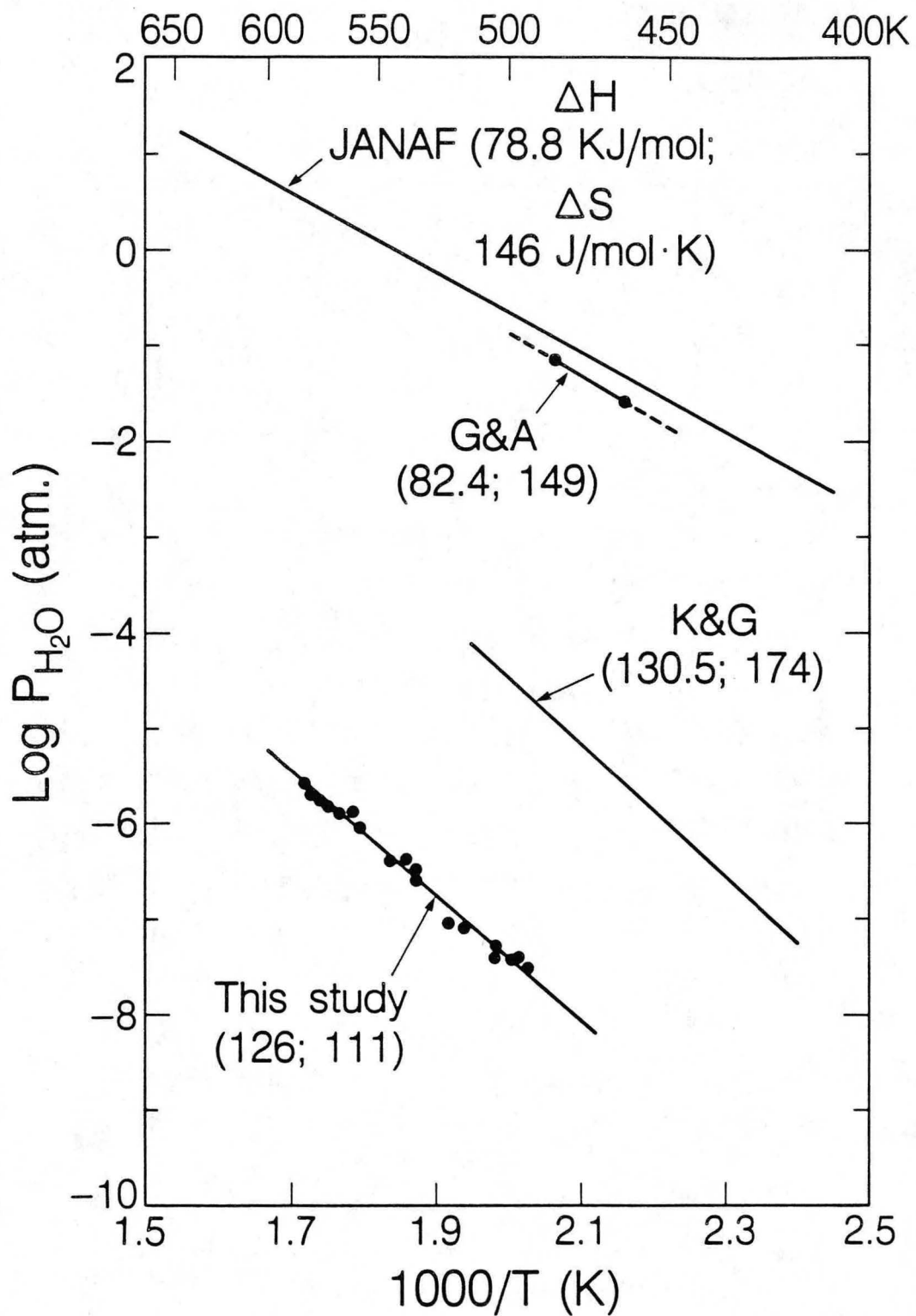
Fig. 11



-125-

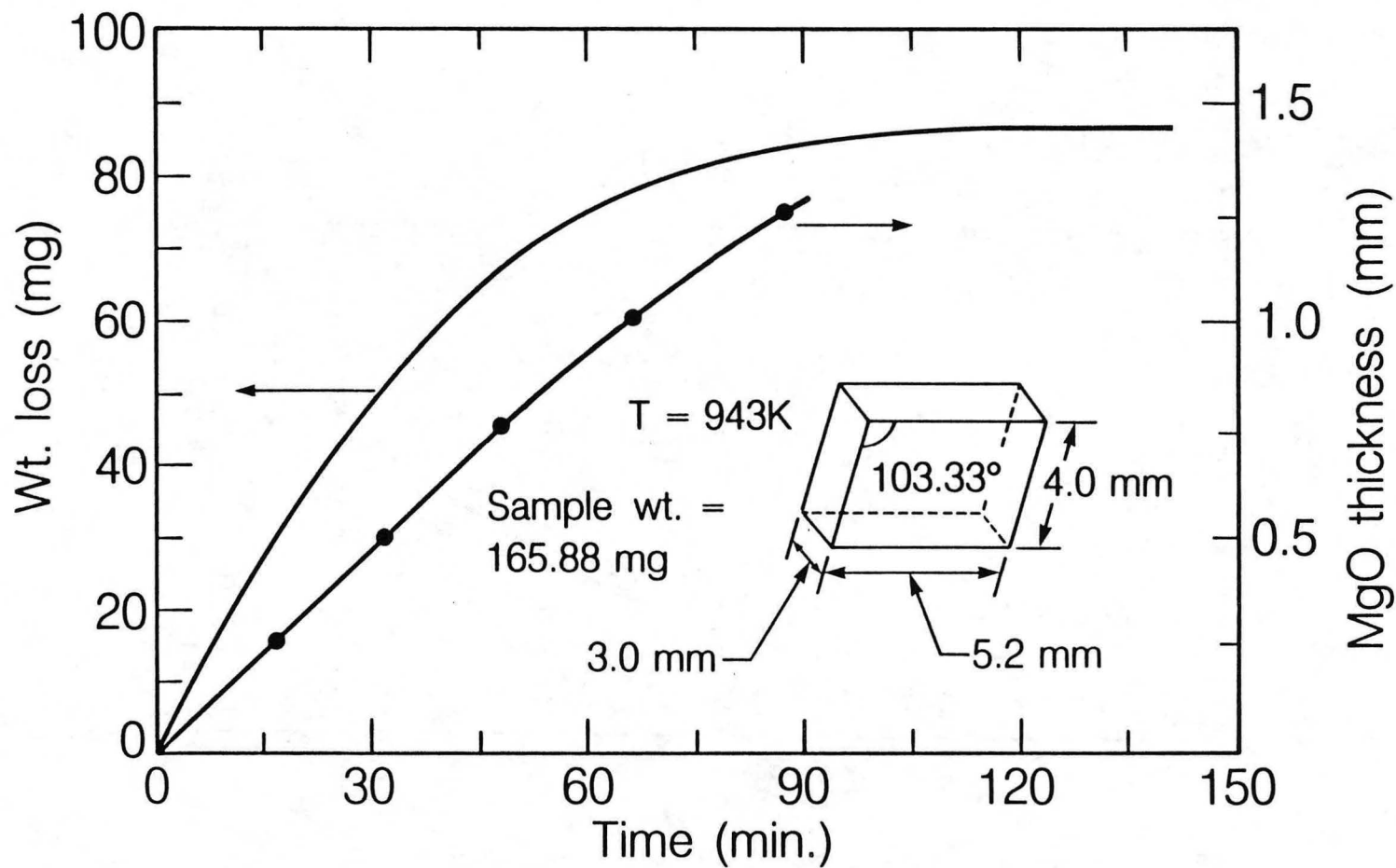
XBL 859-3836

Fig. 12



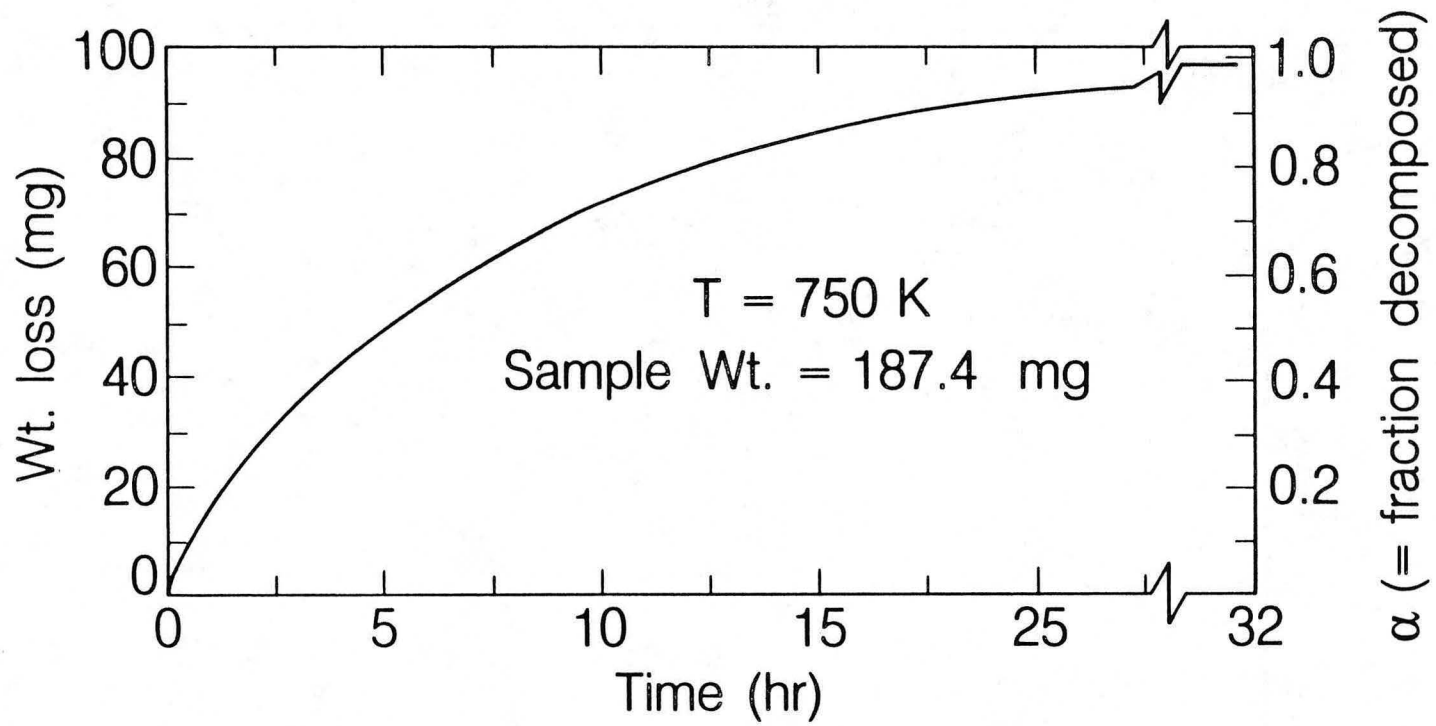
XBL 8410-8788

Fig. 13



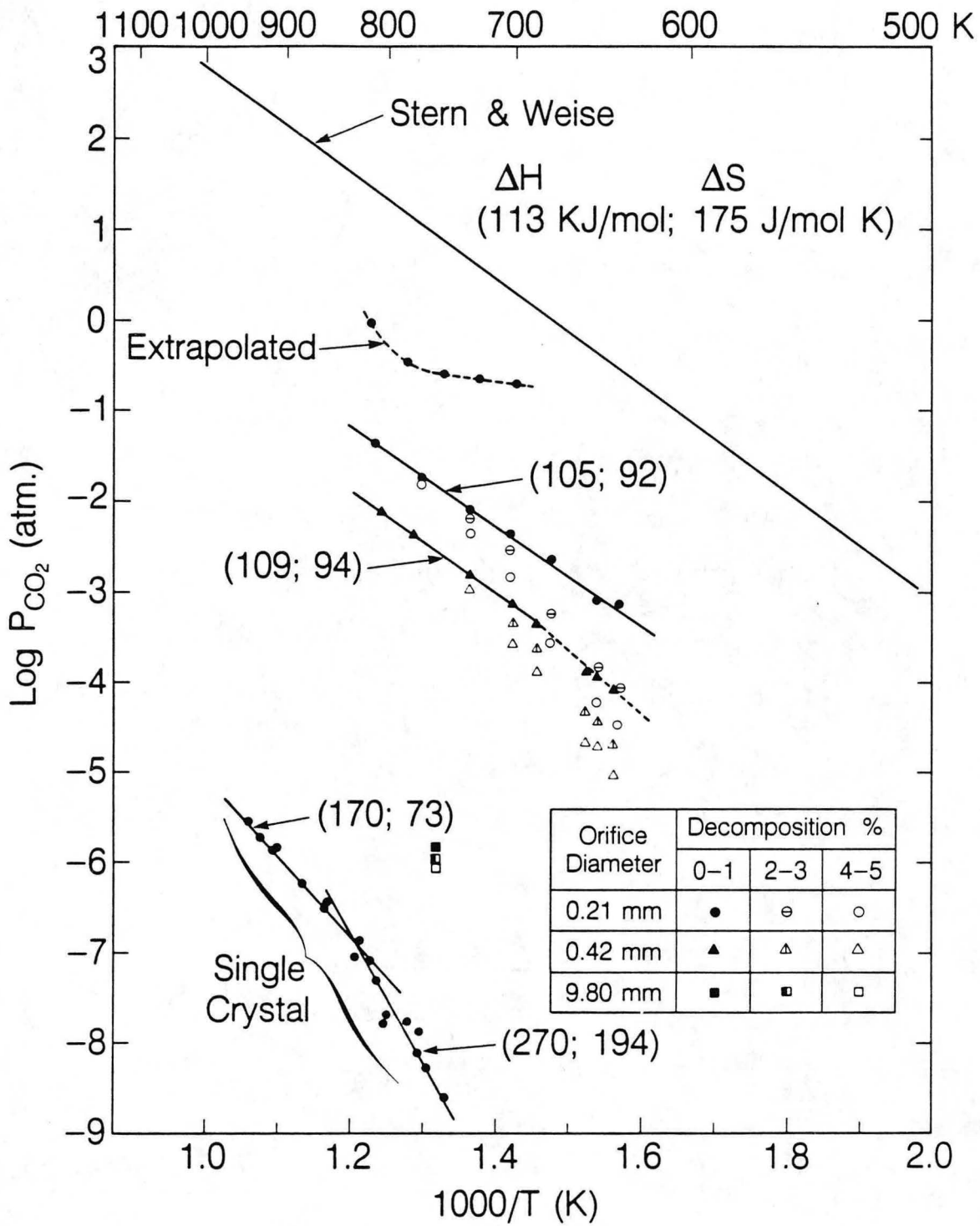
XBL 859-3843

Fig. 14



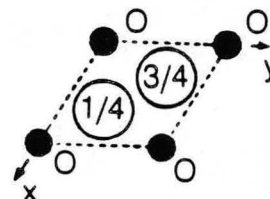
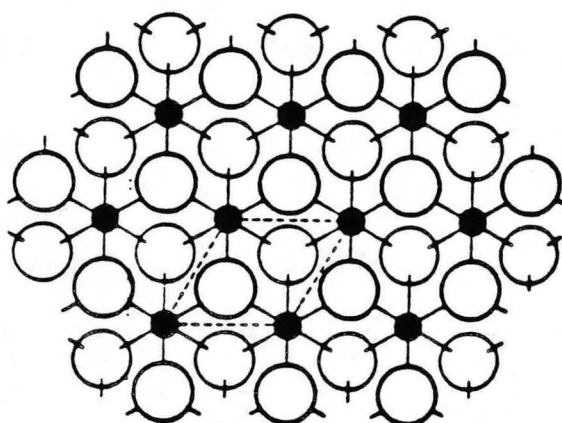
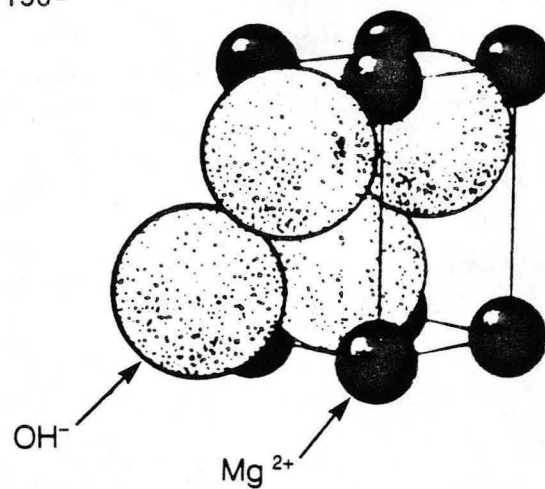
XBL 859-3849

Fig. 15



XBL 859-3839A

Fig. 16



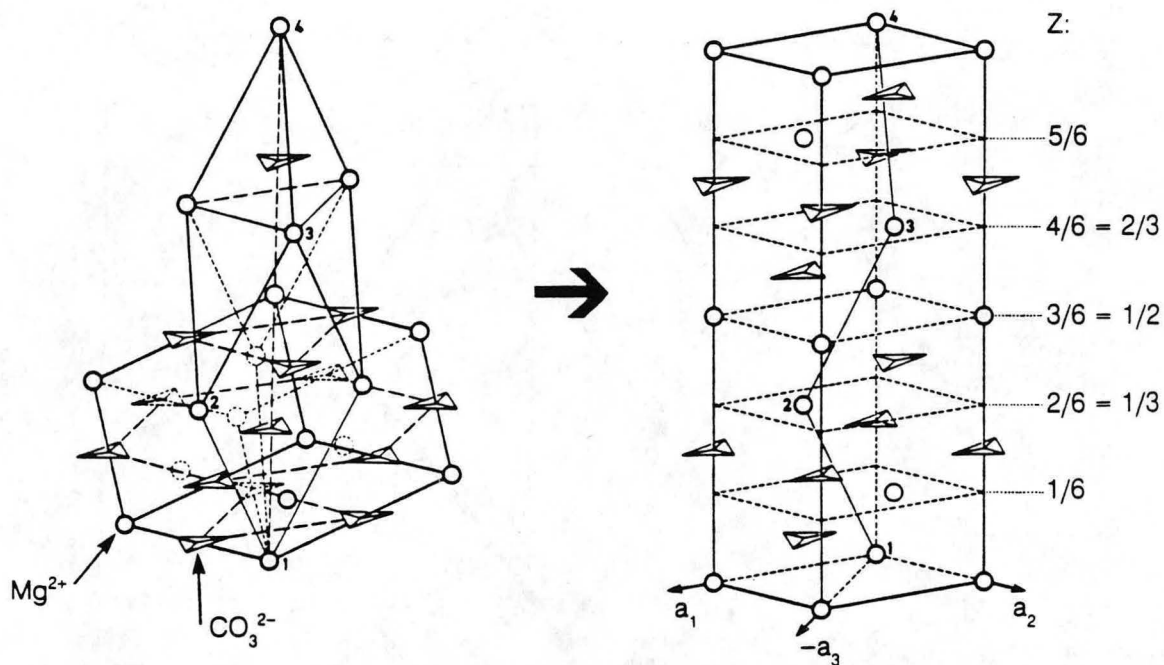
Hexagonal $\text{Mg}(\text{OH})_2$

$$a_o = 3.147 \text{ \AA}$$

$$c_o = 4.769 \text{ \AA}$$

XBL 854-2140

Fig. 17



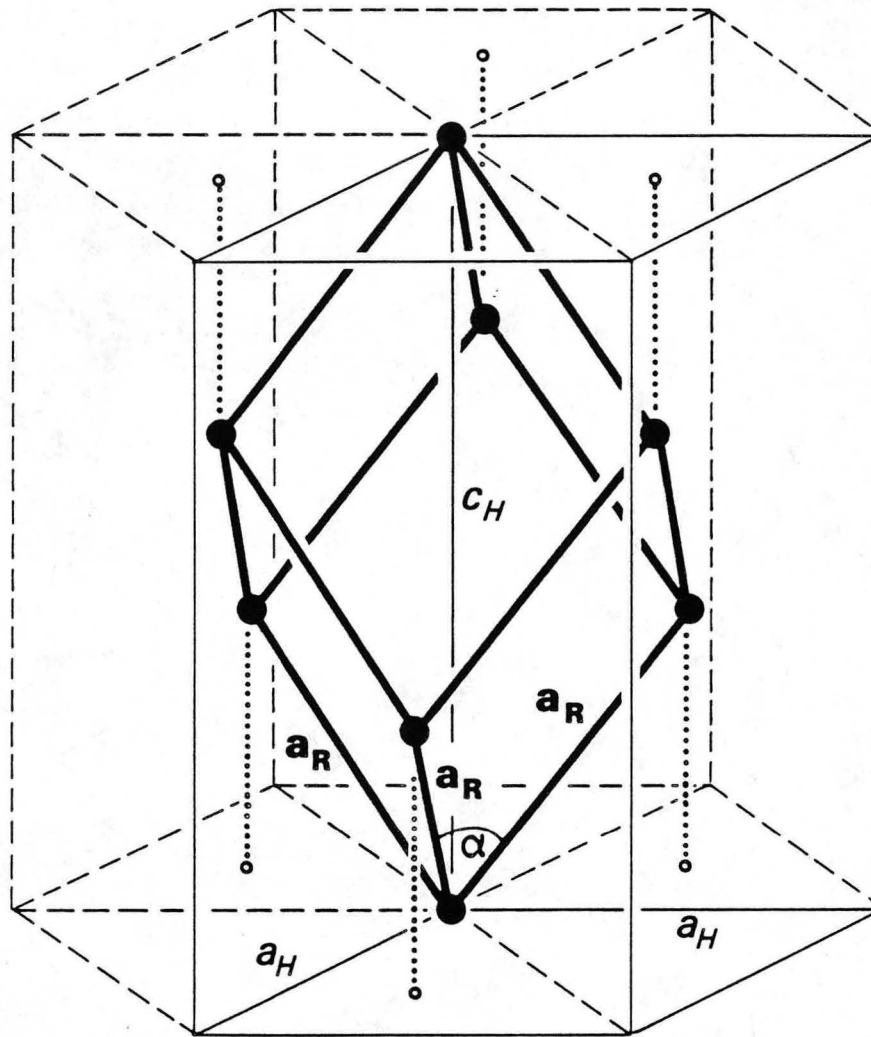
Hexagonal Mg CO₃

$a_o = 4.6332 \text{ \AA}$

$c_o = 15.015 \text{ \AA}$

XBL 854-2135

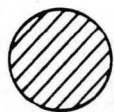
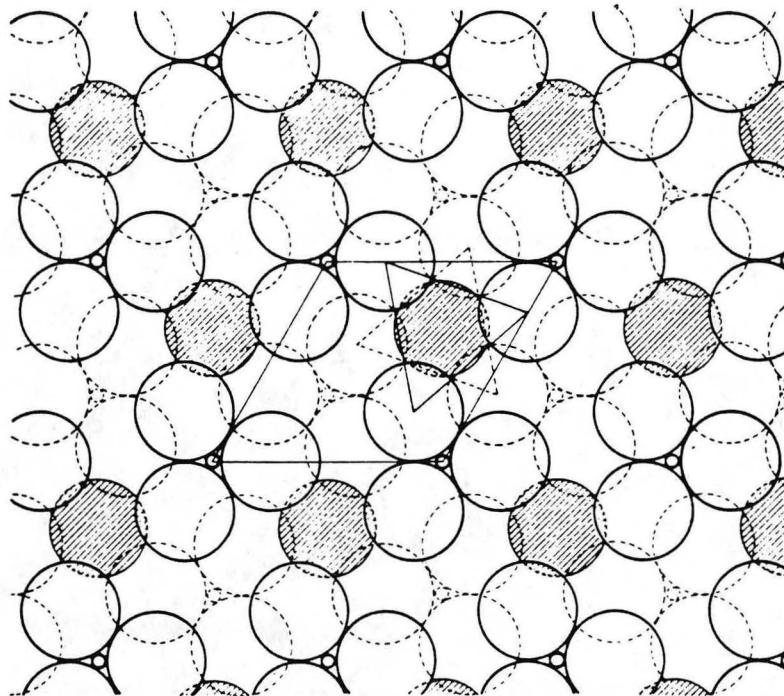
Fig. 18



TRANSFORMATION BETWEEN RHOMBOHEDRAL (a_R, α)
AND HEXAGONAL (a_H, c_H) CELLS

XBL 8011-2355

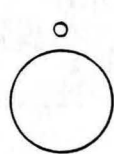
Fig. 19



M ion at $Z = 2/12$



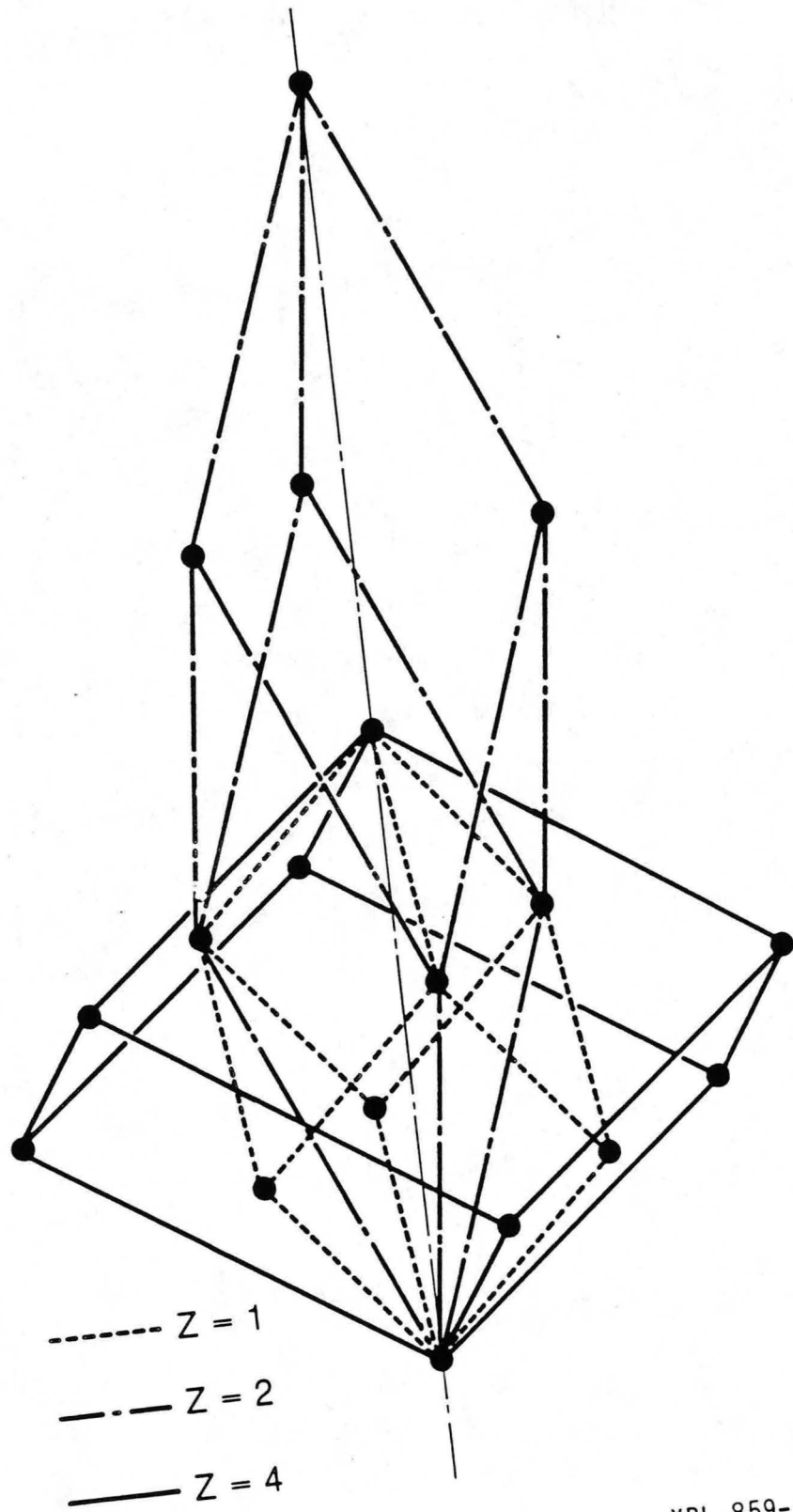
C }
O } at $Z = 1/12$



C }
O } at $Z = 3/12$

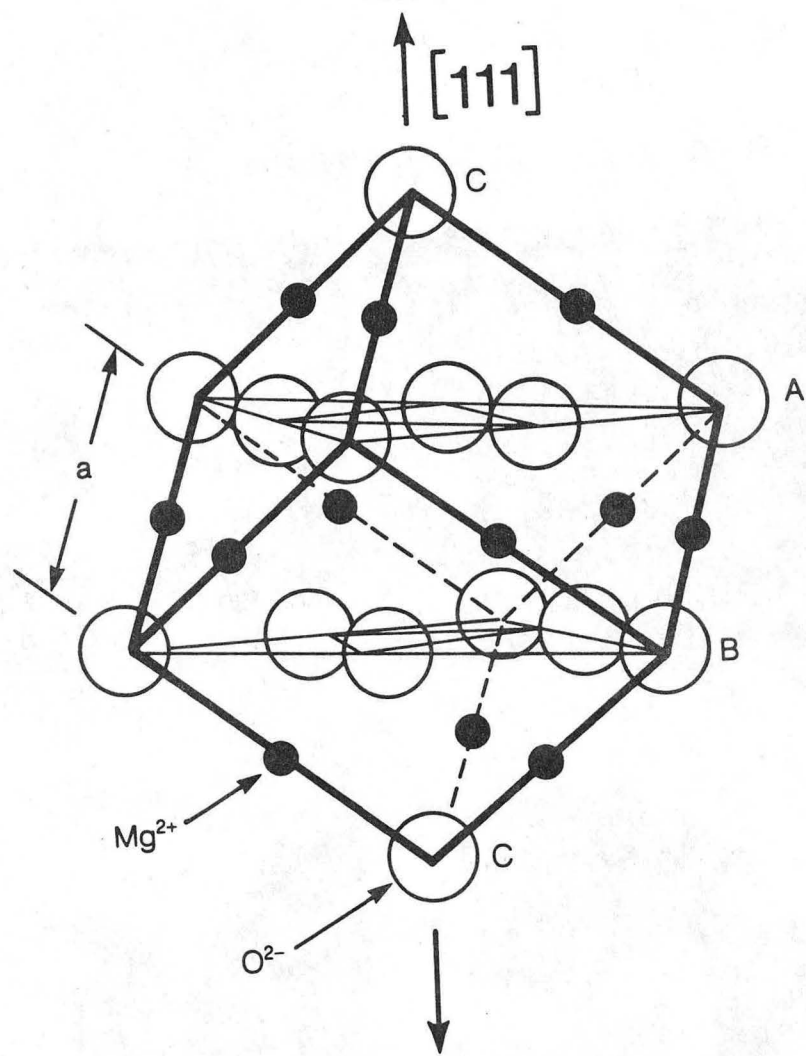
XBL 859-3848

Fig. 20



XBL 859-3844

Fig. 21

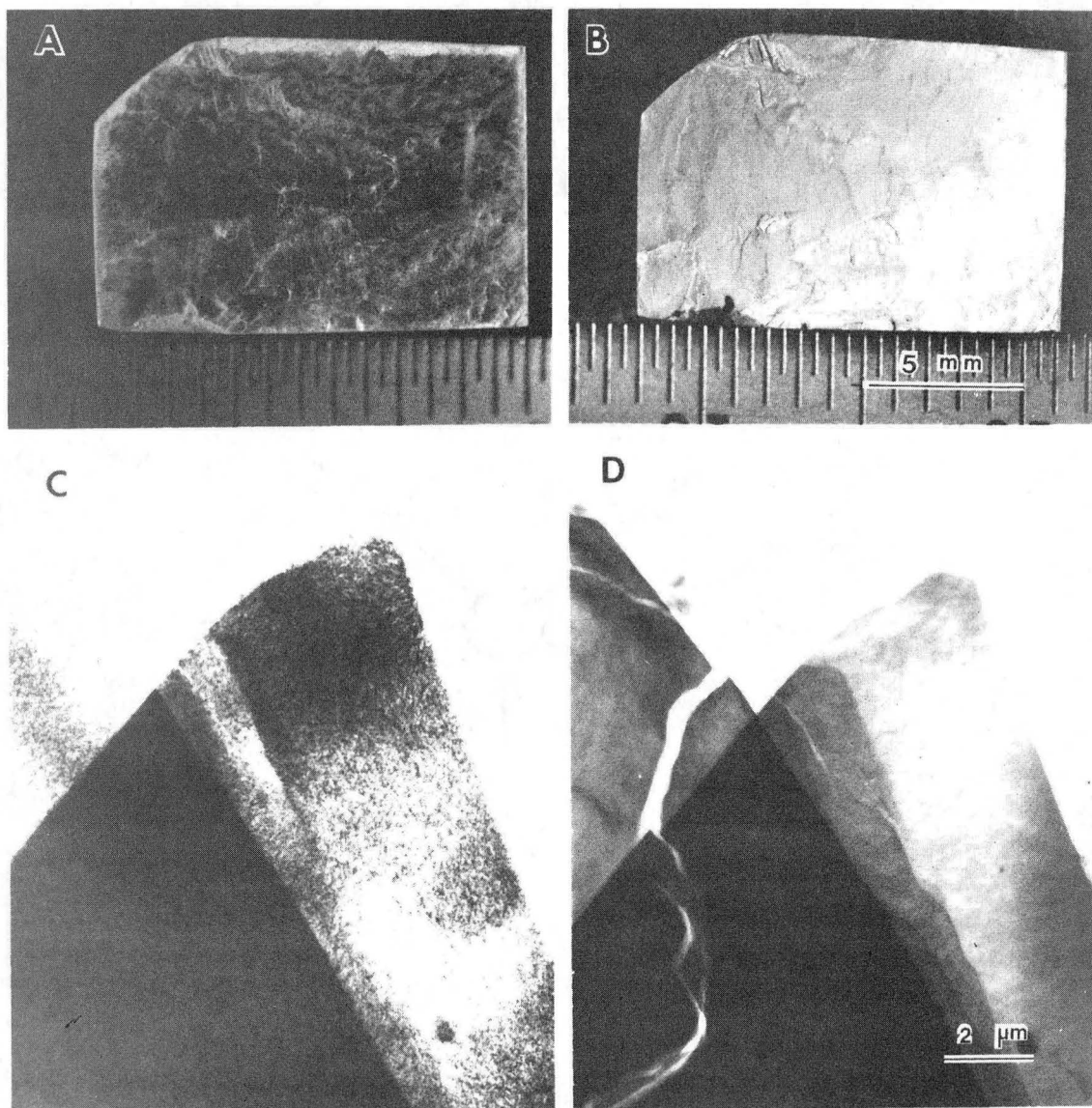


FCC MgO

 $a_o = 4.213\text{\AA}$

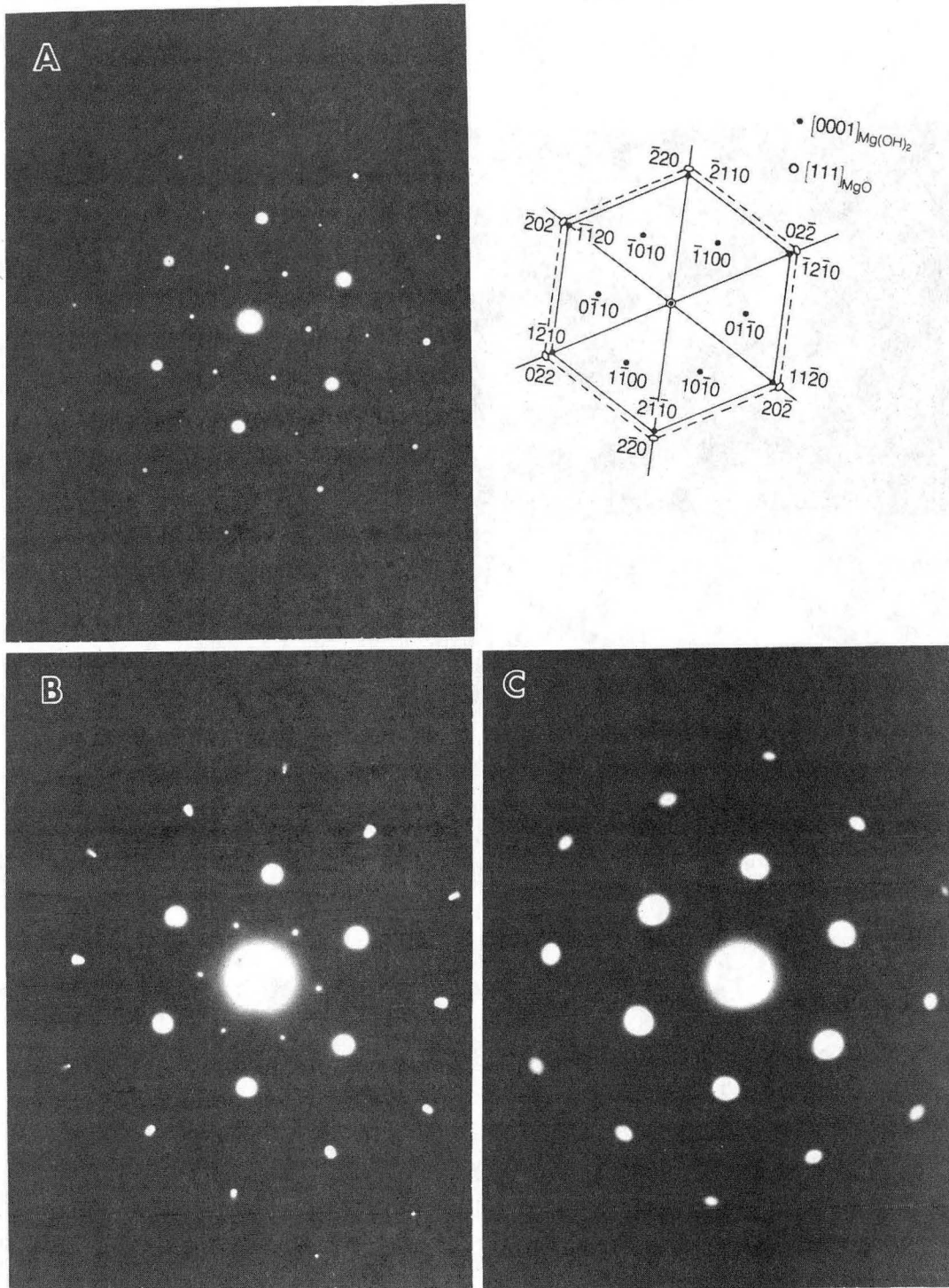
XBL 854-2136

Fig. 22



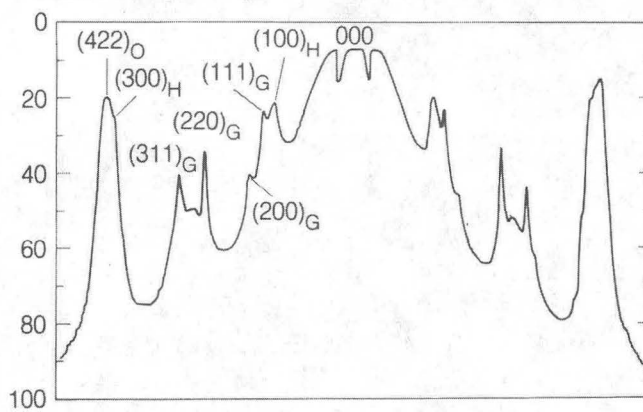
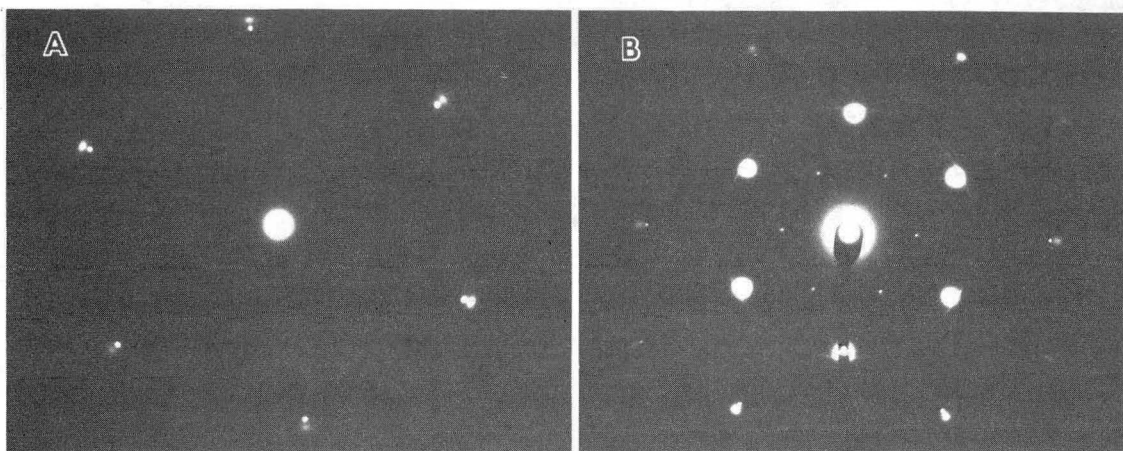
XBB 840-7414

Fig. 23



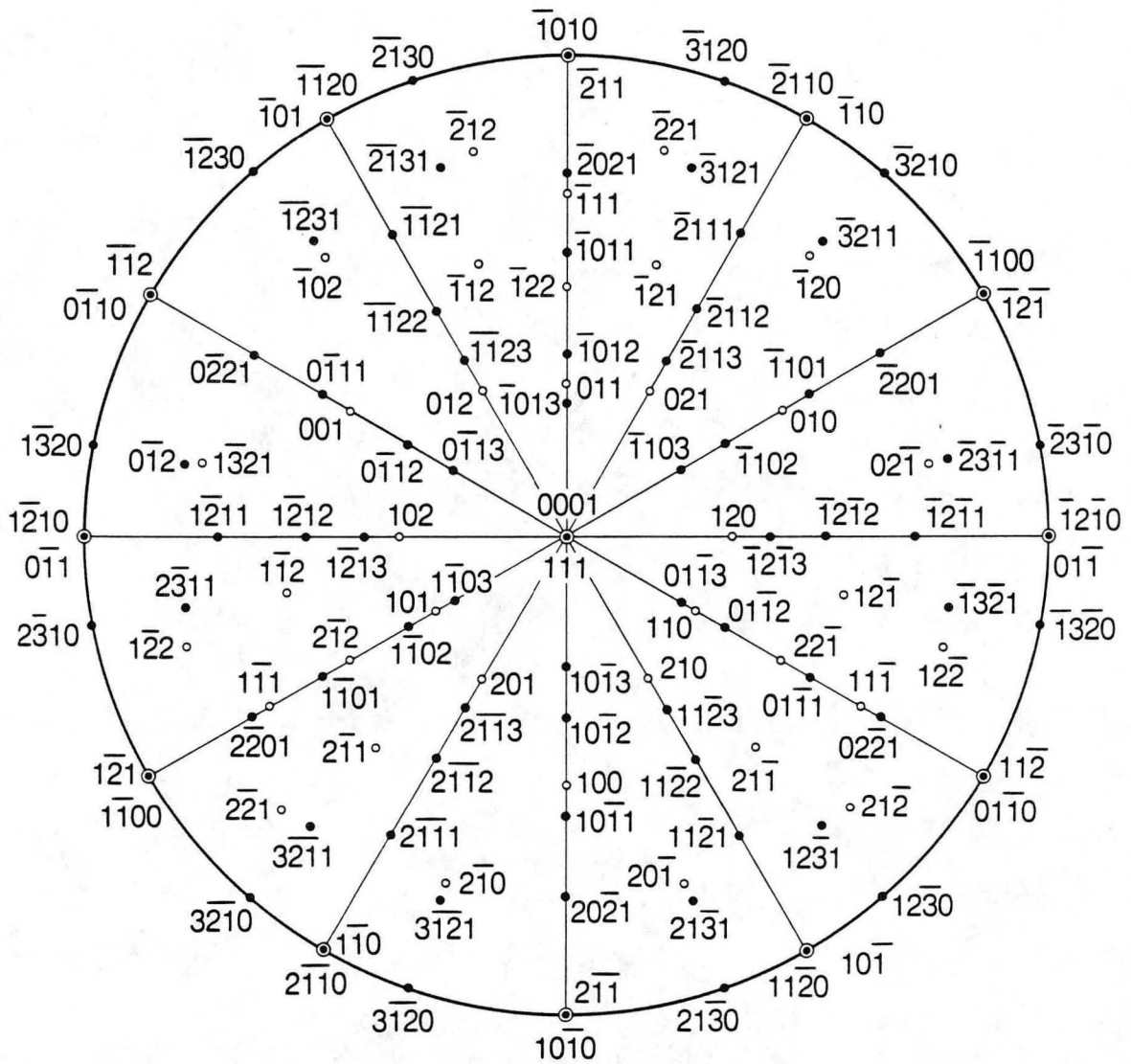
XBB 840-7417

Fig. 24



XBB 840-7415

Fig. 25

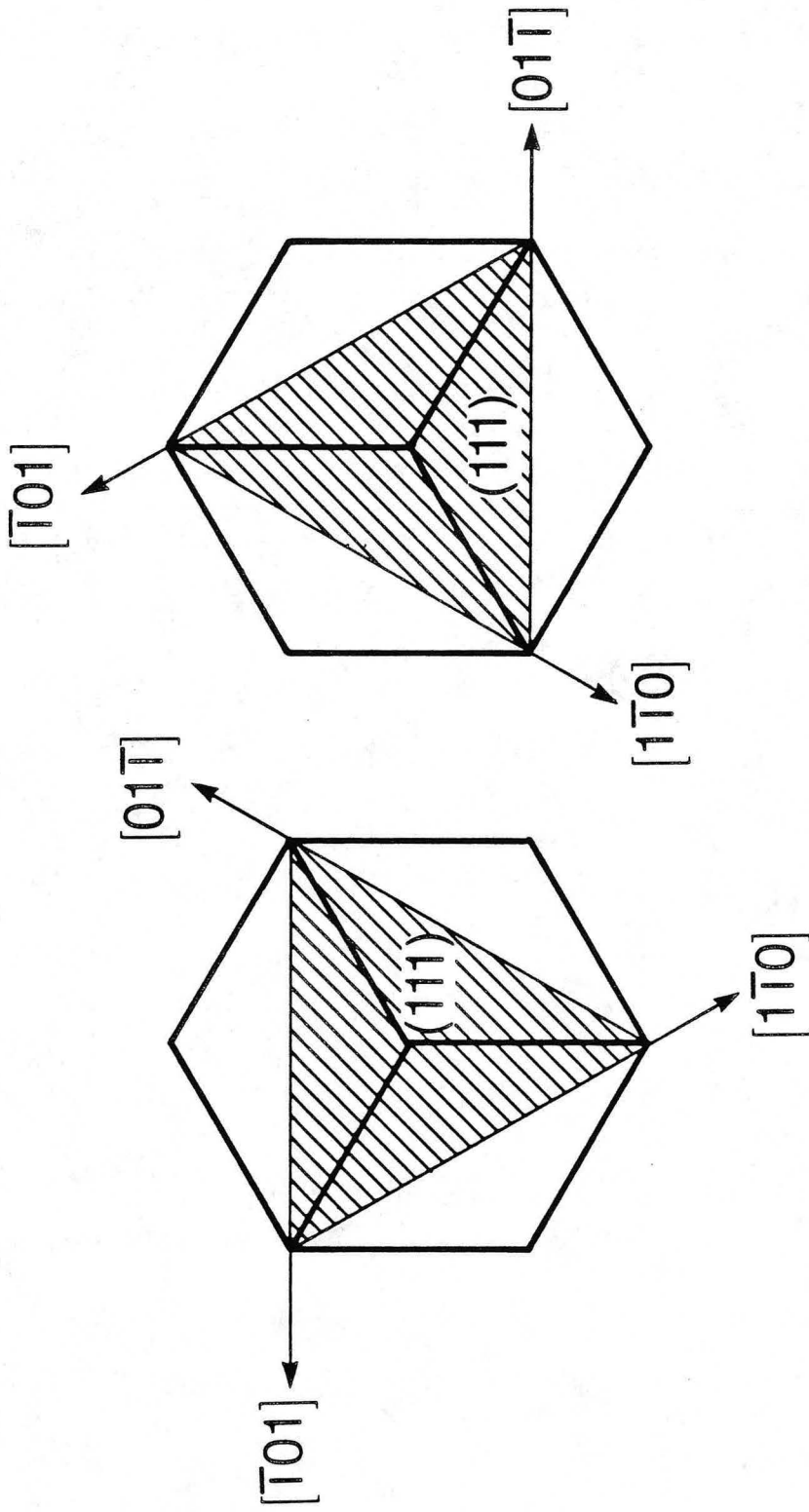


Mg(OH)₂ (0001) // MgO (111)

Mg(OH)₂ [11 $\bar{2}$ 0] // MgO [10 $\bar{1}$]

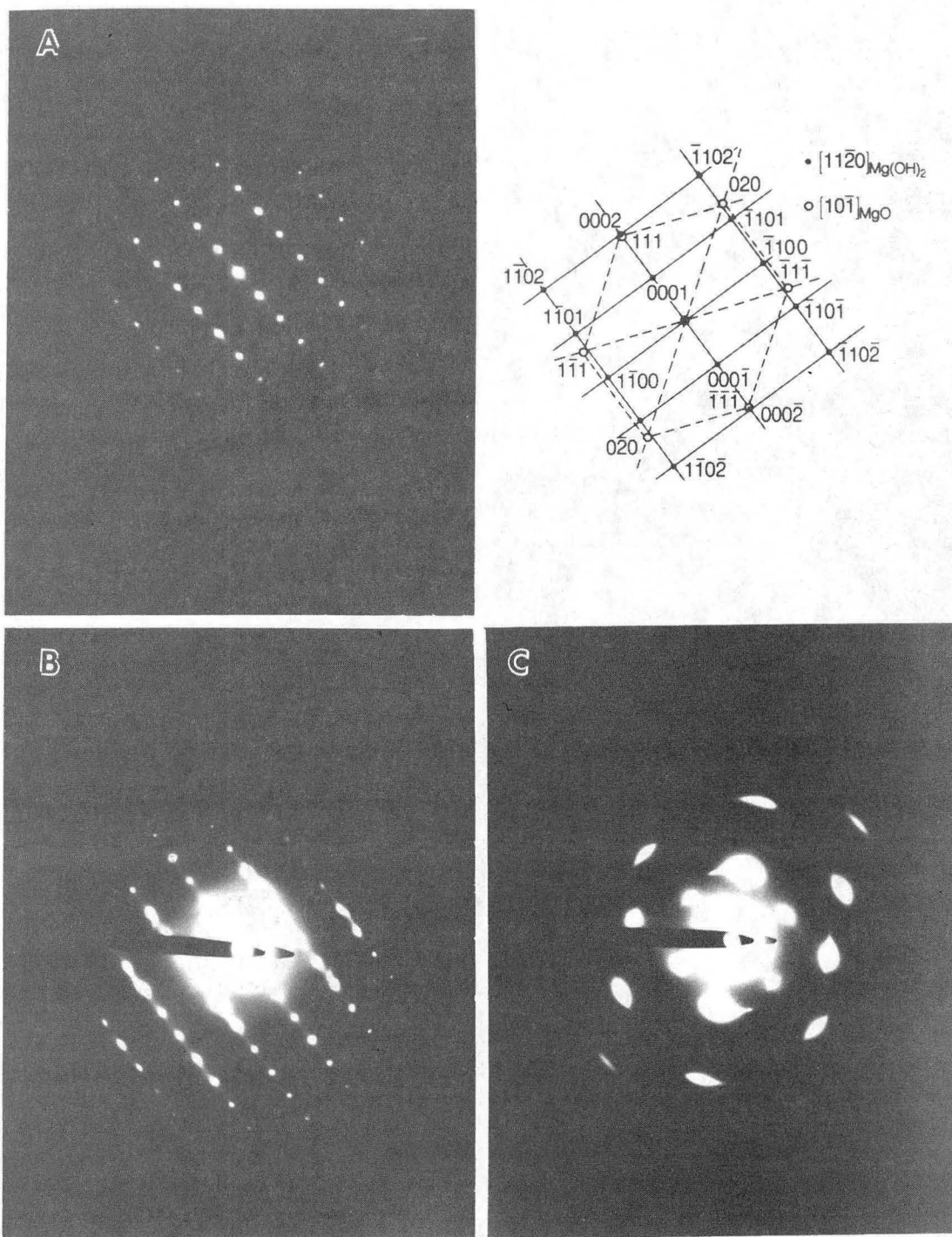
XBL 8410-8782

Fig. 26



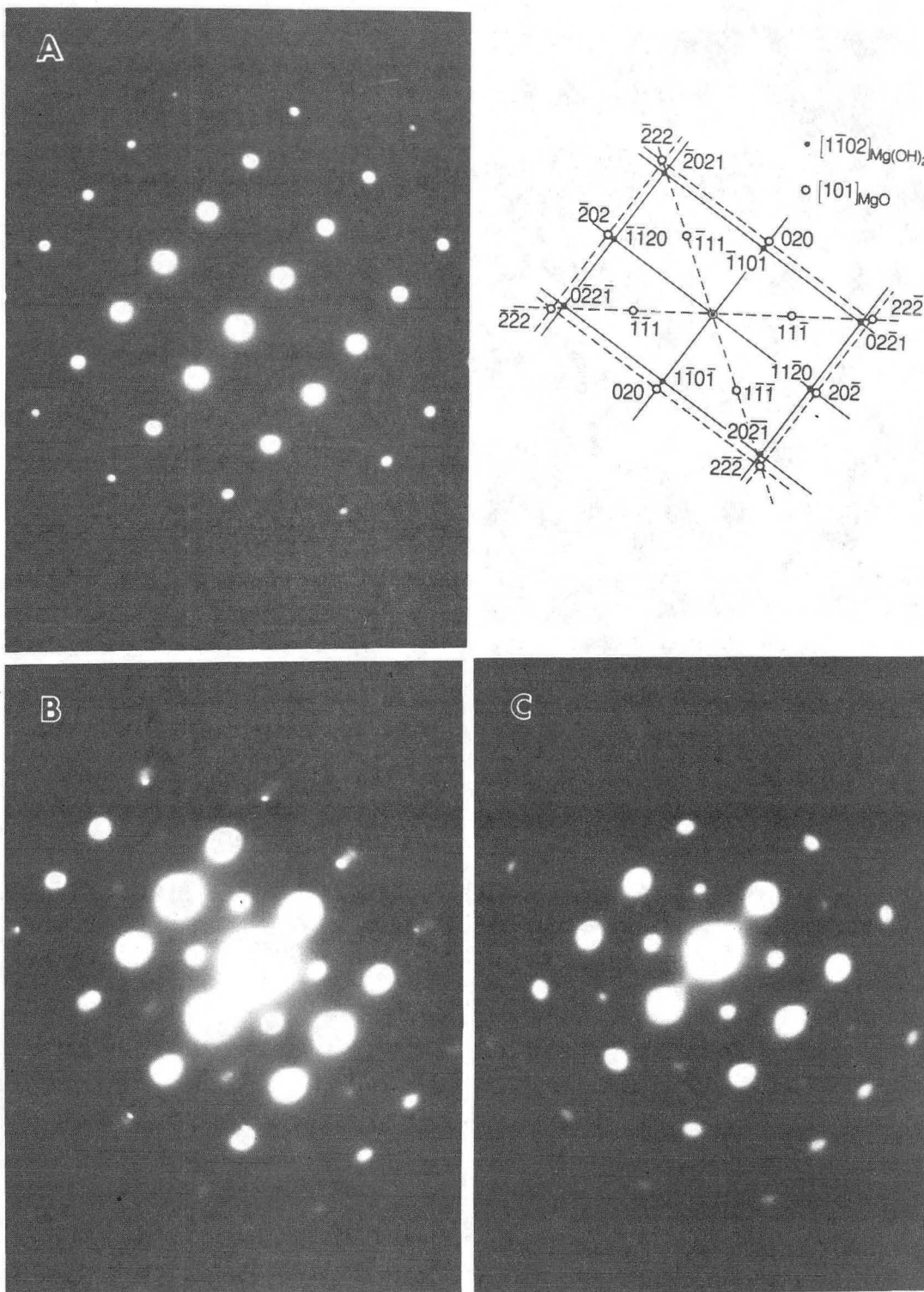
XBL 859-3845

Fig. 27



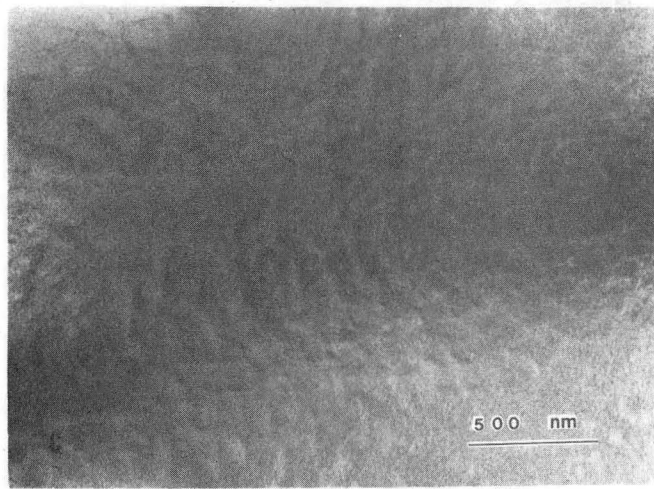
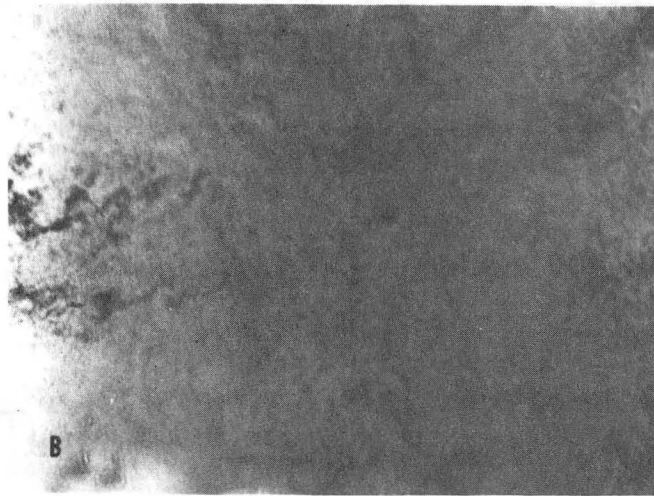
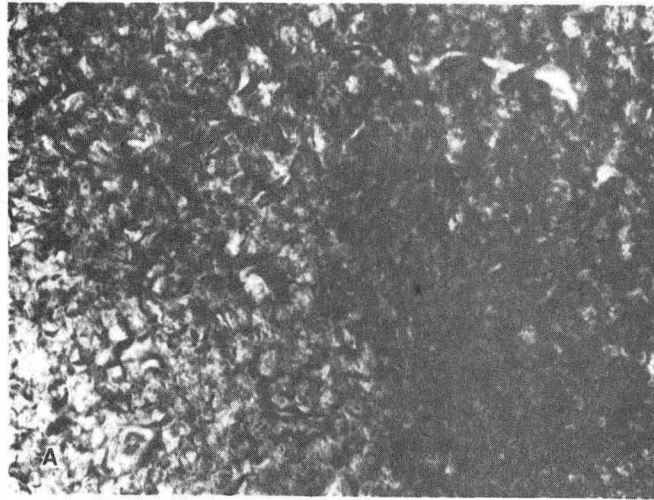
XBB 840-7416

Fig. 28



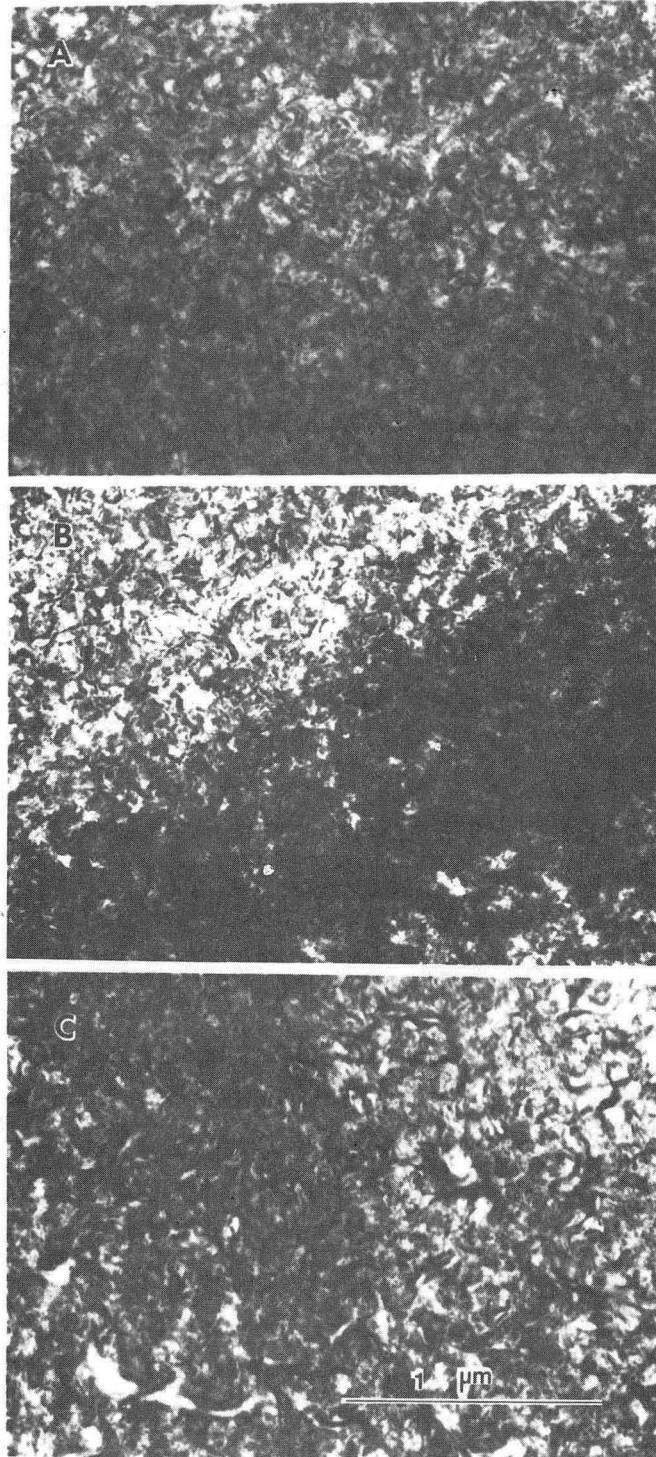
XBB 840-7420

Fig. 29



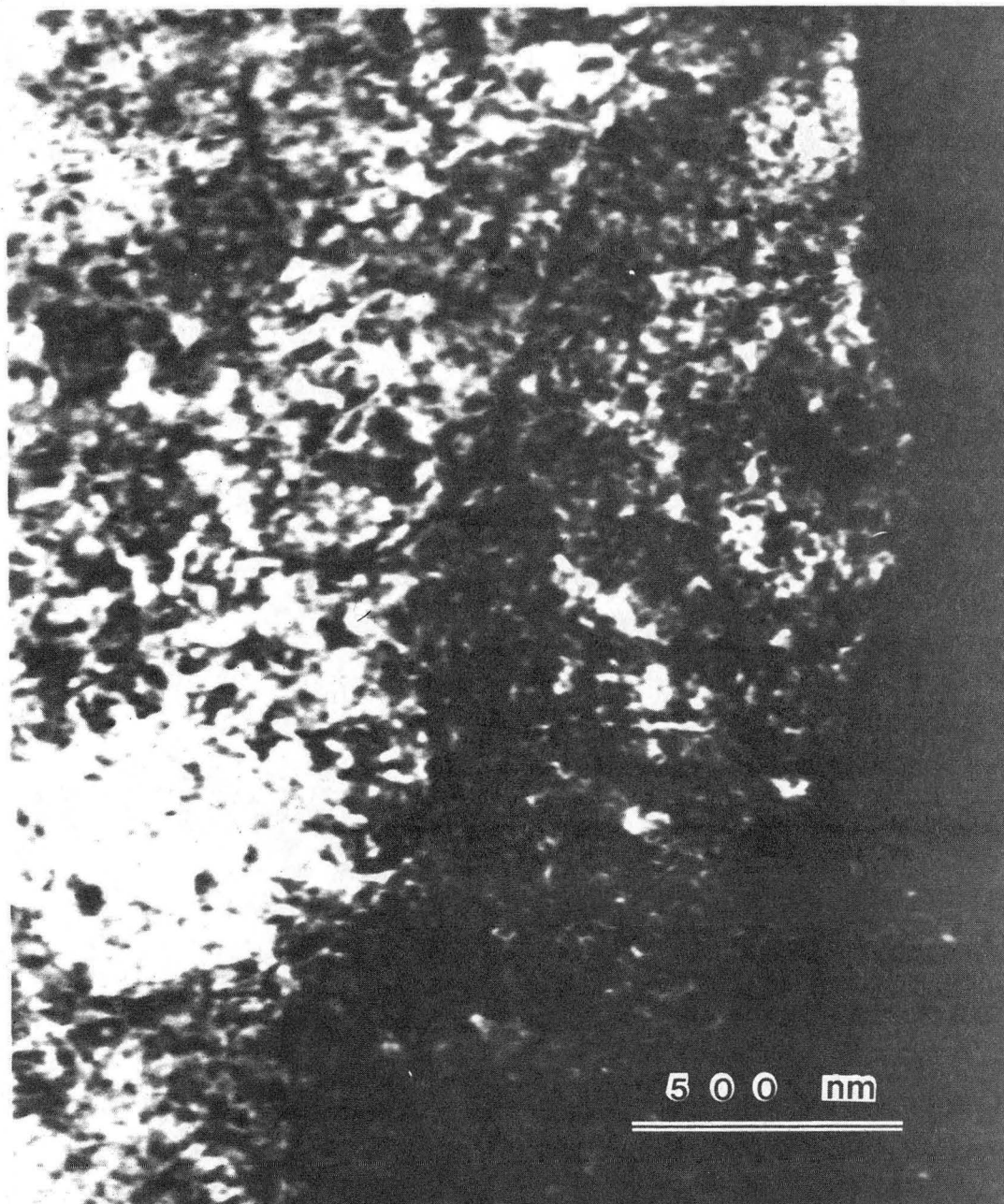
XBB 840-7413

Fig. 30



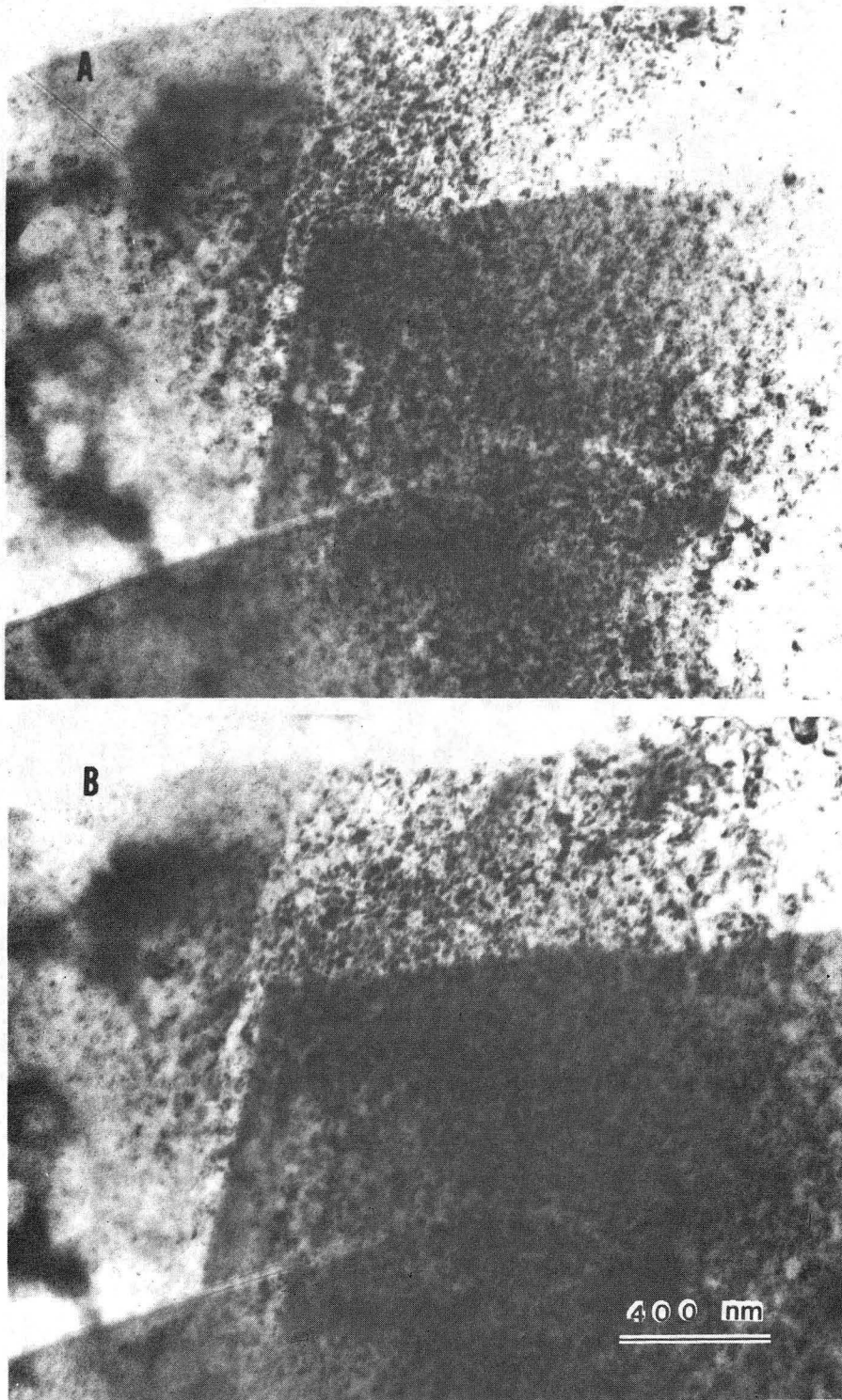
XBB 840-7427

Fig. 31



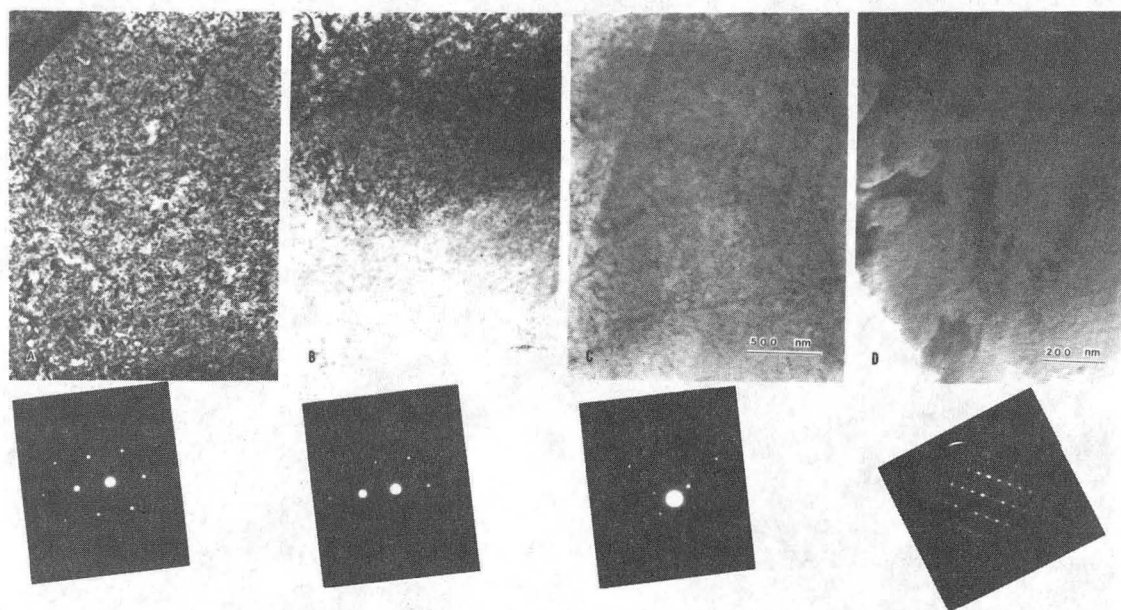
XBB 840-7421

Fig. 32



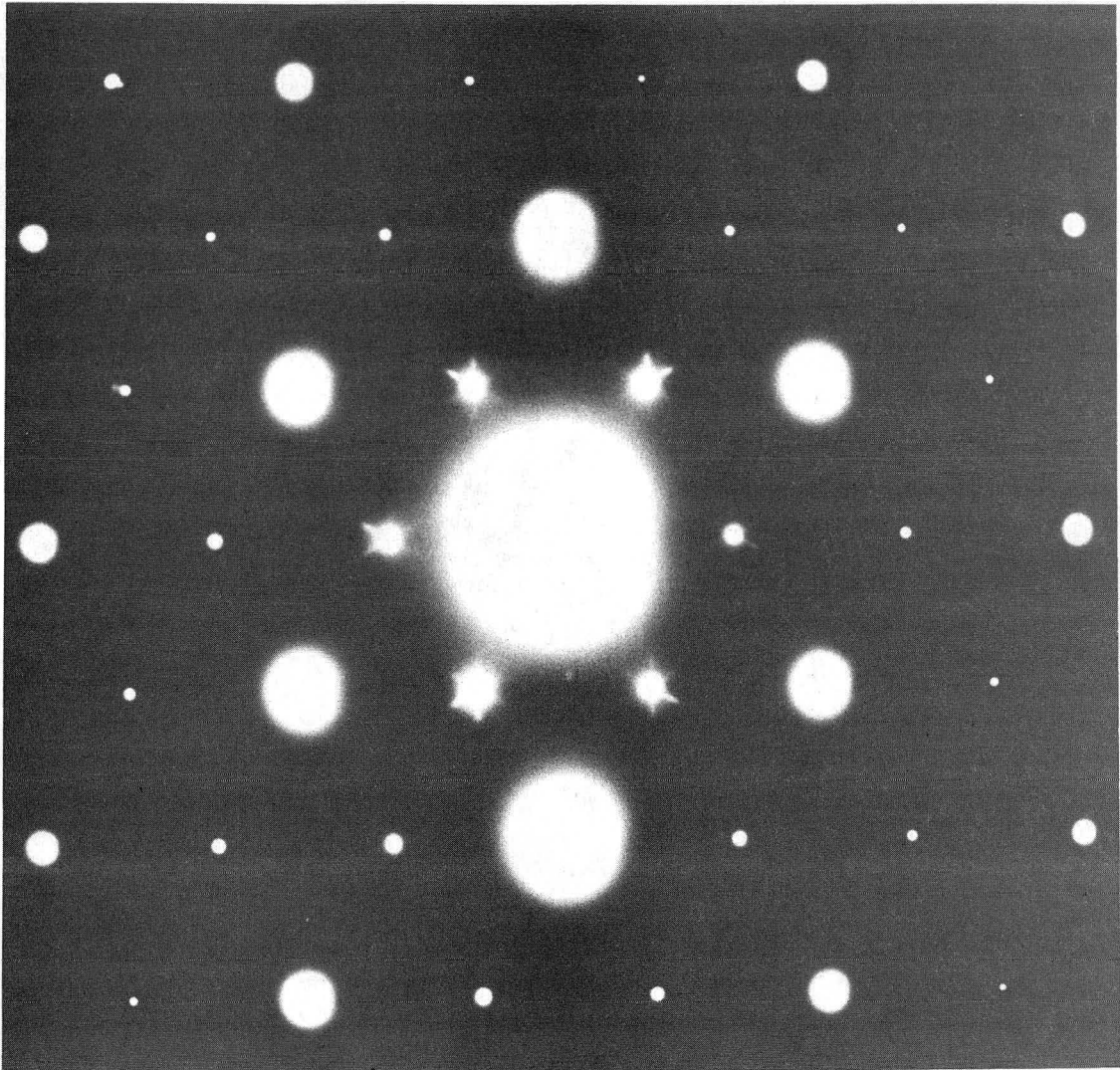
XBB 840-7422

Fig. 33



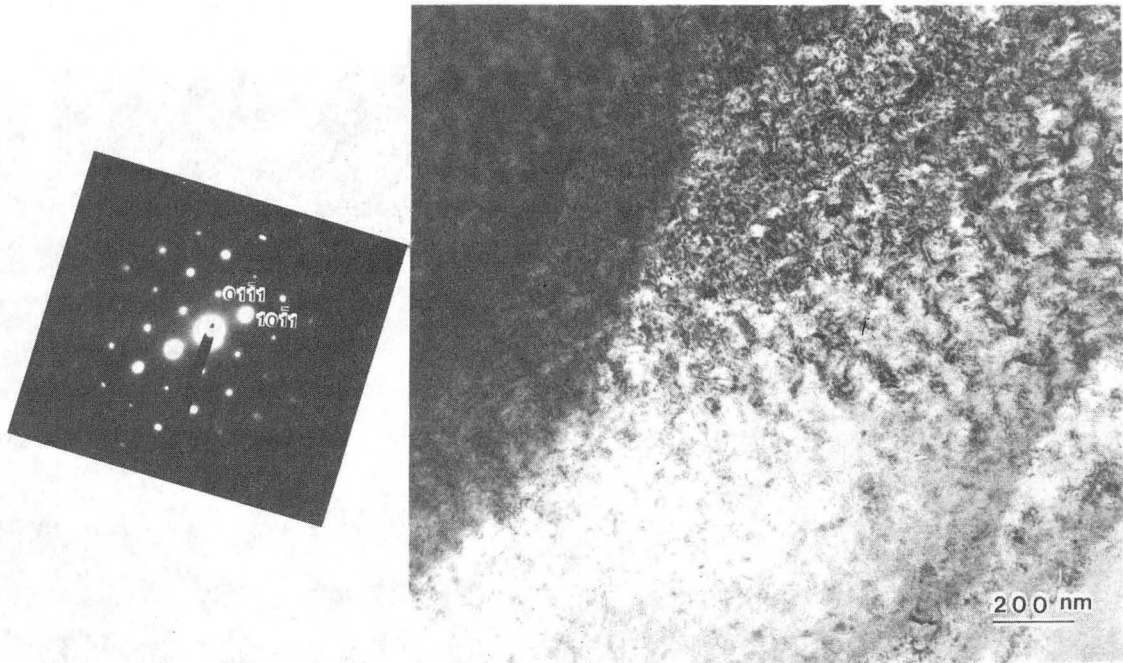
XBB 840-7430

Fig. 34



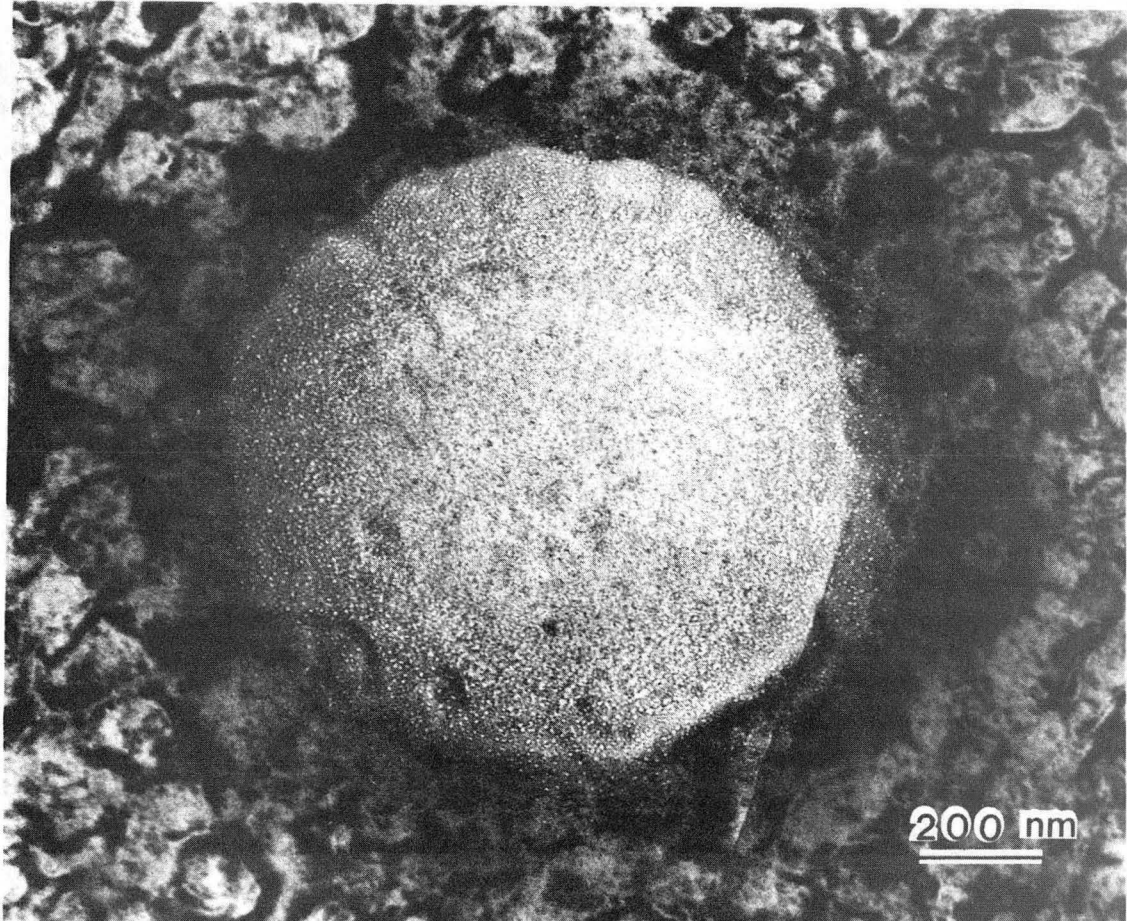
XBB 859-7043

Fig. 35



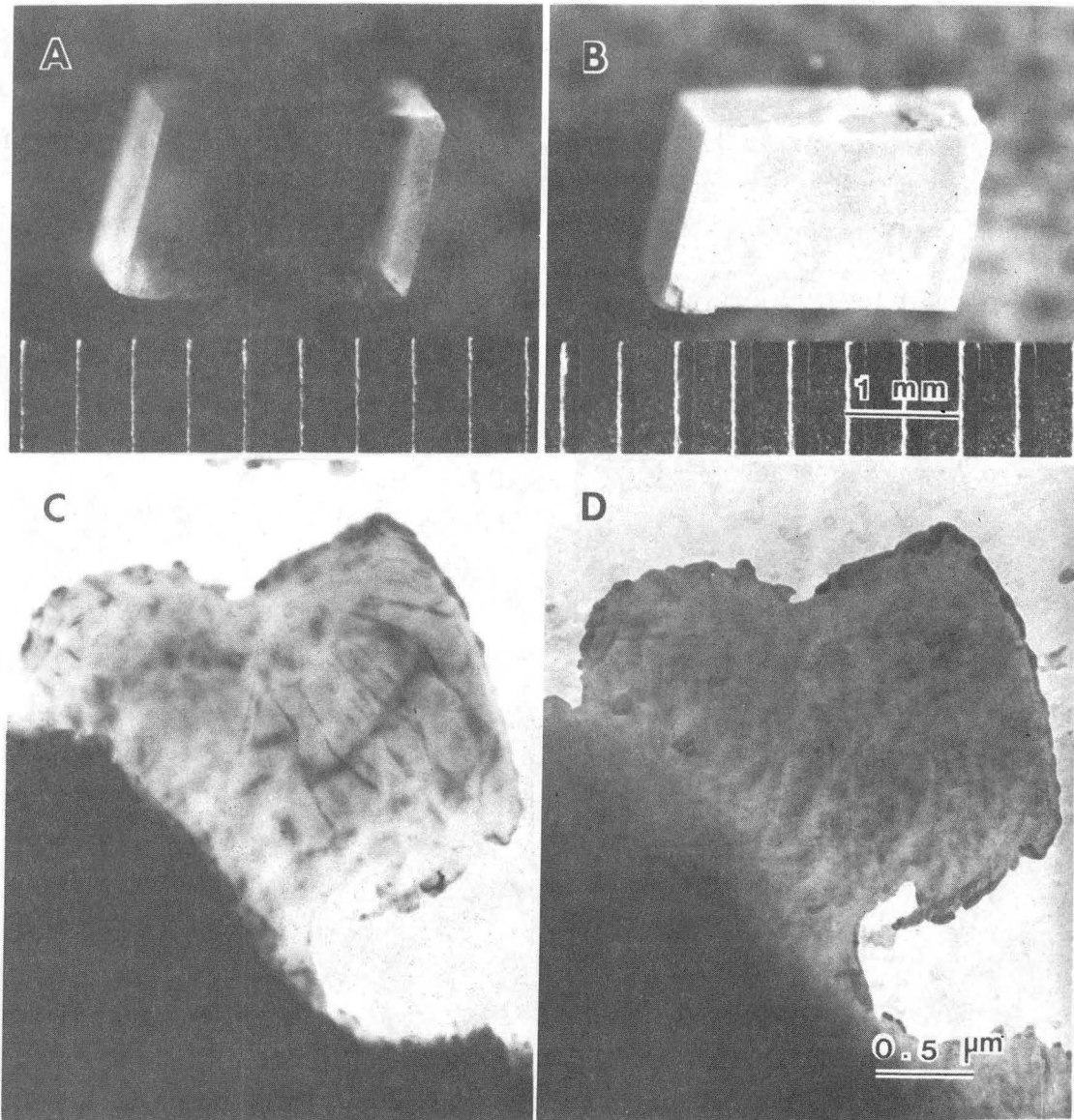
XBB 859-7045

Fig. 36



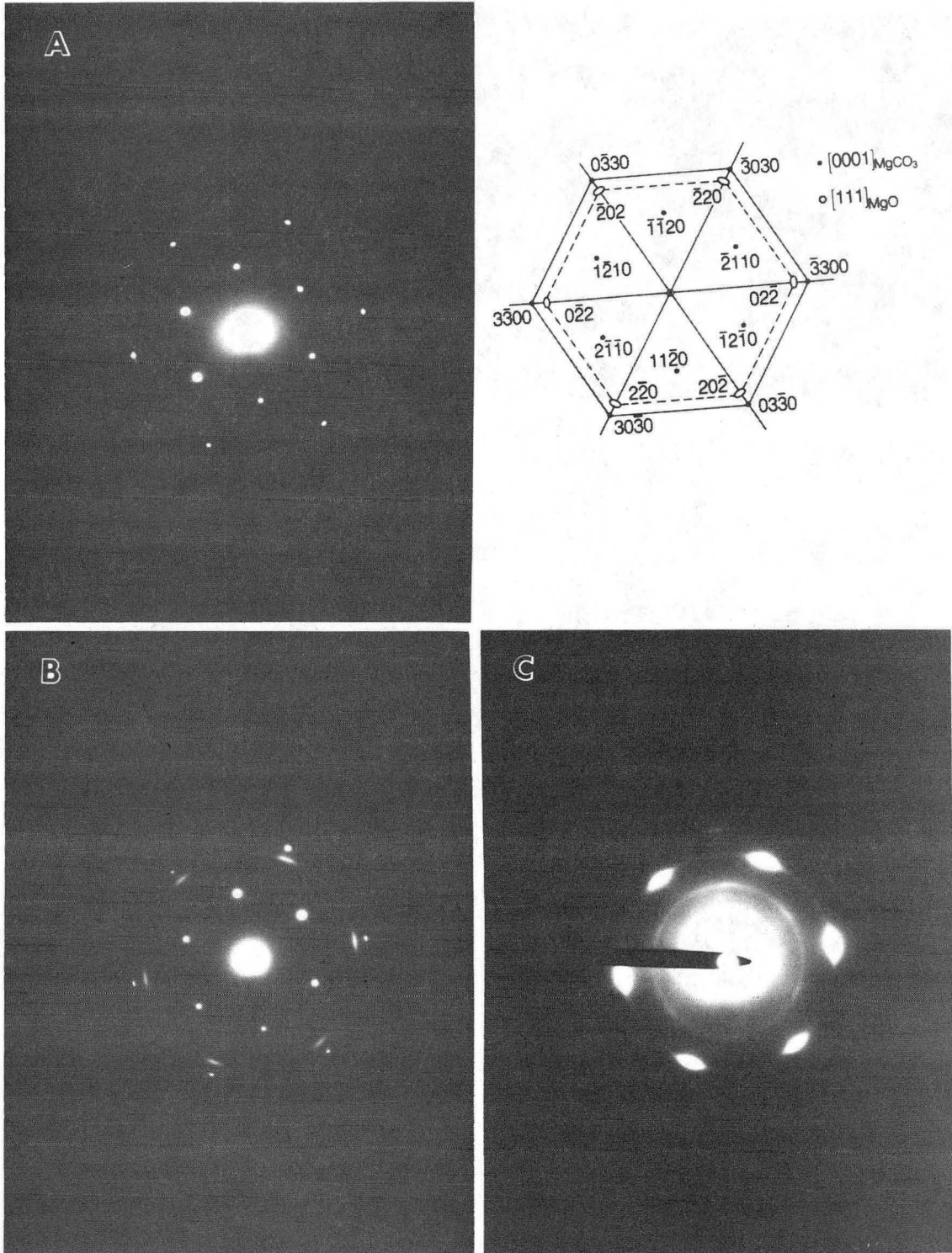
XBB 859-7042

Fig. 37



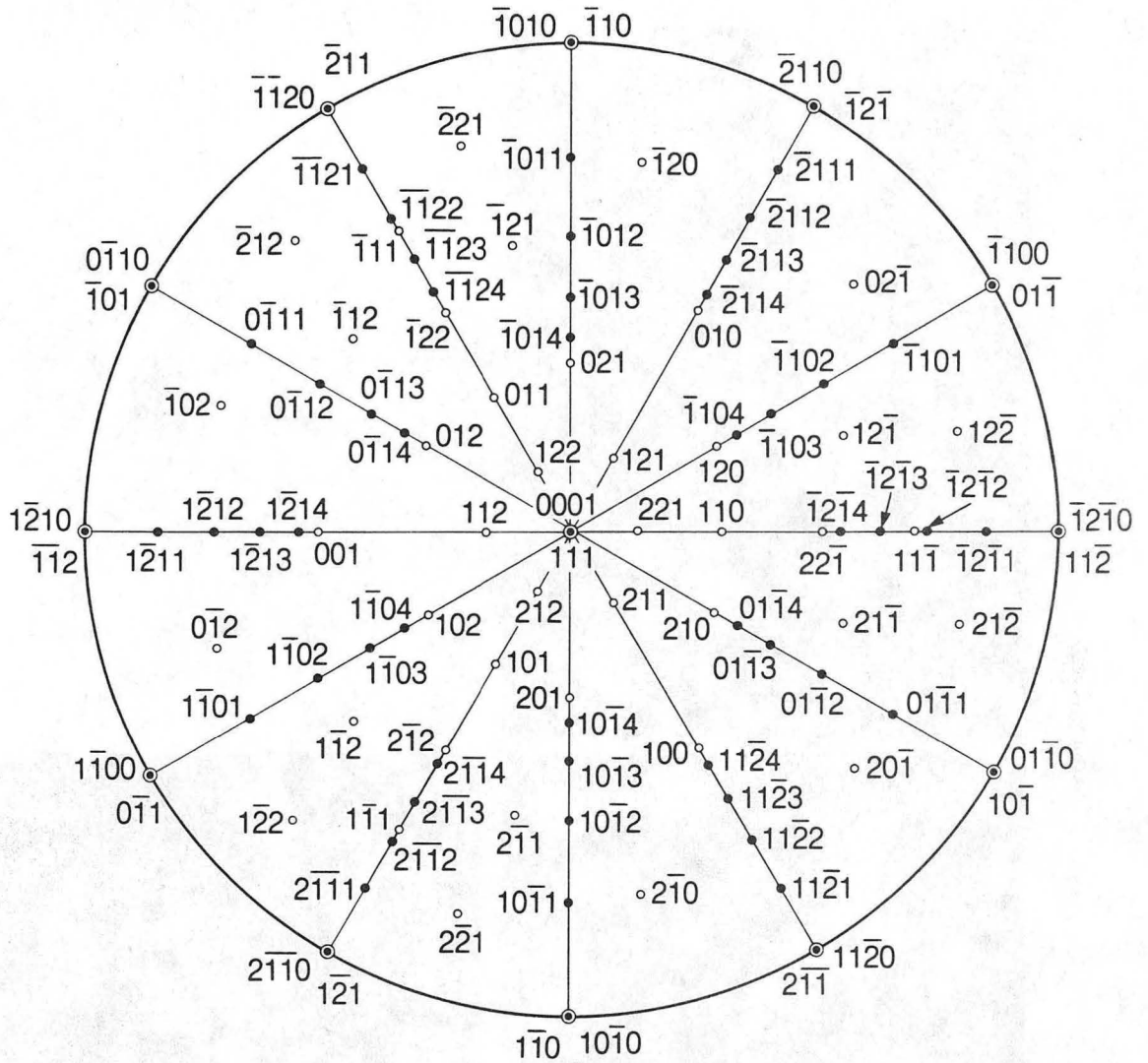
XBB 859-7048

Fig. 38



XBB 840-7419

Fig. 39

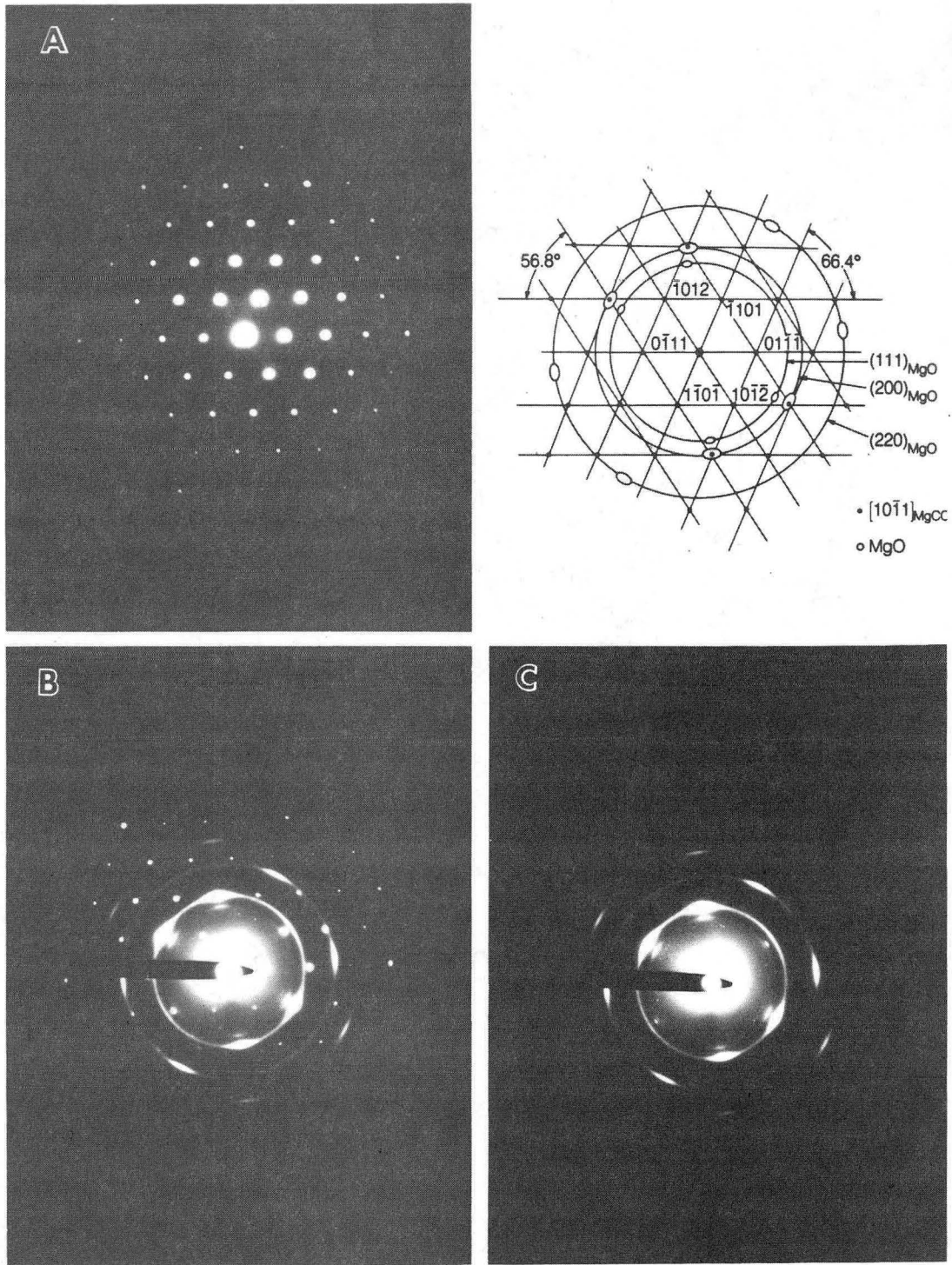


Mg CO₃ (0001) // MgO (111)

Mg CO₃ [1120] // MgO [211]

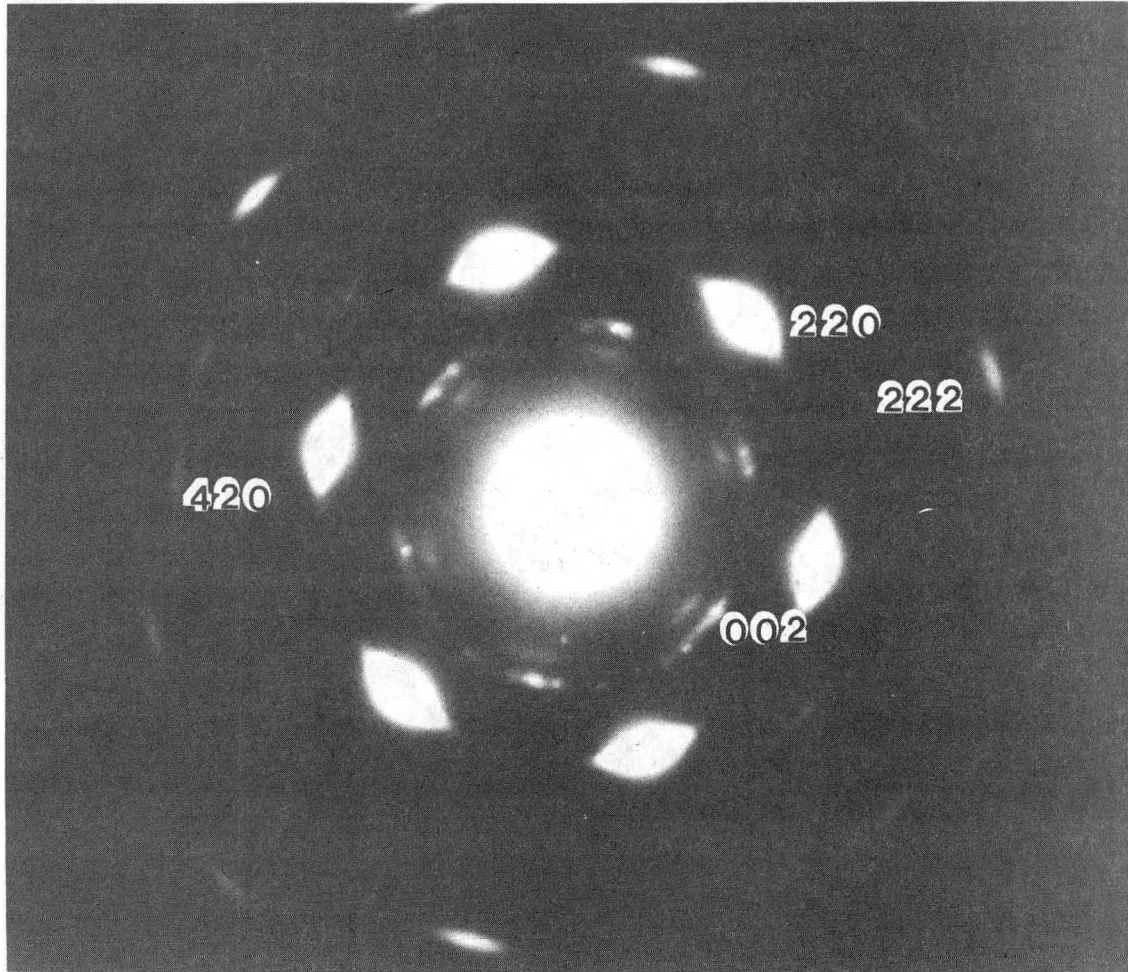
XBL 8410-8781

Fig. 40



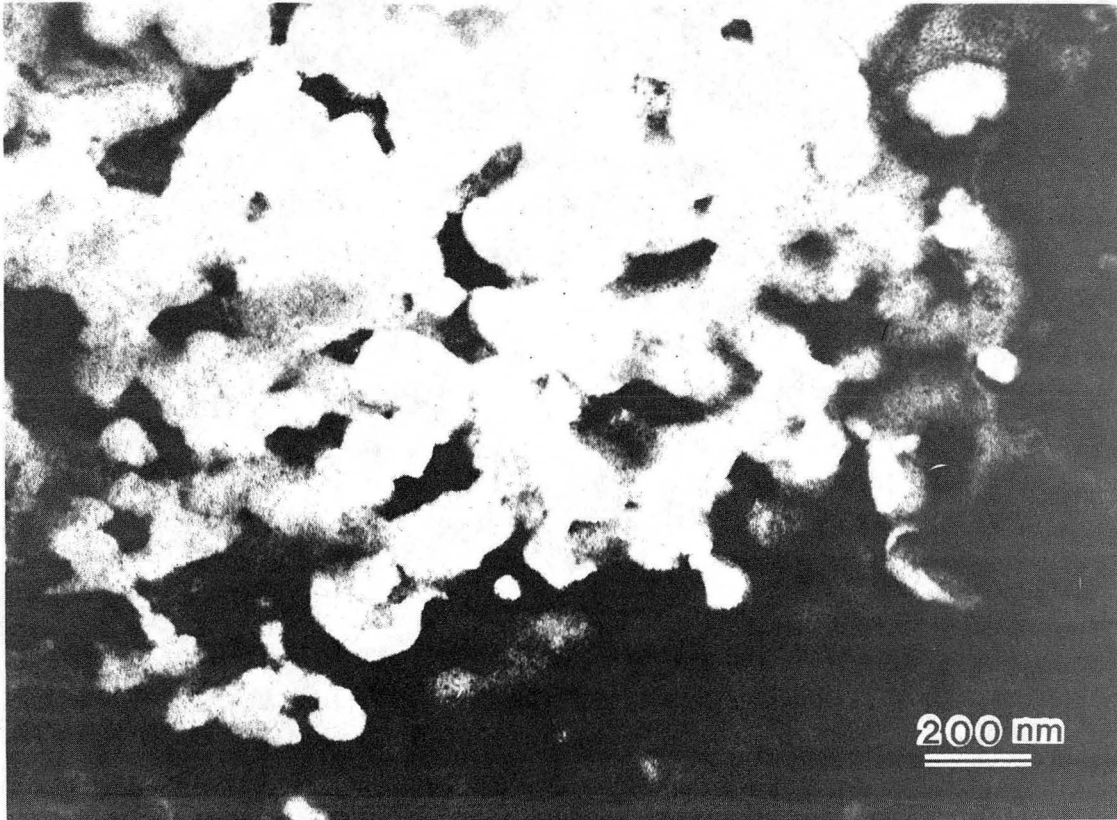
XBB 840-7418

Fig. 41



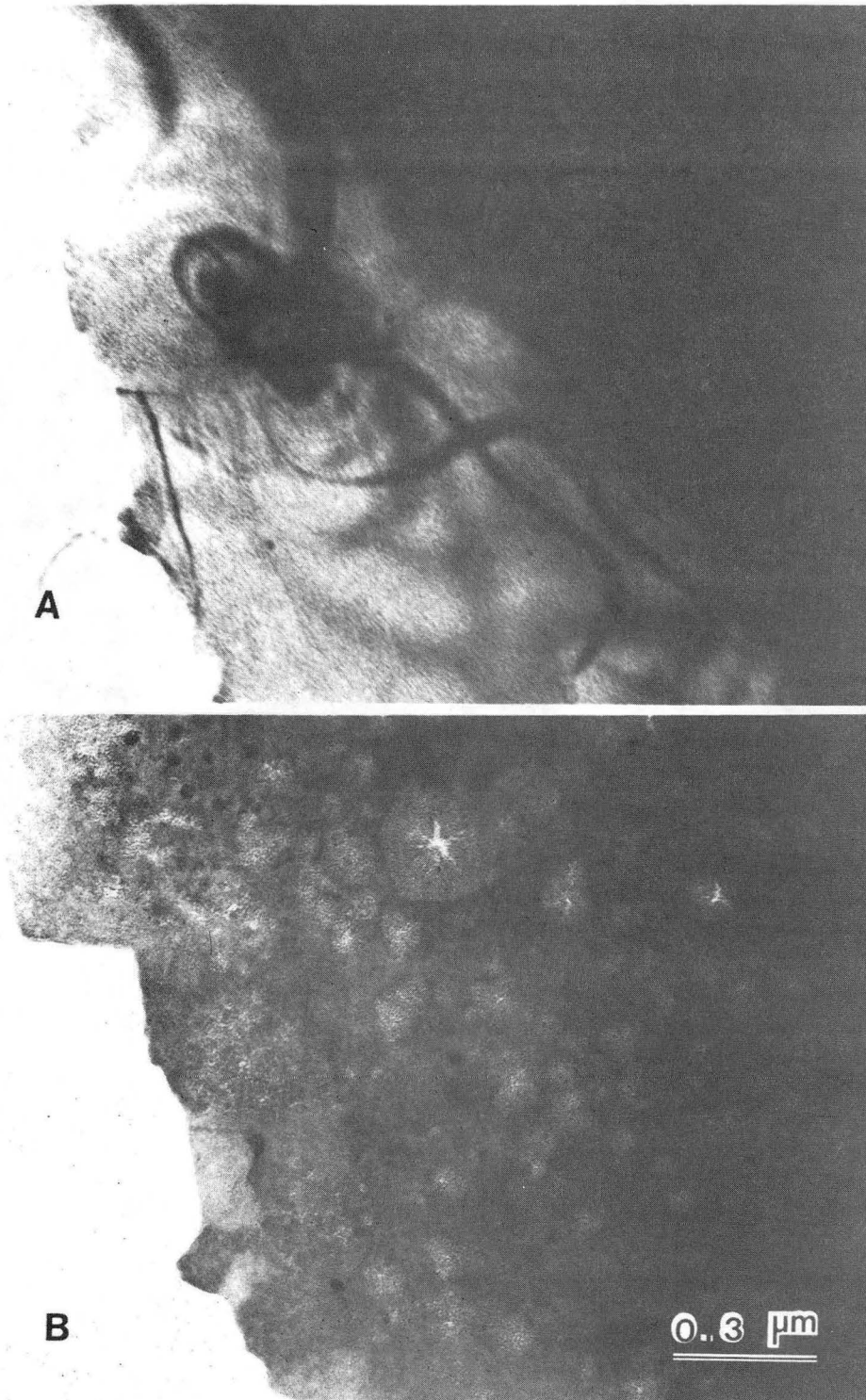
XBB 859-7050

Fig. 42



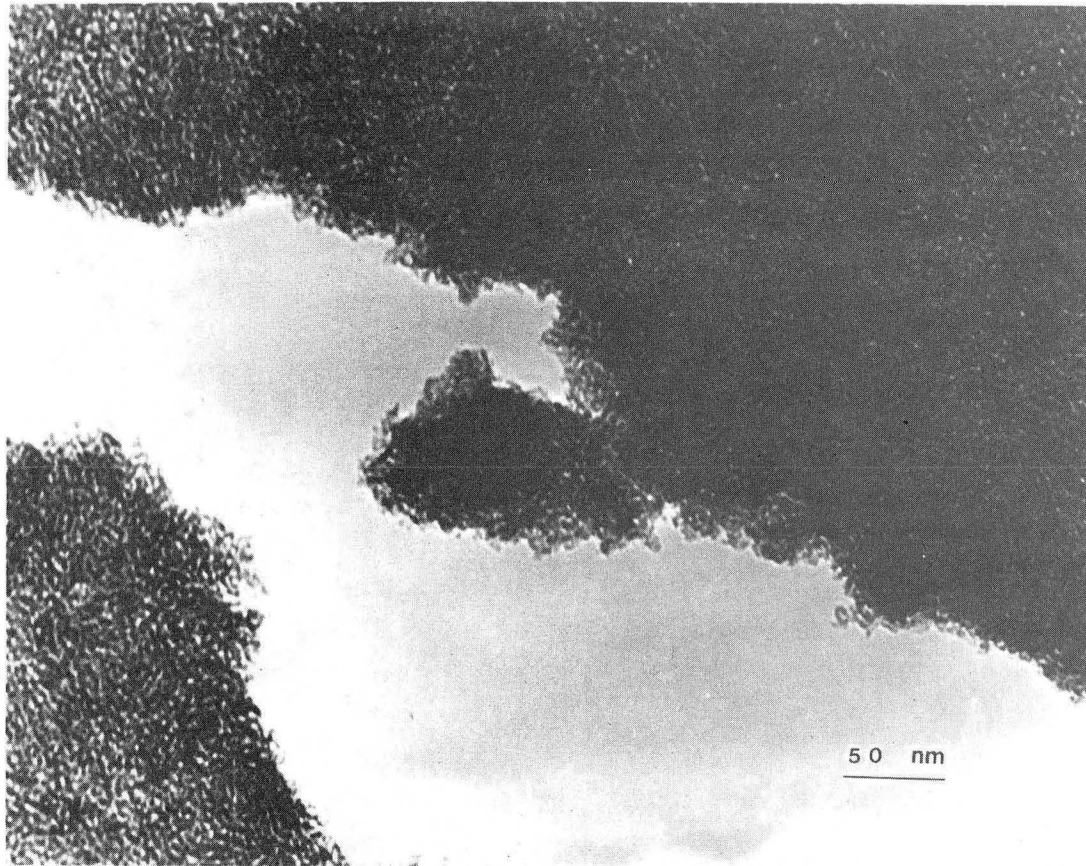
XBB 859-7041

Fig. 43



XBB 854-3154

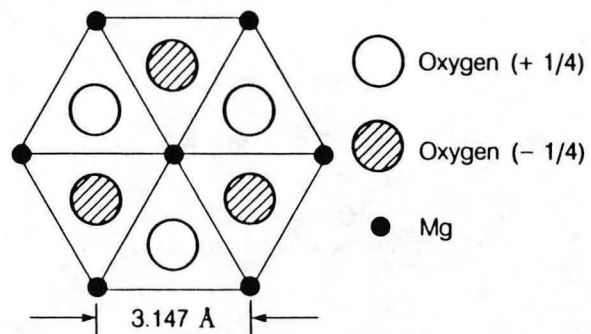
Fig. 44



XBB 840-7412

Fig. 45

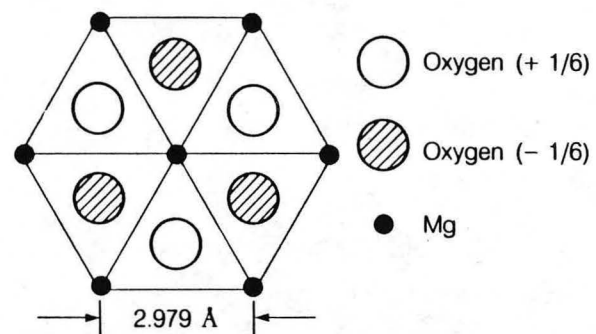
(0001) Projection of $\text{Mg}(\text{OH})_2$



Interatomic Distances and Angles
of Oxygen Octahedra

{	Mg-O	2.102 Å
	O-O'	3.147 Å
	O-O''	2.787 Å
{	O-Mg-O'	96.73 °
	O-Mg-O''	83.05°
	O-Mg-O'''	180.00°

(111) Projection of MgO

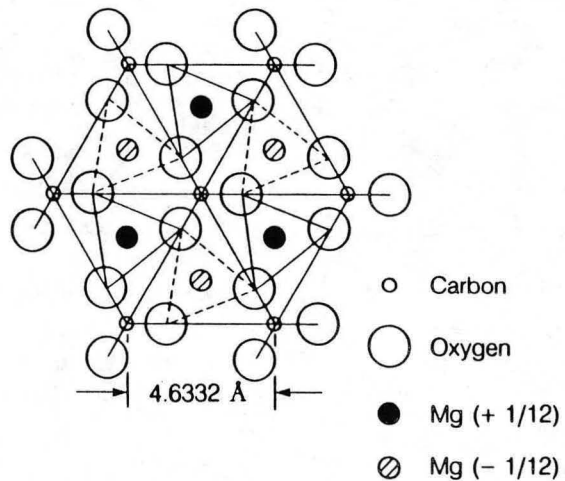


Interatomic Distances and Angles
of Oxygen Octahedra

{	Mg-O	2.1065 Å
	Mg-Mg	2.979 Å
	O-O	2.979 Å
{	O-Mg-O	90°
	O-Mg-O'	180°

Fig. 46

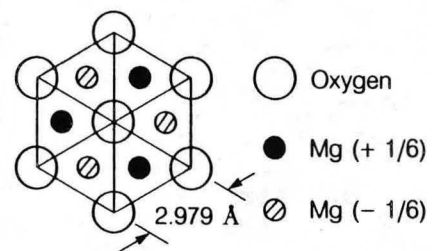
(0001) Projection of MgCO_3



Interatomic Distances and Angles of Oxygen Octahedra

{	Mg-O	2.105 Å
	O-O'	2.850 Å
	O-O''	3.022 Å
{	O-Mg-O'	88.25°
	O-Mg-O''	91.75°
	O-Mg-O'''	180.00°

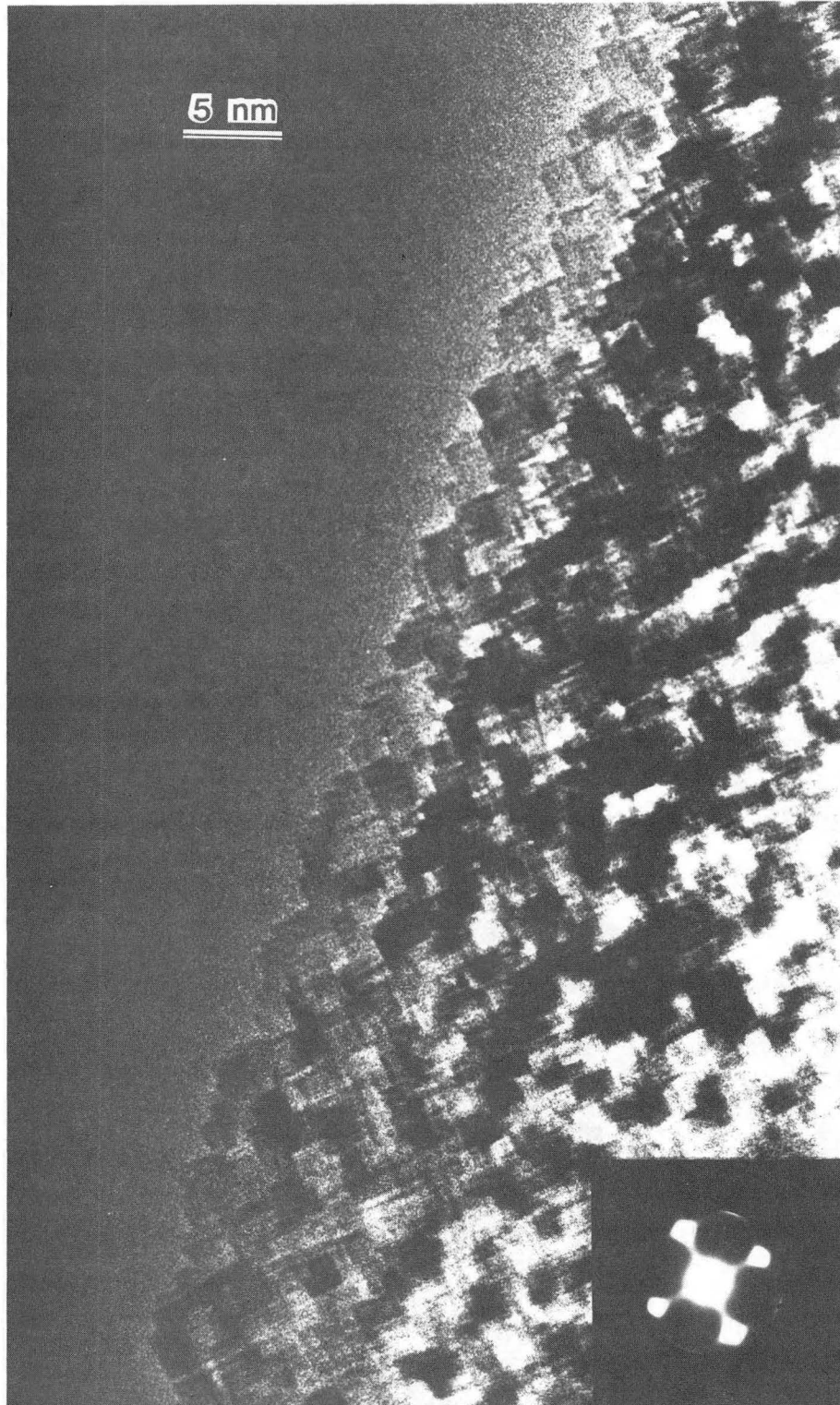
(111) Projection of MgO



Interatomic Distances and Angles of Oxygen Octahedra

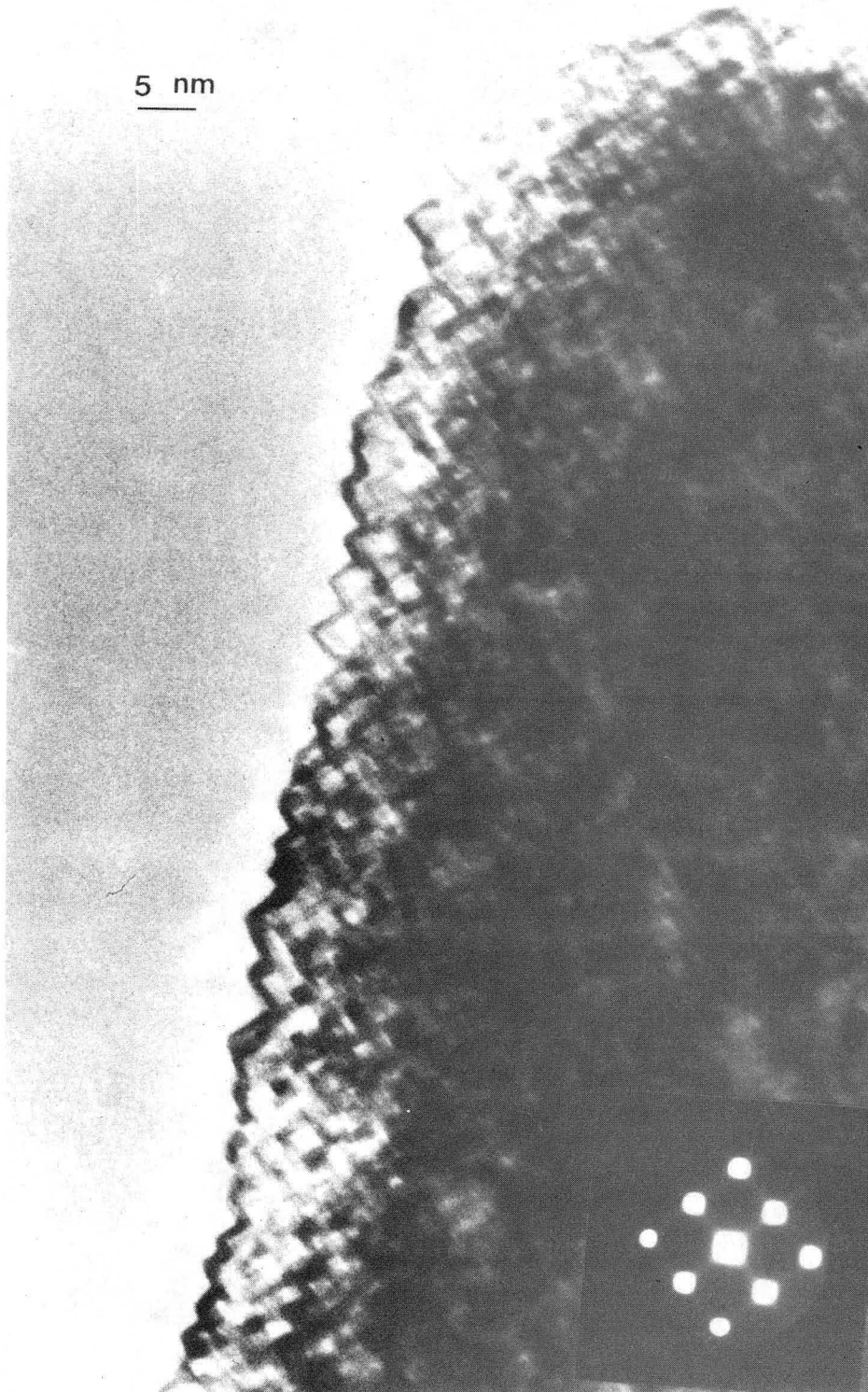
{	Mg-O	2.1065 Å
	Mg-Mg	2.979 Å
	O-O	2.979 Å
{	O-Mg-O	90°
	O-Mg-O'	180°

Fig. 47



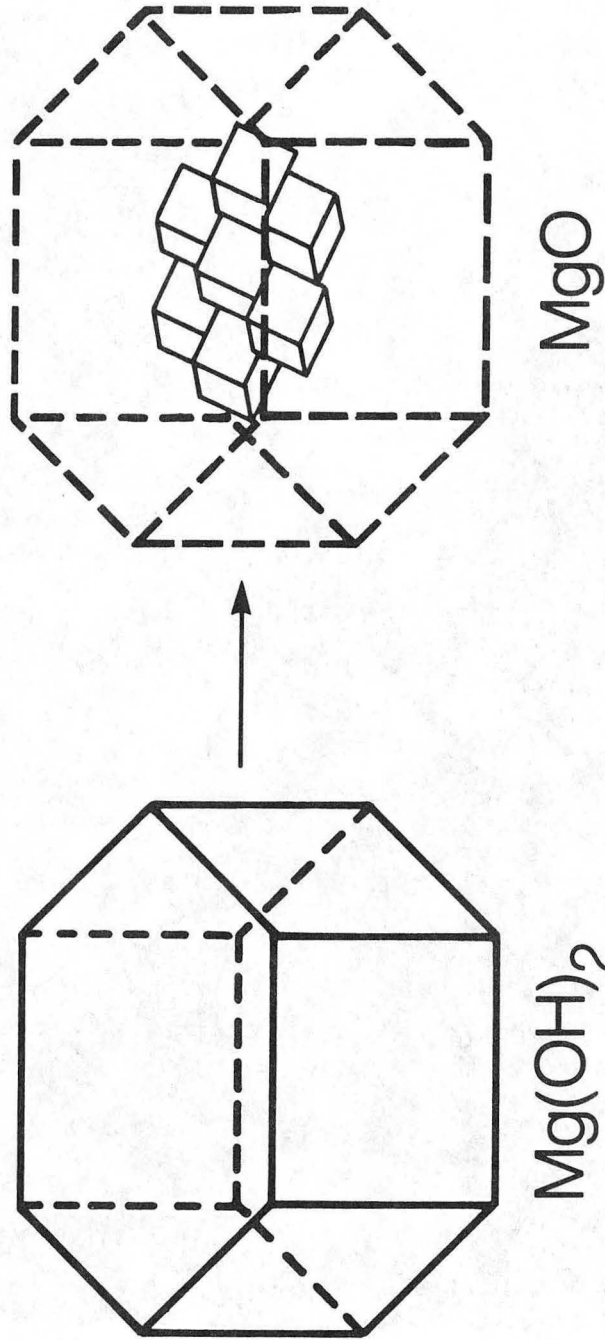
XBB 840-8959

Fig. 48



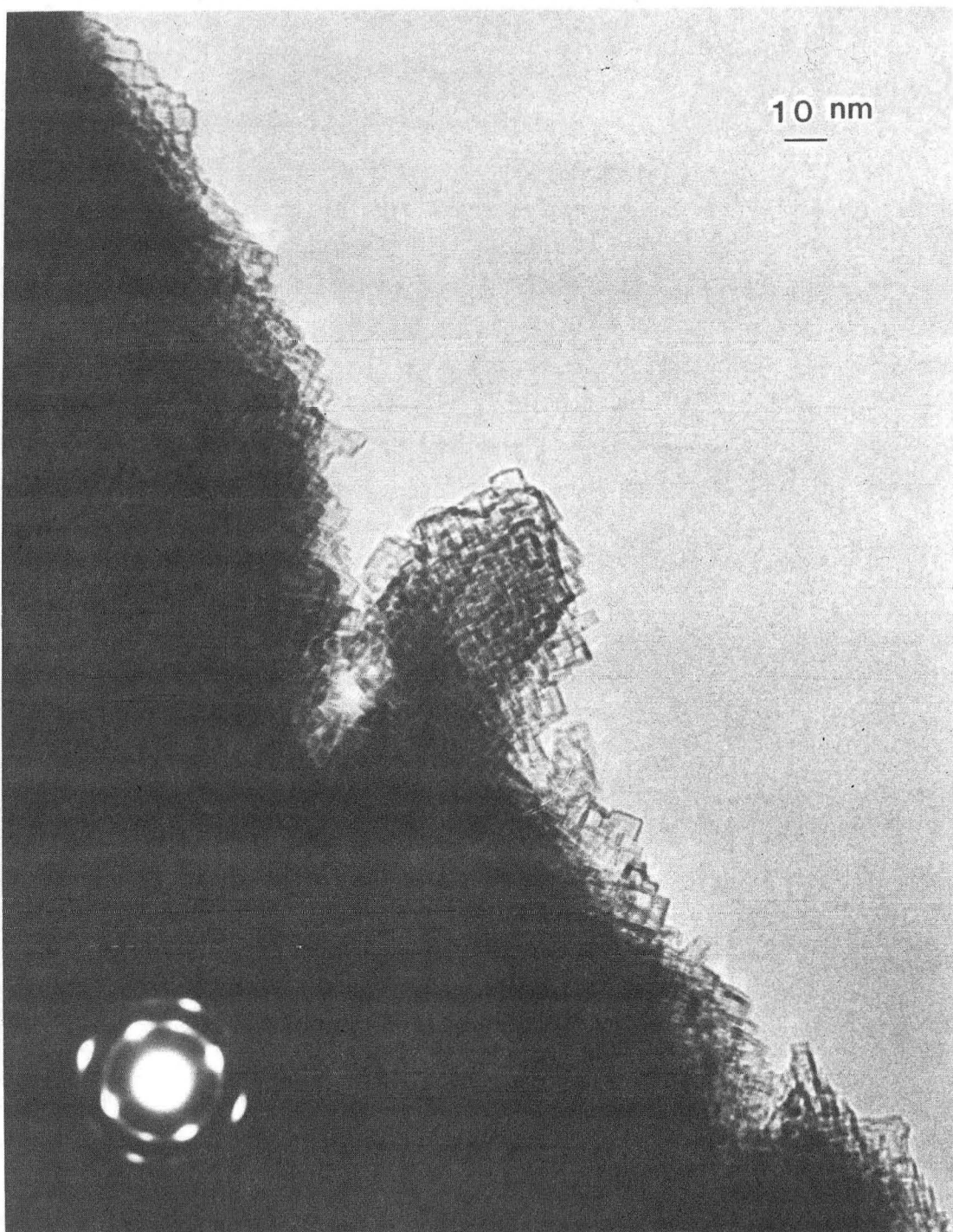
XBB 859-7040

Fig. 49



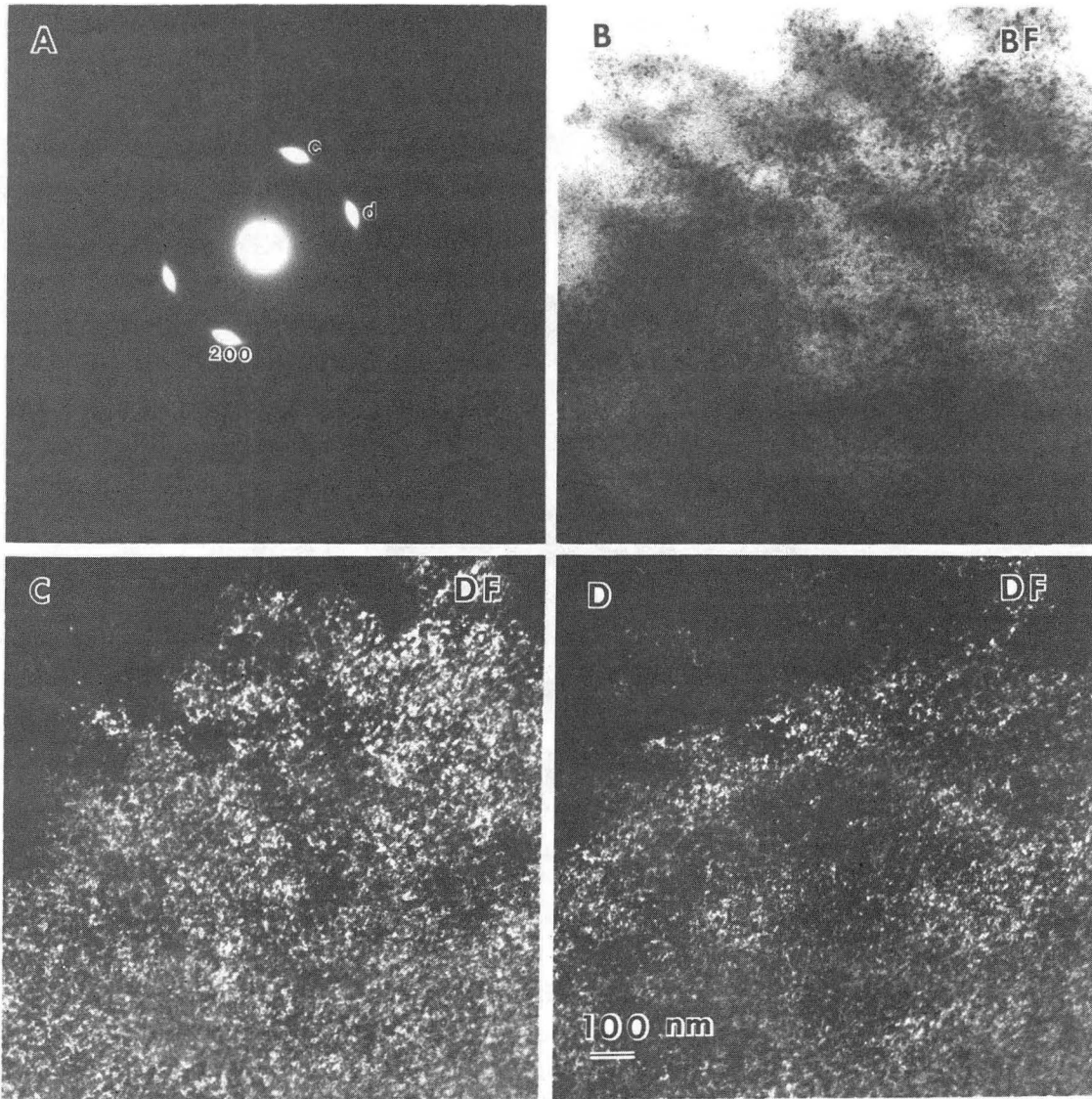
XBL 8410-8780

Fig. 50



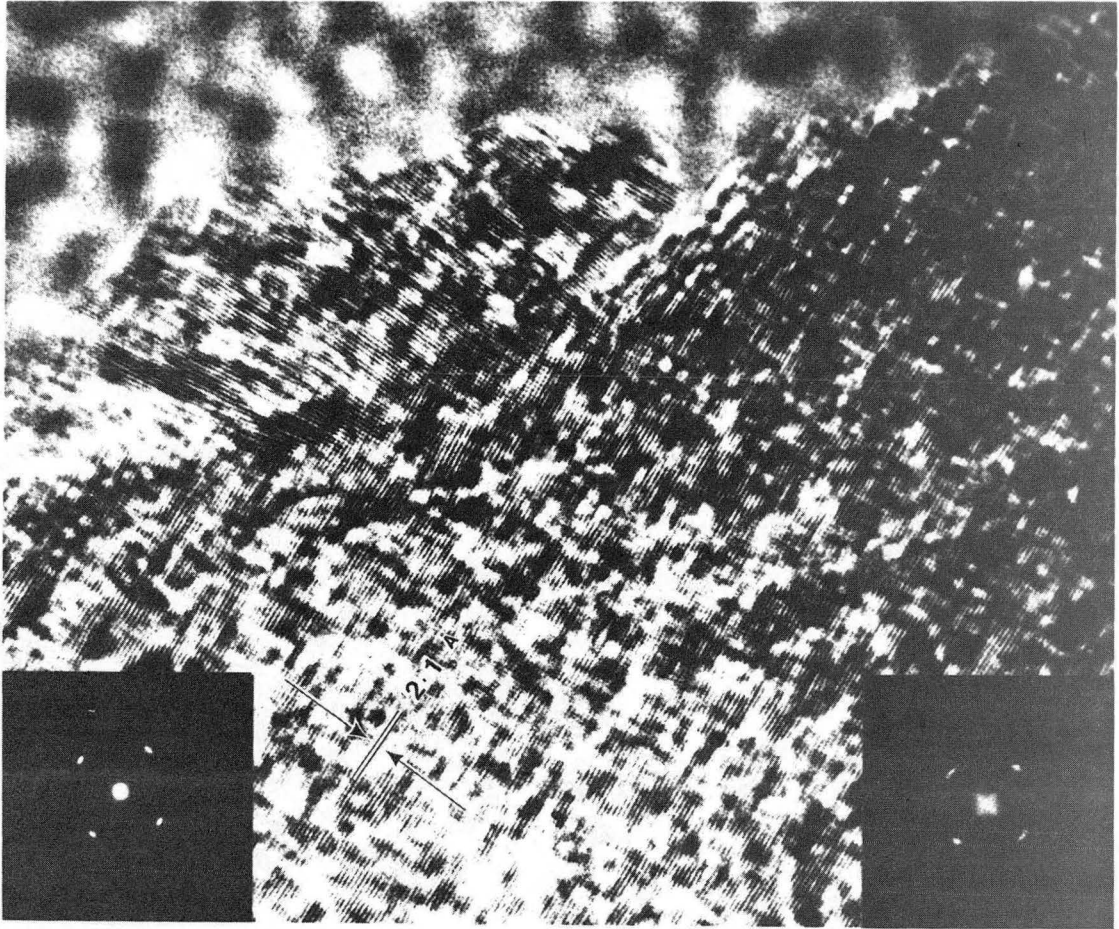
XBB 859-7039

Fig. 51



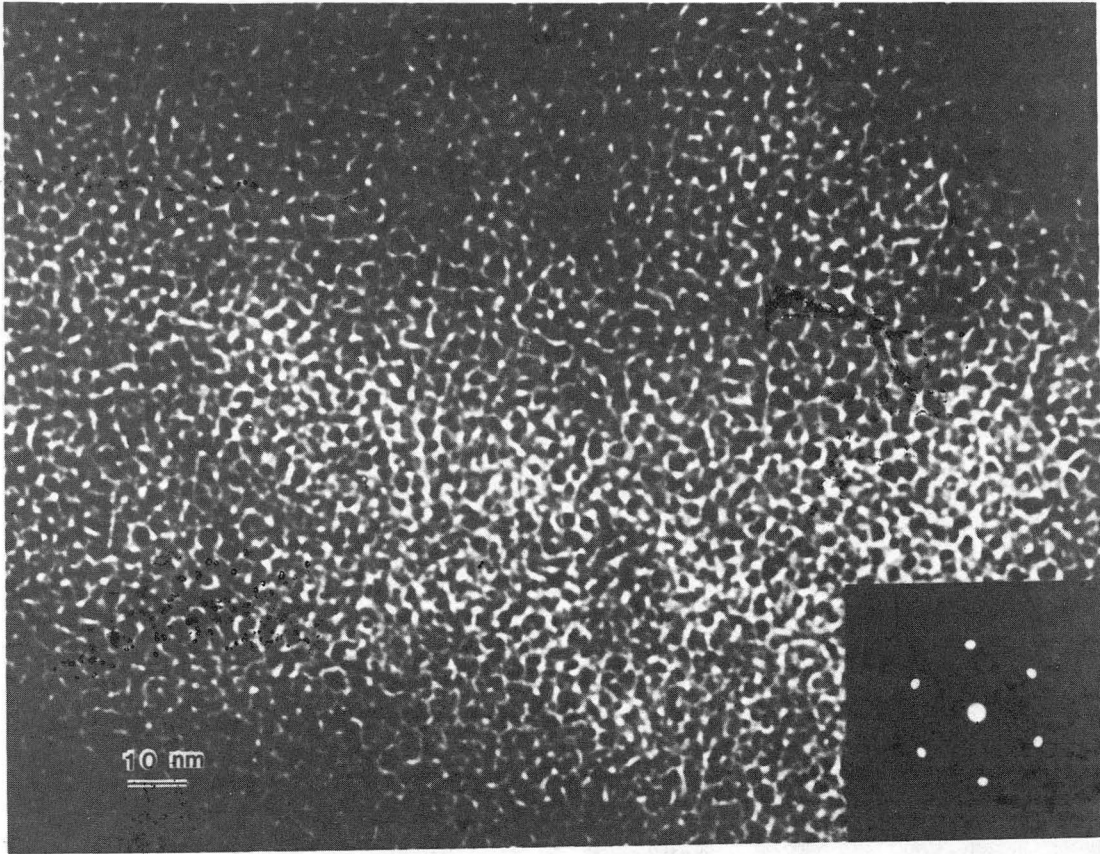
XBB 850-8454

Fig. 52



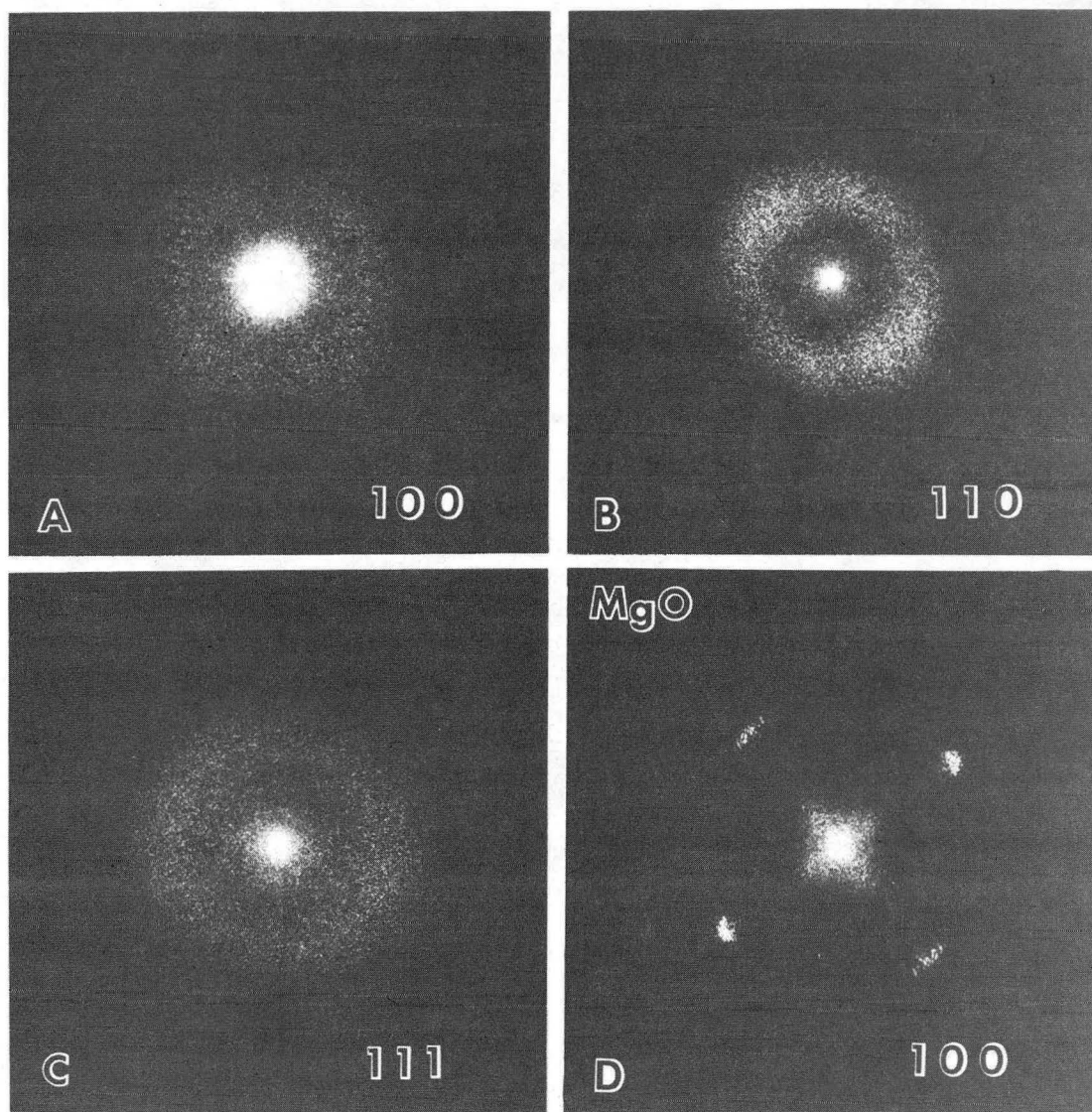
XBB 840-7429

Fig. 53



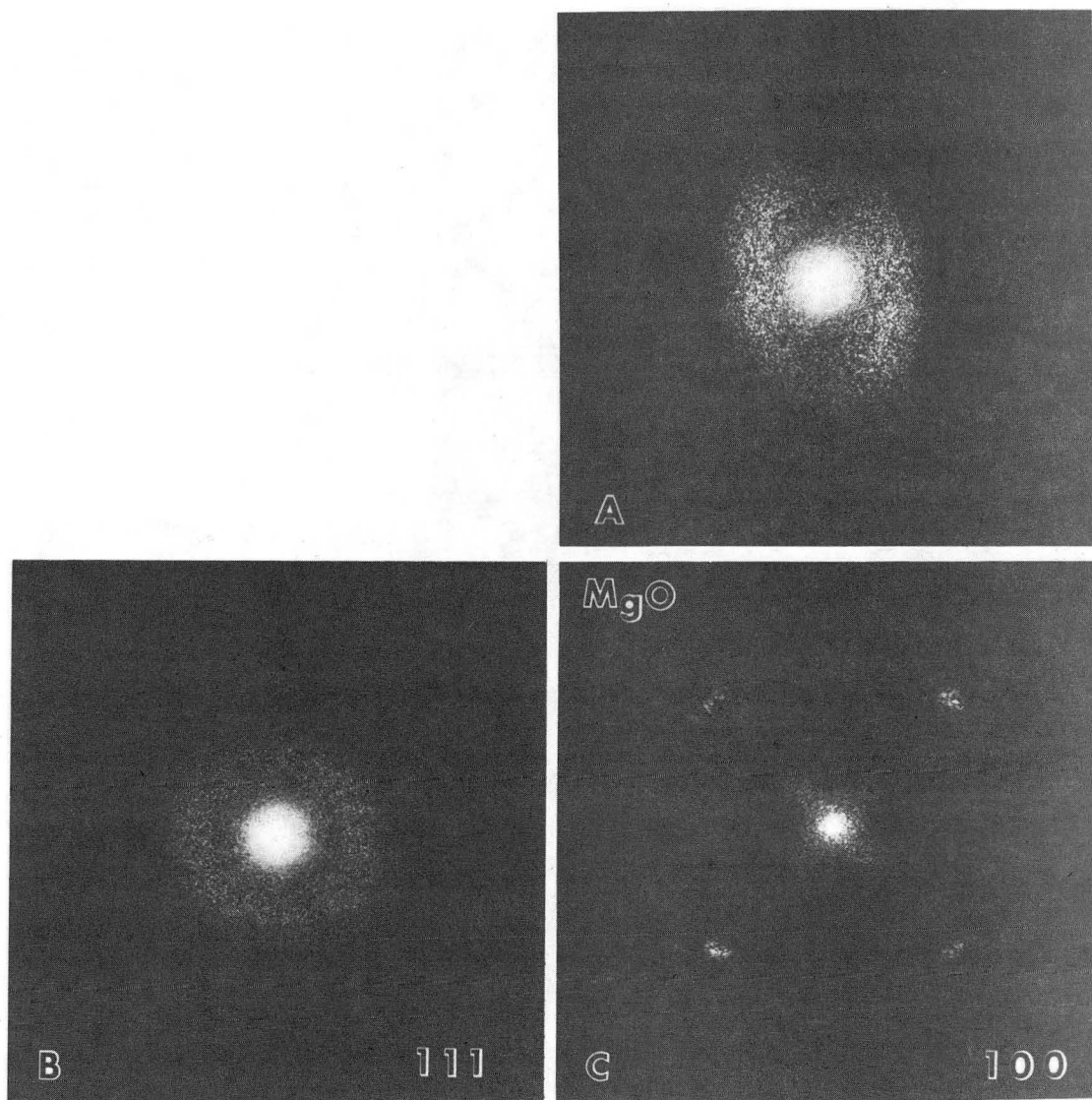
XBB 840-7410

Fig. 54



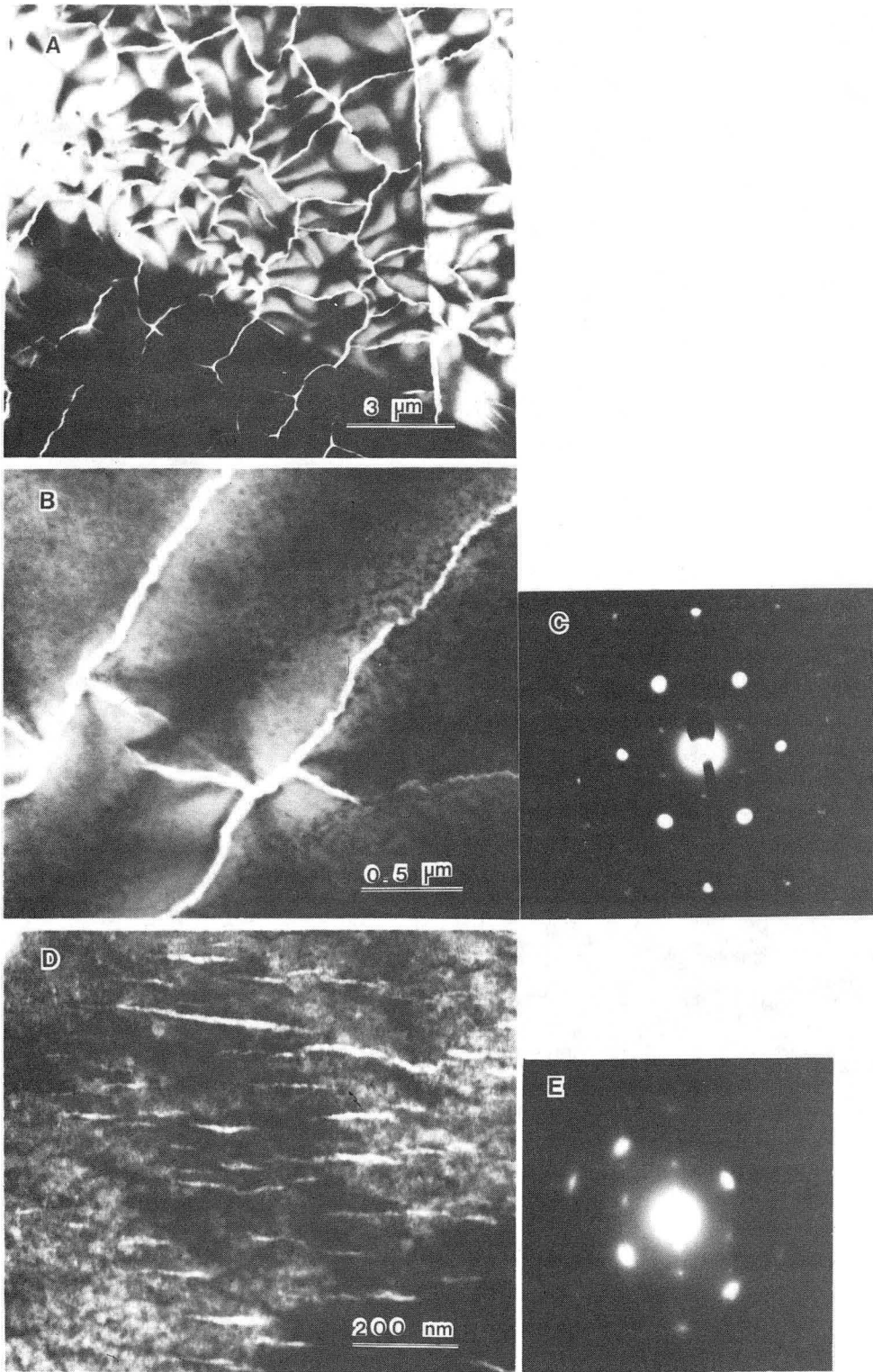
XBB 857-5777A

Fig. 55



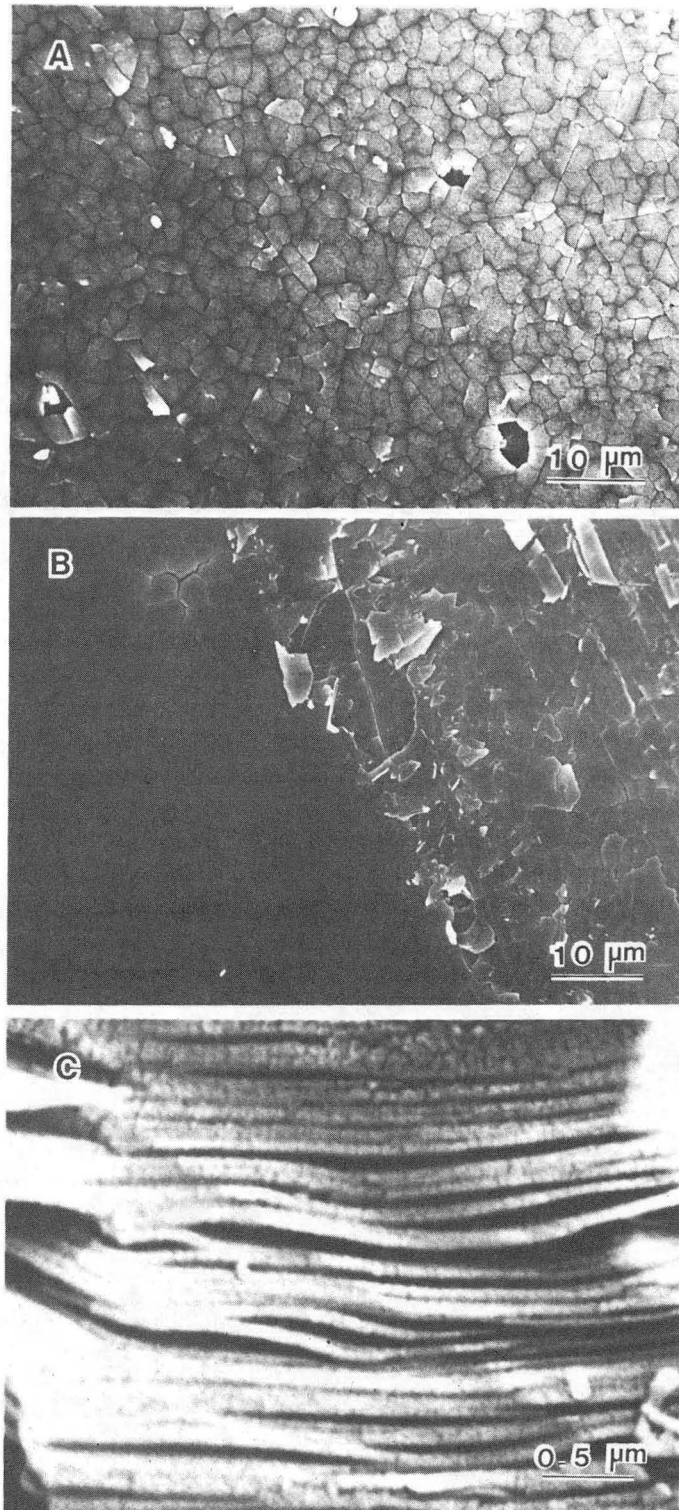
XBB 859-7047

Fig. 56



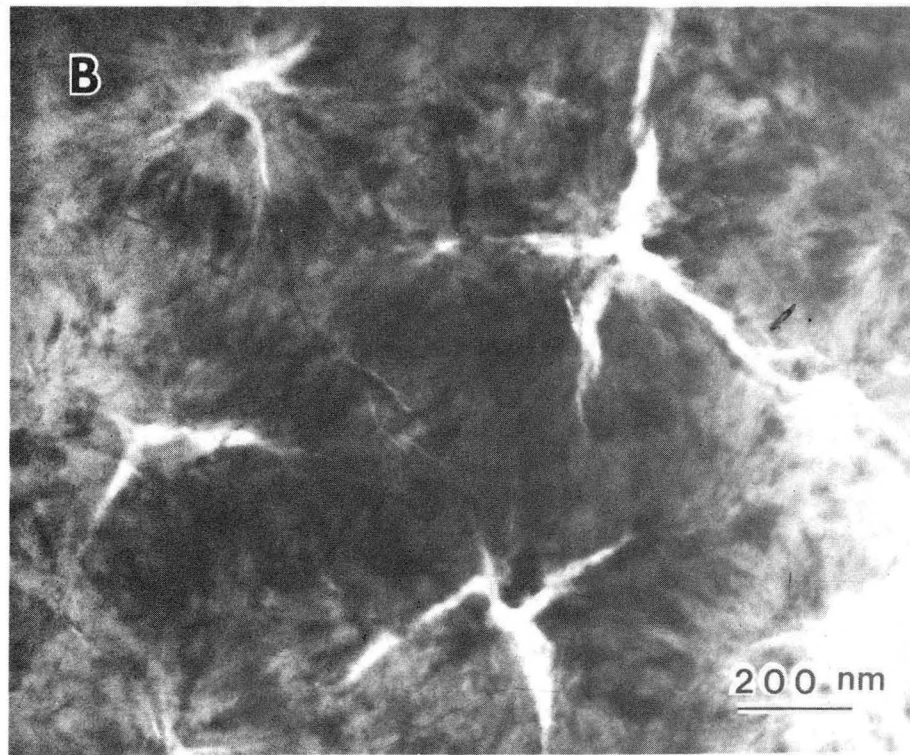
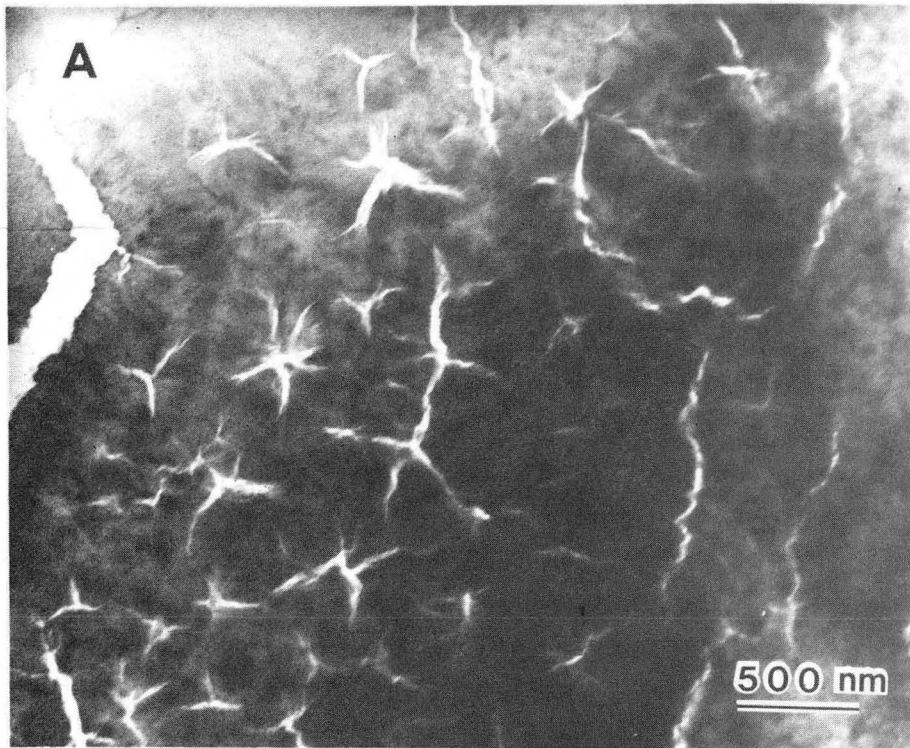
XBB 854-3157

Fig. 57



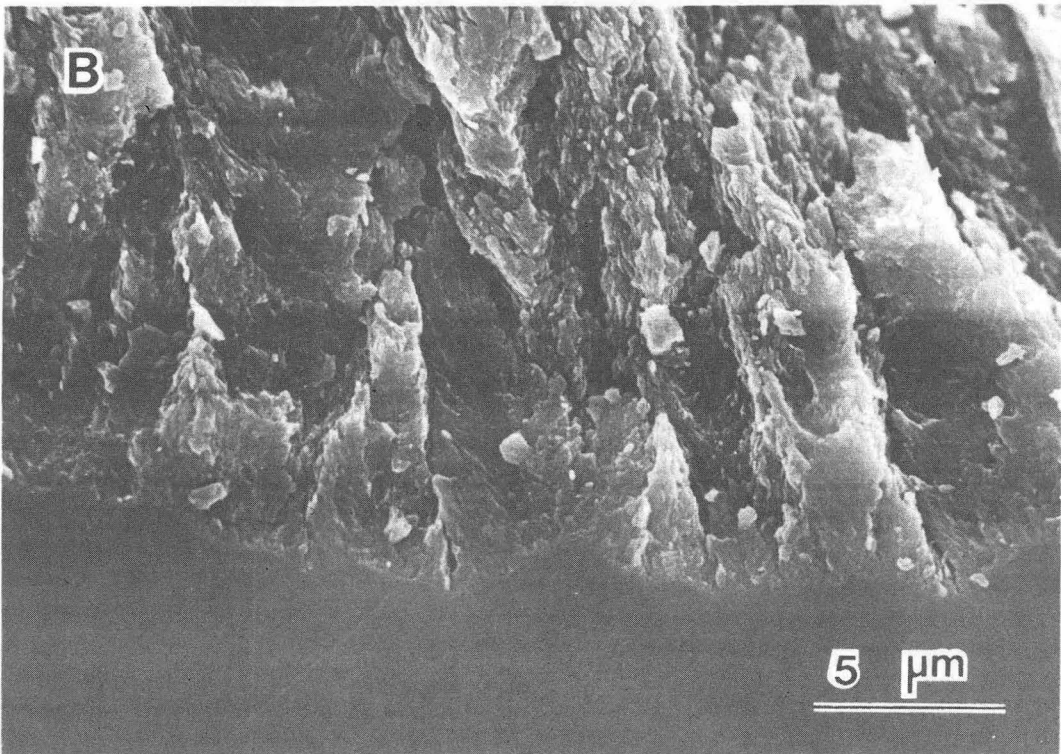
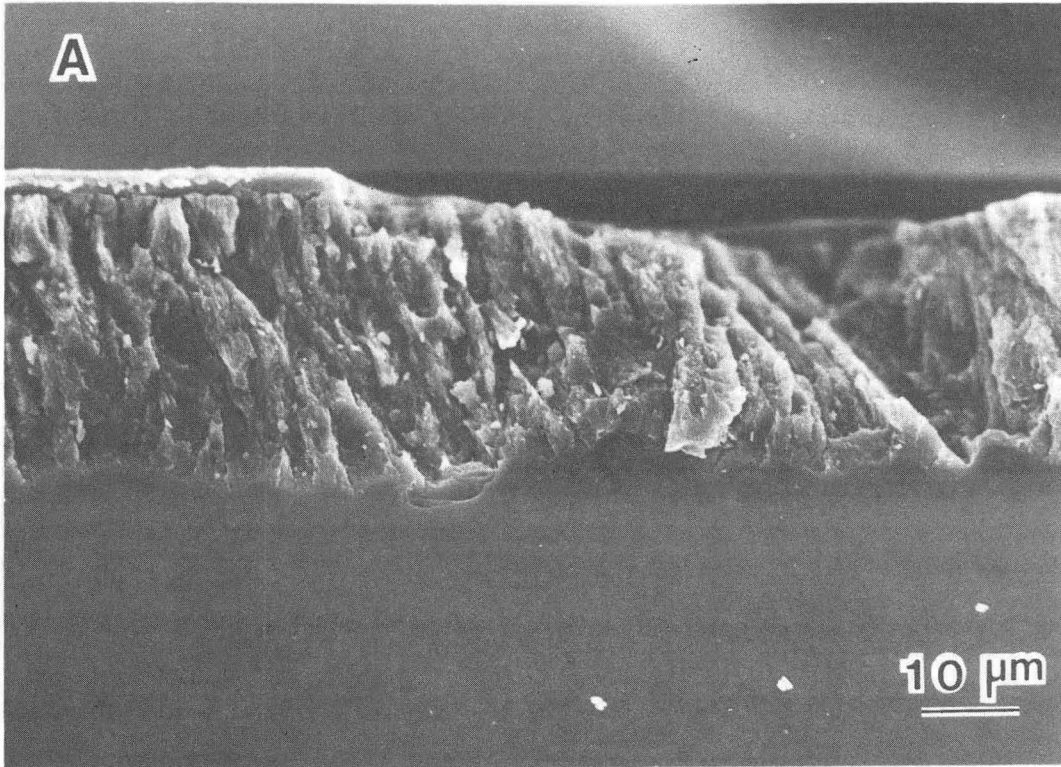
XBB 854-3155

Fig. 58



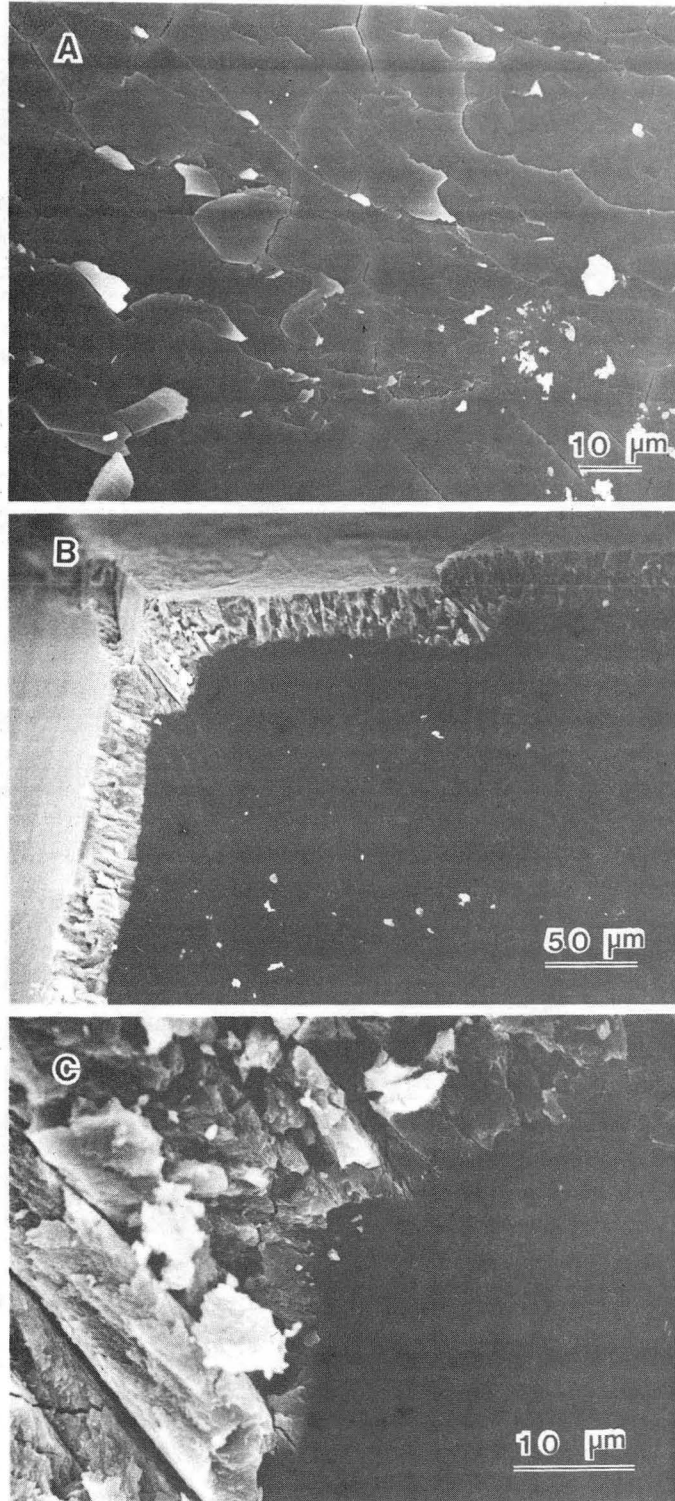
XBB 859-7046

Fig. 59



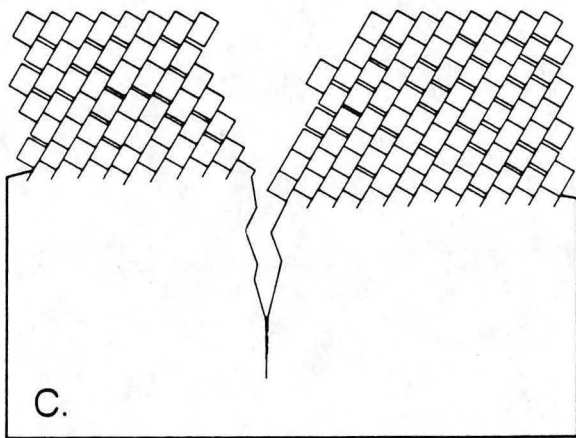
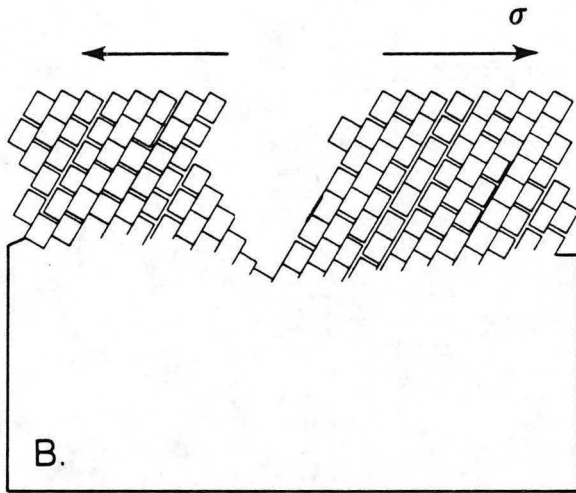
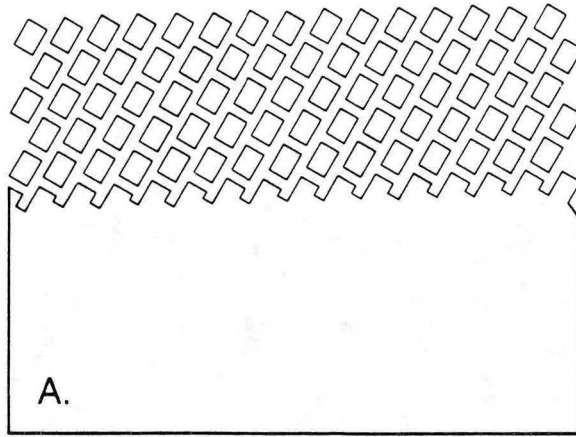
XBB 854-3152

Fig. 60



XBB 854-3156

Fig. 61



XBL 854-2137

Fig. 62

This report was done with support from the Department of Energy. Any conclusions or opinions expressed in this report represent solely those of the author(s) and not necessarily those of The Regents of the University of California, the Lawrence Berkeley Laboratory or the Department of Energy.

Reference to a company or product name does not imply approval or recommendation of the product by the University of California or the U.S. Department of Energy to the exclusion of others that may be suitable.

*LAWRENCE BERKELEY LABORATORY
TECHNICAL INFORMATION DEPARTMENT
UNIVERSITY OF CALIFORNIA
BERKELEY, CALIFORNIA 94720*